The CLAS12 RICH readout electronics: design, development and test

Matteo Turisini

February 2017

Contents

List of Figures

List of Tables

Introduction

Motivation, Goals, State of the Art The new generation of RICH detectors anticipates challenging requirements for the readout systems such as high granularity, high rates, low dead time and low power consumption. In addition, readout systems should often match severe constraints in terms of mechanical fit, material budget, radiation hardness and must have enough flexibility to adapt to different experimental conditions. The current focus is on readout electronics for large arrays of multi-anode single photon sensors.

It is worth to mention that the technological development of the latest year, with unprecedent rate, has been pushed not only by physics or astrophysics but also from other fields. Among these, are the medical field, where imaging techniques derived from physics are used to reach high spatial resolution and sensitivity, and the electronics industry, that created highly integrated application specific circuits and programmable hardware allowing high specialization and high flexibility at the same time.

The main objective of this thesis is to provide a description of the recently developed multi-channel front end electronics for the RICH detector of the CLAS12 experiment at JLab. The cutting edge technology is now at the picocosecond level and many asics are available to readout pulse shapes like in a real time oscilloscope. The RICH electronics is rather based on mature technology and well tested components to match the time constraints for installation and assure a reliable running for few years of operation without the need of access for maintenance. The RICH electronics were developed in a compact and modular way, to be able to serve small installations (i.e. for R&D) as well as large-area detectors, and complemented by a flexible software easy to interface with different environments.

Guide to Chapters Chapter 1 is an introduction to the scientific framework in which the thesis is conducted. It presents the motivations and the general layout of the RICH and its electronics requirements for its readout. Chapter 2 follows with a detailed description of design at hardware, firmware and software level. Once the system has been presented, Chapter 3 and Chapter 4 are dedicated to the performance characterization and single photoelectron response optimization. Chapter 5 is about real condition testing in radiation environments and for Cherenkov light detection and measurements. Finally the Chapter 6, in addition to the conclusion of the entire work, presents few promising extension application where the designed readout electronics can be used.

Personal Contribution of the candidate The author has contributed from the beginning to all the phases of the project. He studied the experimental constraints and provide solutions for the electronics resources, as outlined in chapter 1. He contributed with stimulating ideas to the design of the electronics and suggested improvements for reducing the interference between analog and digital lines and increase the number of resources on board, as described in chapter 2. He develop the software library for run control, data storage, parsing and analysis. The software suite is suitable for simple testing stand-alone setups as well as for the real large-scale experiment and was used in all the phases of the electronics development: pulser and laser test benches, irradiation and beam tests. He realized the automatic protocol for the tile validation, characterization, calibration and use, as detailed in chapter 3. He tested the performance with photo sensors, as discussed in chapter 4. He was in charge of the readout system in all the experimental campaigns performed during the project, as described in chapter 5.

Chapter 1

The CLAS12 RICH Project

One of the world leading laboratories for the study of nature at nuclear and sub-nuclear scales is Jefferson Lab (JLab) where the Continuous Electron Beam Accelerator Facility (CEBAF) has been recently upgraded to reach 12 GeV energy and access smaller scale of investigations. A new experimental hall was built and the three pre-existing halls renewed their spectrometers to refine the performance on the extended energy range. The CEBAF Large Acceptance Spectrometer (CLAS12) in Hall-B, that is receiving beam for the first time during the writing of this thesis, is going to use in few months an innovative RICH detector to improve its particle identification capability. This chapter introduces the RICH detector, its role in CLAS12, and the motivation that inspired the construction of the counter. After a general description of the detector layout and components, the specific requirements for the RICH readout electronics are discussed. The definition of the services (power supply, DAQ, gas system, cooling and interlock) and their routing in the experimental hall are also outlined being part of the present work.

1.1 Scientific objectives

Lepton Deep-Inelastic Scattering (DIS) is the basic tool for determining the fundamental structure of matter, in particular of the nucleon, the founding block of our observable physical world. Experiments using high energy lepton beams have successfully tested the theory of Quantum Chromodynamics (QCD), which describes the strongly interacting matter in terms of the basic quark and gluon degrees of freedom. The successful prediction of the scale dependence of the parton distributions, which were introduced to describe the complex structure of the nucleon, has been one of the great triumphs of pertubative QCD.

Nevertheless surprising phenomena have been observed that are awaiting an explanation since decades, i.e. the small fraction of the nucleon spin generated by the parton spin and the single-spin asymmetries in hadron interactions. Lately they have been related to the complex parton dynamics into a confined object (nucleon) and an increasing interest has been focused on the partonic transverse degrees of freedom. These studies can be completed only in conjunction with the flavor information that can be accessed by exploiting particle identification in the final state. RICH detectors are powerful and sophisticated instruments to provide excellent hadron identification and may have an impact in several flagship investigations planned at CLAS12.

1.1.1 Nucleon structure: towards a 3D image

One of the most surprising results of thirty years of explorations in Hadronic Physics, is the evidence that only an unexpectedly small fraction, about a quarter, of the proton's spin can be ascribed to the contribution of quark and antiquark spins. This finding has triggered a vast experimental and theoretical activity aiming at clarifying the role gluon and parton orbital angular momenta play for a complete description of the proton spin structure. New concepts as Transverse Momentum Dependent (TMD) parton distribution and fragmentation functions, which go beyond the historical collinear approximation, are a key to unravel the intricacies of the parton dynamics inside a confined object like the nucleon. They can shed light on the possible connections between the parton orbital motion and the spin of the nucleon, which cannot be described with standard (e.g. collinear) parton distributions. TMD distributions together with the so-called Generalized Parton Distributions (GPDs) provide for the first time a framework to obtain information towards a genuine multi-dimensional momentum and space resolution of the nucleon structure [1]. This knowledge will likely have an important impact to other fields of nuclear and high-energy physics [2].

The mapping of GPDs and TMD distributions and the deduction of a three-dimensional image of the nucleon is a major focus of the hadron physics community and constitutes a milestone in the physics program of the JLab 12 GeV upgrade [3].

While GPDs can be probed in hard exclusive processes where the nucleon stays intact and the final state is fully observed, TMD distributions are most successfully measured in Semi-Inclusive Deep-Inelastic Scattering (SIDIS). In SIDIS experiments, at least one hadron is detected in the final state in addition to the scattered lepton. These experiments are the most powerful tool for obtaining direct flavour-dependent information about the nucleon's quark structure. In particular, they provide unique access to the elusive strange quark distributions. Pioneering polarized semi-inclusive DIS experiments have revealed surprising effects in various different kaon production observables, which deviate from the expectations based on a u-quark dominance for the scattering off a proton target. The peculiar kaon results point to a significant role of sea quarks, and in particular the strange quarks. For almost all kaon observables, the deviation from the expected behavior is most pronounced in the kinematic region around $x_B = 0.1$ (x_B being the Bjorken scaling variable), which is well covered by CLAS12. In order to fully explore the power of SIDIS experiments, pion, kaon and proton separation over the full accessible kinematic range is indispensable.

Measurements with kaons in semi-inclusive and hard-exclusive processes will be crucial in understanding the underlying dynamics behind spin-orbit correlations in hard processes and accomplishing the CLAS12 program of studies of the three-dimensional structure of the nucleon.

1.1.2 Effects of nuclear matter

Besides the exciting new aspects of nucleon structure investigation, a very interesting pattern of modifications of parton distribution and fragmentation functions in nuclear matter has been observed in lepton-nucleus scattering, which generated an intense experimental and theoretical activity. The understanding of quark propagation in the nuclear medium is essential for the interpretation of high energy proton-nucleus interactions and ultra-relativistic heavy ion collisions. Lepto-production of hadrons has the virtue that the energy and momentum transferred to the struck parton are well determined, as it is “tagged” by the scattered lepton. The nucleus can be basically used as a probe at the fermi scale with increasing size or density, thus acting as a femtometer-scale detector of the hadronization process. Theoretical models can therefore be calibrated in nuclear SIDIS and then applied, for example, to studies of the Quark-Gluon-Plasma in ultra-relativistic heavy-ion collisions.

The experimental results achieved over the last decade demonstrate the enormous potential of nuclear SIDIS in shading light on the hadronization mechanisms. For all observables investigated so far, a very distinct pattern of nuclear effects was observed over various different hadron types. However, the existence and relative importance of the various stages, like the propagation and the interaction of the original parton, the color-neutralization and the final hadron formation, are far from being determined unambiguously.

In this panorama, JLab with its high beam intensity and the usage of a large variety of nuclear targets will provide data in a kinematic region that is very suitable for studying nuclear effects. The ability of performing a fully differential analysis is a key to disentangle the various different stages of hadronization. The capability of identifying pions, kaons and protons over the whole kinematic range of interest will be crucial for gaining insights into the space-time evolution of the hadronization process.

1.1.3 Search for exotic mesons

The phenomenology of hadrons and in particular the study of their spectrum led more than forty years ago to the development of the quark model, where baryons and mesons are described as bound systems of three quarks and of a quark-antiquark pair, respectively. In addition to these states, which have been experimentally observed and extensively studied, phenomenological models and lattice QCD calculations suggest the existence of exotic configurations such as hybrids (qqg), tetraquarks ($qq\bar{q}\bar{q}$) and glueballs. The experimental verification of the existence of such exotic states would significantly deepen our knowledge about the dynamics of QCD.

A very attractive method to identify exotic mesons is through strangeness-rich final states, where kaons from the decay of the involved ϕ-meson are usually high energetic. Kaon identification over the whole accessible momentum range would hence provide unique capabilities for the study of strangeonia and the search for exotic mesons.

1.2 CLAS12 particles identification

The exciting physics program of Hall-B at JLab, aiming at a detailed investigation of the three-dimensional structure of nucleons, is based on the unique features of the upgraded CEBAF and CLAS12 spectrometer:

- high beam energy and intensity,
- high beam polarization,
- longitudinally and transversely polarized proton and deuterium targets,
- variety of nuclear targets,
- large acceptance, multipurpose spectrometer,
- excellent particle identification.

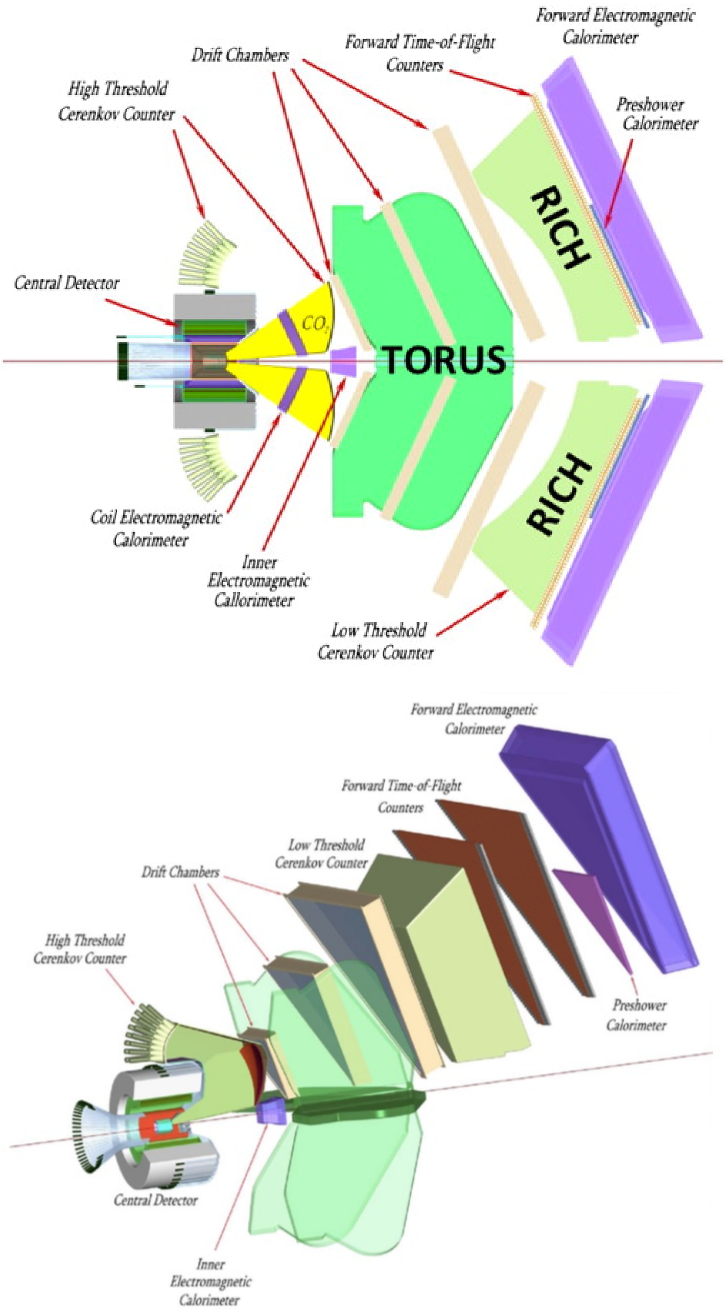

Figure 1.1: Detection elements that constitute the CLAS12 spectrometer. The target is located inside the Central Detector. In the exploded view, only one out of six sectors of the Forward Detector is shown.

1.2.1 The CEBAF Large Acceptance Spectrometer

CLAS12 is designed to operate at a luminosity of $10^{35}\,\mathrm{cm}^{-2}\mathrm{s}^{-1}$ and offers an almost complete coverage of the final state phase space. The detector, shown in figure 1.1, consists of two parts, a Forward Detector (FD) and a Central Detector (CD). The CD, with its high-field (5 T) solenoidal magnet, surrounds the target and is used to detect recoiling particles at large angles. It comprises a barrel tracker, a time of flight system for charged particle identification (TOF) and a neutron detector. The FD detects charged and neutral particles in the polar angle range between 5° and 40°. It is based on a 2 T superconducting toroidal magnet and it is organized in 6 sectors (wedges) to cover the full azimuthal angle extent. It includes a tracking system made of a vertex tracker and three regions of drift chambers (DC), the second of which inside the toroidal field. Baseline particle identification is accomplished by two gas Cherenkov detectors for electron/pion separation (High-Threshold Cherenkov Counter, HTCC, and Low-Threshold Cherenkov Counter, LTCC), a forward Time-Of-Flight (FTOF) system for hadron identification and a preshower and electromagnetic calorimeter to help in electron identification and to detect neutral particles.

1.2.2 Baseline PID

Hadron identification in the FD is obtained by combining the information of HTCC, LTCC and FTOF. As will be shown in the next paragraphs, by using only these detectors no sufficient separation of kaons from pions can be achieved in the momentum range relevant for SIDIS reactions. However, they may give essential contributions in specific kinematic regions and should be accounted for in the general CLAS12 hadron identification strategy.

Forward Time of Flight (FTOF)

The FTOF system is composed by two panels of plastic scintillators, one with 15 cm wide bars and the other with 6 cm wide bars. Combining the two panels, the time resolution ranges between 45 and 80 ps, depending on the polar angle of the particle, i.e. the bar length. As the distance between the target and the FTOF system is about 650 cm, a good separation of pions and kaons is achievable only in the low momentum region below 3 GeV/c.

High Threshold Cherenkov Counter (HTCC)

The HTCC counter is a circular shaped detector designed to separate electrons from pions with high efficiency. It is composed by a CO_2 radiator and large photomultipliers with quartz window. About 16.5 photoelectrons (p.e.) are expected in average for an electron track, with small dependence on the polar angle. Kaons and protons are always below threshold and cannot be detected. For pions, the number of p.e. goes from 0 at the threshold of about 5 GeV/c up to 12 at the maximum 10 GeV/c momentum. Inefficiency in their estimation can be calculated using Poisson fluctuations on the number of detected p.e. For example, with a minimum number of 3 p.e., a 3σ confidence level may be obtained only above $P = 7.8\,\mathrm{GeV/c}$ and a 4σ separation may be obtained only in the extreme region of the momentum distribution.

Low Threshold Cherenkov Counter (LTCC)

The LTCC counter is made by a C_4F_{10} gas radiator with a pion threshold at 2.7 GeV/c momentum and a number of p.e. about a factor of two smaller than the HTCC. Protons are below threshold for momenta up to about 9 GeV/c. As done for HTCC, the LTCC pion inefficiency can be estimated using Poisson statistics. A 3σ separation may be achieved above 7.7 GeV/c only with a minimum cut at two photoelectrons. Such a low cut however may lead to incorrect identification due to possible background hits. The required 4σ cannot be obtained over the whole momentum range.

In conclusion, the CLAS12 baseline instrumentation can not provide adequate kaon identification in the momentum range between 3 and 8 GeV/c. By replacing at least one sector of the existing LTCC with a RICH detector, hadron identification can be extended to the full momentum range reaching the wide coverage required by SIDIS analyses.

1.2.3 Impact of RICH

The addition of a RICH detector would significantly enhance the particle identification capabilities of CLAS12 [4] and make Hall-B an ideal place for obtaining flavour separated information about the complex multi-dimensional nucleon structure. The novel TMDs and GPDs will be uniquely explored in the valence kinematic region where many new, intriguing aspects of nucleon structure are expected to be most relevant. Furthermore, as pions greatly outnumber the other hadrons at nearly all kinematics, the RICH detector can tremendously reduce the backgrounds for the detection of unstable particles with at least one charged decay product different from a pion, hence opening a new window for studying exotic mesons with strangeness contents.

The main objectives of the physics program for CLAS12 with a RICH detector are:

- *The role of strangeness*: Exploration of the elusive strange quark distributions in the nucleon and search of signatures for intrinsic strangeness using kaon production in unpolarized and doubly longitudinally polarized deep-inelastic scattering off proton and deuterium targets, as well as exclusive kaon-hyperon and ϕ-meson production.

- *Intricacies of parton intrinsic transverse momentum*: Study of the flavour and kinematic dependence of the intrinsic transverse quark momenta employing fully differential analyses of pion and kaon production in unpolarized deep-inelastic scattering off proton and deuterium targets.

- *Nucleon imaging in transverse momentum space and the role of spin-orbit correlations*: Mapping of the full set of leading and subleading TMD quark distributions via the extraction of spin and azimuthal asymmetries for pions and kaons from deep-inelastic scattering off unpolarized, transversely and longitudinally polarized proton and deuterium targets.

- *Gluon imaging in coordinate space*: Study of the transverse spatial distribution of 'valence-like' gluons from hard exclusive ϕ-meson production.

- *Effects of nuclear matter:* Investigation of quark propagation through cold nuclear matter via nuclear hadronization and transverse momentum broadening employing pion and kaon production in deep-inelastic scattering off a variety of nuclear targets.

- *Dynamics of QCD and the search for exotic mesons:* Study of exotic meson configurations via the tagging of strangeness-rich final states in quasi-real photoproduction.

1.3 RICH mechanical overview

In order to minimize the impact on the existing CLAS12 baseline detectors, RICH modules have been designed to replace (part of) the six LTCC sectors. A first sector is currently under construction and will enter the experimental hall in September 2017 just before the starting of the data-taking of the experiments. A second sector is foreseen to create a symmetrical setup to support transverse polarized target studies. Figure 1.3 shows a three-dimensional simplified view of the proposed geometry for the RICH modules.

In this section the main components of the new RICH will be reviewed starting with a brief introduction on Cherenkov effect and ending with the description of the innovative hybrid geometry adopted. The radiation detection elements and the specification for the readout electronics are presented in the next section.

1.3.1 Principle of Cherenkov detectors

The first observation of the Cherenkov effect dates back to 1926 by Mallet. Eight years later Cherenkov, ignoring Mallet's work, observed again the effect, ascribing to it a nature different from the fluorescence known at that time. Only in 1937 the phenomenon was definitively understood: Frank and Tamm developed the theoretical part and Cherenkov published a paper having completed the experimental study.

On a quality level the effect can be described as follows:

- a charged particle that travels in a medium polarize at every instant the region around,
- polarized molecules or atoms behave as elementary dipoles,
- at small propagation speed (compared with the speed of light in the medium) a complete spherical symmetry exists along the trajectory that neutralize any field created by single dipoles in their relaxation,
- as the velocity increase the symmetry starts to break in the direction of the traveling particle while still exists in the transverse plane. In this case the waves produced by the dipoles has a destructive interference and the field remains null at large distances,
- when the speed of the particle exceed the phase speed of light in that medium, it happens that the waves emitted by the dipoles are aligned in phase along appropriate directions or, in other words, photons are emitted.

By using classical optics (Huygens principle) is possible to demonstrate that light is produced at a precise angle, depending on the particle speed β (in c units) and on the refractive index n of the radiator medium. Neglecting the small contribution of recoil effect on the emitting atom or molecule, photons of wavelenght λ are effectively emitted along the surface of a cone with semi aperture θ_c, with

$$\cos\theta_c = \frac{1}{\beta n}. \tag{1.1}$$

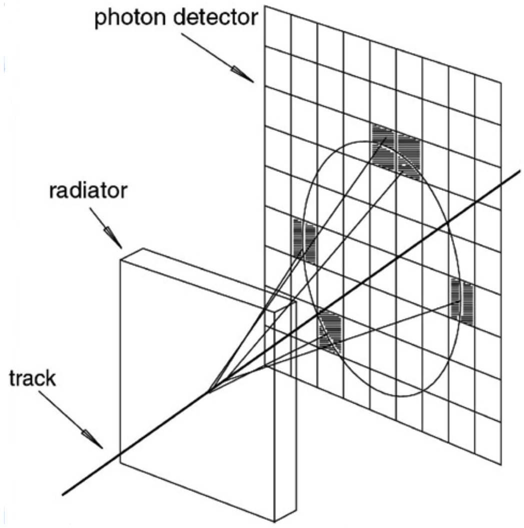

Figure 1.2: Cherenkov light imaging principle

Quantitatively, the number of photons of wavelength λ produced by a charged particle ze in a material of thickness $L >> \lambda$ and refractive index n (homogeneous) is expressed by the relation:

$$\frac{dN_\gamma}{d\lambda} = \frac{2\pi\alpha z}{\lambda^2} L \left(1 - \frac{1}{\beta^2 n^2(\lambda)}\right). \tag{1.2}$$

The emitted radiation intensity thus depends on the wavelength through the factor λ^{-2} and indirectly by the dispersion relation of the refractive index. The latter is less than one in the X rays region (apart from atomic and molecular shell resonances), so the emission is concentrated mostly in the visible region and especially in the ultraviolet portion on the electromagnetic spectrum.

Considering that the speed of a particle depends on its mass and momentum, the Cherenkov emission can be used to distinguish between particles that are traveling below or above the speed of light in the medium. Detector based on this working principle are widely used in Nuclear Physics since many years and are called Cherenkov counters or Threshold detectors.

Alternatively, by knowing the momentum by other means and measuring the position of photons with a photosensitive surface, it is possible to reconstruct the speed of a particle, and thus its mass, from the aperture of the Cherenkov cone. Such kind of detectors were first proposed by T.Ypsilantis and J.Seguinot in the late 70s [5] and are known as Ring Imaging Cherenkov detector or RICH as the photons form a ring that is the intersection between the Cherenkov cone and the photosensitive surface. The principle of RICH detectors is presented in figure 1.2.

If for a Threshold Cherenkov counter the goal is simply to collect the largest number of photons produced by the radiator, in a RICH the position of each photon hit has to be measured with an adequate technique in order to reconstruct the emission angle of the Cherenkov radiation. Thus in a RICH not only the number of detected photons is important, but also the resolution on position and direction measurements, i.e. the error that affects the mapping between photon hit position and emission angle. The number of detected photons depends on many factors, the main ones are the efficiency of the photon detection (quantum and collection efficiency of the sensor) and the efficiency of transportation (radiator transparency and, if used, mirror reflectivity). The single-photon resolution on the Cherenkov angle depends in general on the uncertainty of the photon emission point along the radiator, the chromatic dispersion of the radiator, the photosensor pixel size and the quality of any optical element (i.e. focusing mirrors). The global error on the Cherenkov angle (cone aperture) is of course reduced by the square root of the number of detected photons.

Though first realizations were limited by technology, from the 90s RICH technique has become a mature instrument to identify high energy particles in the fields of Physics, Astrophysics and Medicine.

1.3.2 RICH module layout

According to the CLAS12 Forward Detector geometry [3], the RICH modules occupy the space between the last drift chamber and the time of flight detectors, at a distance of 5.5 m from the interaction point, covering the scattering angles between 5° and 25°. Basically the RICH layout reproduces the LTCC external shape, sharing the same size, position and anchoring brackets. It consists in a trapezoidal box with a major base of about 4.3 meters, a height of 3.8 meters and a depth of 1 meter. To follow the projective geometry of the experiment, it is tilted by 65° with respect to the vertical.

The frame is constituted by different pieces, robust on the lateral sides in the shadow of the torus coils, but lightweight on the entrance and exit panels inside the CLAS12 acceptance. Stiffening elements allow to sustain the instrumentation without significant deformation. The latter have been designed after a detailed study of the detector installation operation in the experimental hall. The RICH will be assembled vertically in a clean room, tested and transported horizontally and finally anchored in the Forward carriage by rotations involving all the degrees of freedom. The total weight is around 1000 kilograms, mostly due to the thick aluminum frame. The elements in acceptance are made by lighter carbon fiber.

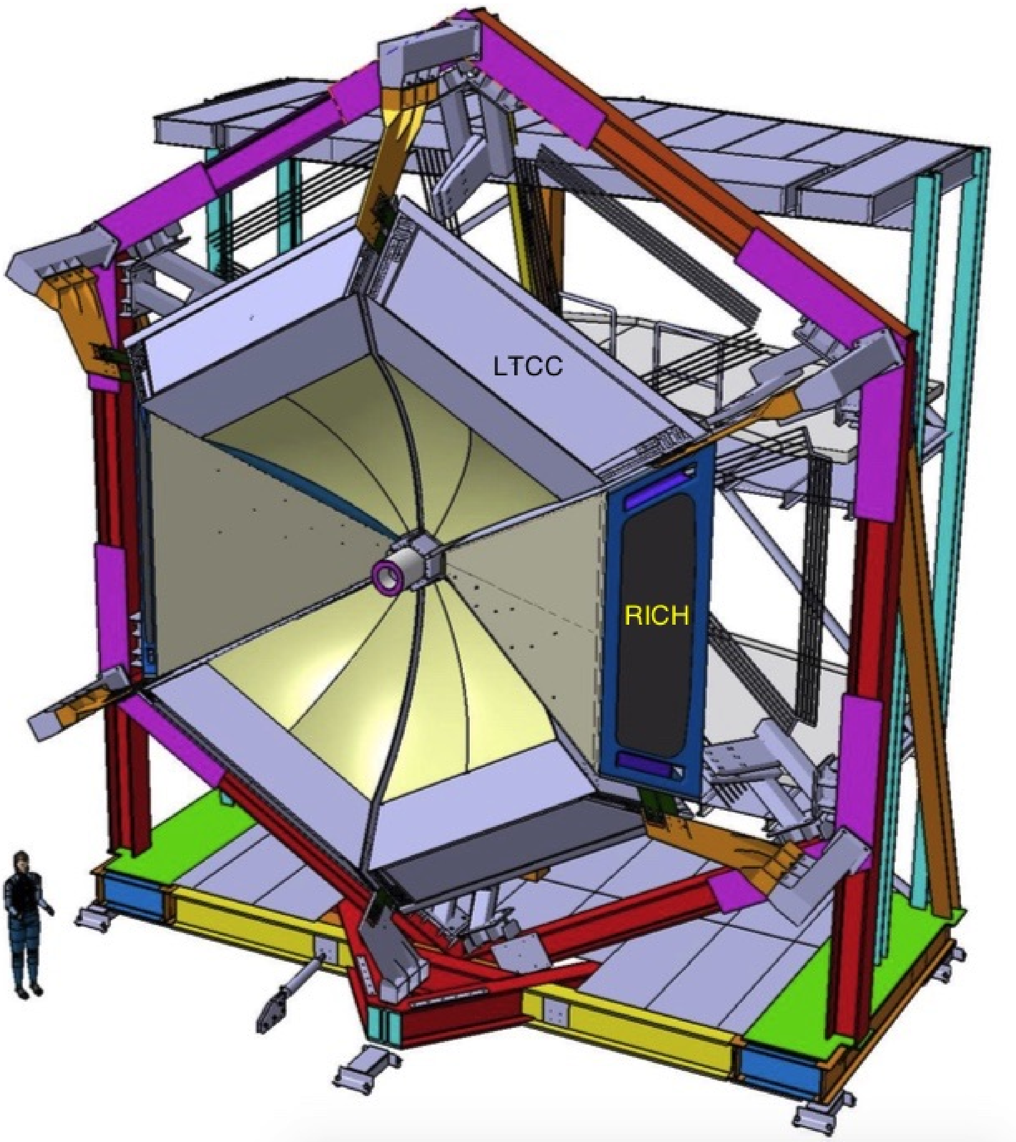

Figure 1.3: CLAS12 forward carriage layout including two RICH sectors replacing LTCC modules for Kaon asymmetry study. Other subsystems have been removed for clarity.

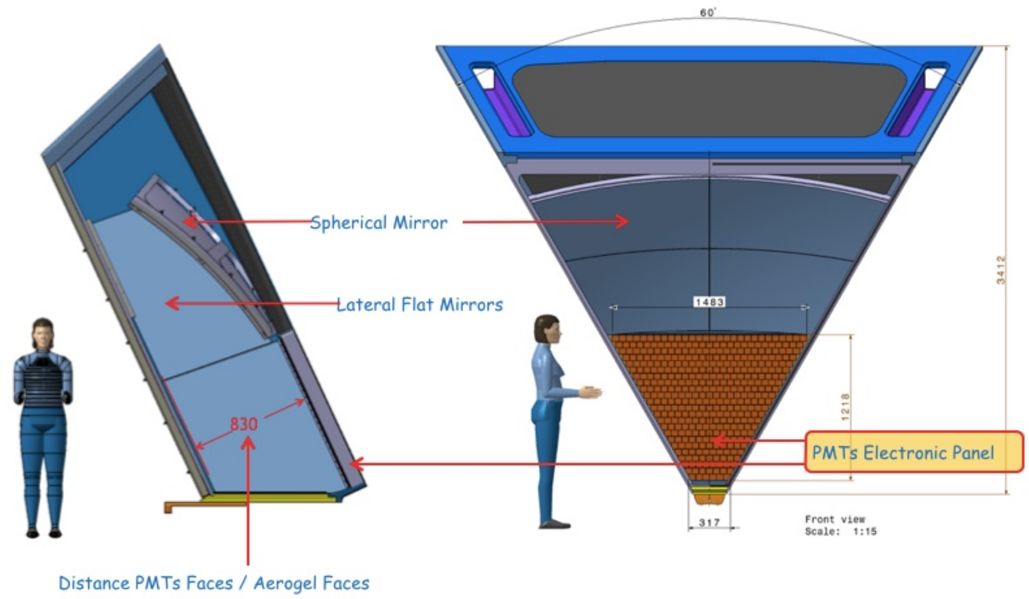

Figure 1.4: RICH Module

The detector can be schematically divided in two blocks. A passive, mostly empty, volume to produce and focus the Cherenkov light and an active element in charge of detecting the photons and reading the information out. For its position, before the TOF and the calorimeter, the RICH is also subject to material budget limitations. A LTCC has a total thickness of $0.032X_0$, while the FTOF scintillator bars have a thickness of $0.12X_0$ and the pre-shower calorimeter a total thickness of $5X_0$. We will take these numbers as a reference, however one should take in mind that, as will be discussed in the following, most of the RICH material budget will be constituted by the photodetectors, that will be located at small polar angles, where the particles have on average higher momentum.

1.3.3 Hybrid geometry

The hadron kinematic distribution expected at CLAS12 is depicted in Fig. 1.5. For momenta below 2.8 GeV/c, the FTOF system provides the required π/K identification. The RICH is designed to extend the hadron identification to higher momenta by exploiting a hybrid optic configuration as described in the following. In order to reduce the area to be covered with photon detectors from several squared meters to about $1\,\mathrm{m}^2$, and thus to decrease costs and material budget, an innovative hybrid geometry solution has been developed using aerogel as radiator material [6].

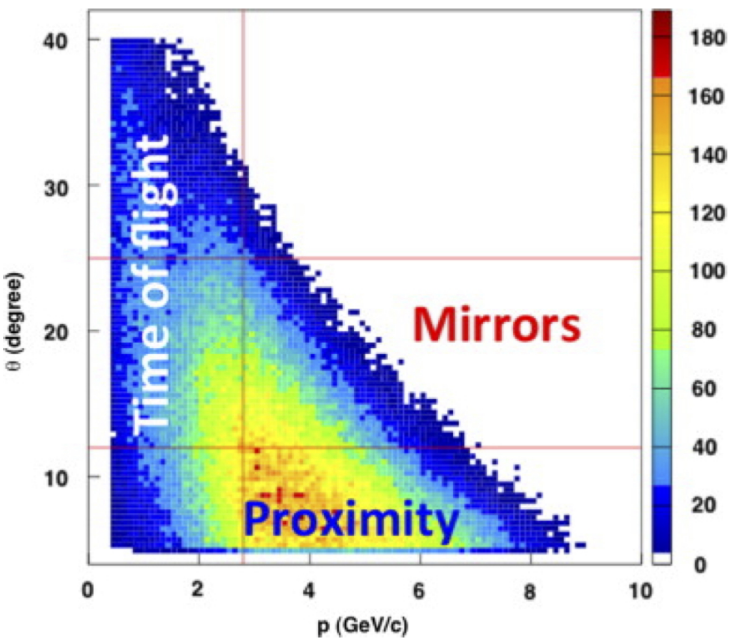

Figure 1.5: Hadron polar angle versus momentum distribution expected in CLAS12. The hybrid geometry RICH extends the hadron separation capability abvove 3 GeV/c momenta providing almost full polar angle coverage. The HTCC complements the π/K separation at high momenta (above 8 GeV/c).

Proximity Focusing

For forward scattered particles (scattering angle $\theta < 13°$) with momenta p = 3 − 8GeV/c, a proximity imaging method is used as shown in figure 5.2. The Cherenkov photons produced by their passage through the radiator material hit the photosensitive surface directly. A similar geometry has been already proposed for the Hall A JLab with CsI photocathodes and perfluorohexane radiator [7]. In the case of CLAS12 RICH the error on the emission point is maintained small by a 1 meter expansion gap.

Mirror Focusing

For particle with larger scattering angles $13° < \theta < 25°$ and intermediate momenta of p = 3 − 6 GeV/c the Cherenkov light is reflected back by a spherical mirror and then redirected on the detection surface by a planar mirror as shown in figure 1.7. This solution has been adopted to match the peculiar geometry of the CLAS12 experiment, derived from the torus layout, and implies a double passage in the radiator material and a consequent higher probability of attenuation and scattering. The longer path of the photons allows the use of ticker aerogel bricks to increase the photon yield without significant decrease of the angular error.

This implies a double reflection for large polar angle particle tracks, thus impose an excellent mirrors quality and radiator transparency in the visible and ultraviolet region to minimize photon scattering contribution to the angular resolution. It implies also a timing resolution at the level of 1 ns to distinguish by arrival time the hits from directly imaged rings and the ones obtained with double reflection. The mixed cases where part of the ring is imaged directly and part is reflected can be identified during the reconstruction to maximize the efficiency.

1.3.4 Aerogel radiator

An excellent angular resolution in the few GeV/c regime, from 3 GeV/c up to 8 GeV/c, is a challenging requirement for a RICH. To achieve good performance in a compact volume (the available expansion gap is about 1 meter) the radiator must have a refractive index in the interval 1.03 − 1.05, a value that can be obtained with high pressure gas mixtures or aerogel.

Aerogel has been preferred because of an easier maintenance and a smaller impact on the design of other detector elements. It is a solid material made of nanometer-scale silica grains filled with trapped air, used in its industrial form as an insulator with excellent physical and chemical properties. The

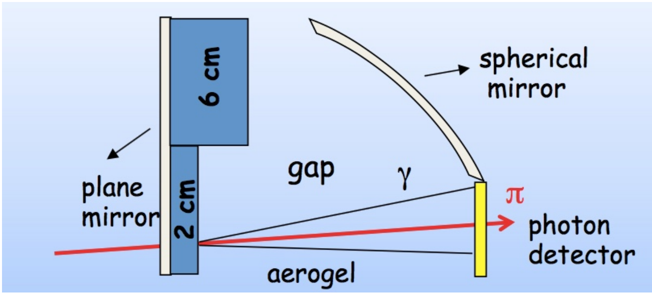

(a) Principle Scheme

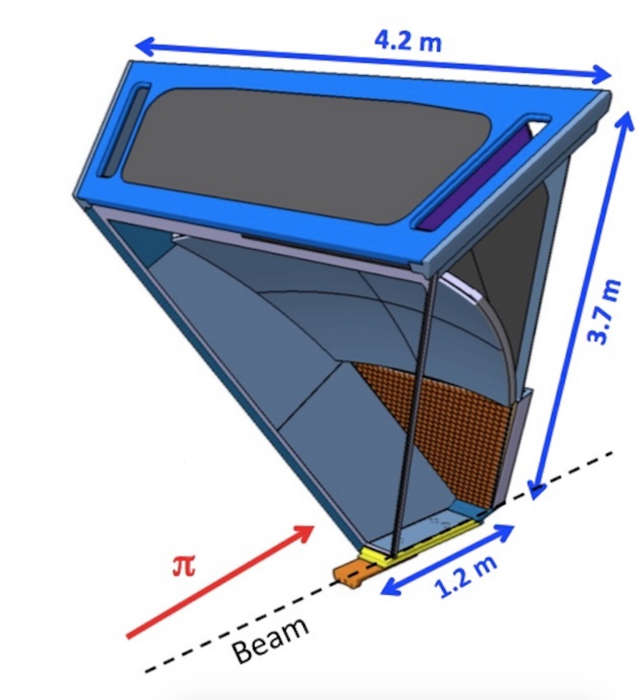

(b) Mechanical Drawing.

Figure 1.6: Proximity Configuration. The Cherenkov cone is directly imaged by the photosensor array for particle with small polar angle trajectories. In the mechanical drawing, the entrance panel with aerogel bricks and the planar mirror, as well as one lateral panel have been removed for clarity.

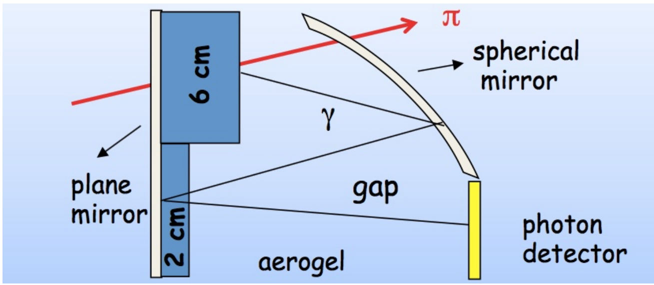

(a) Principle Scheme

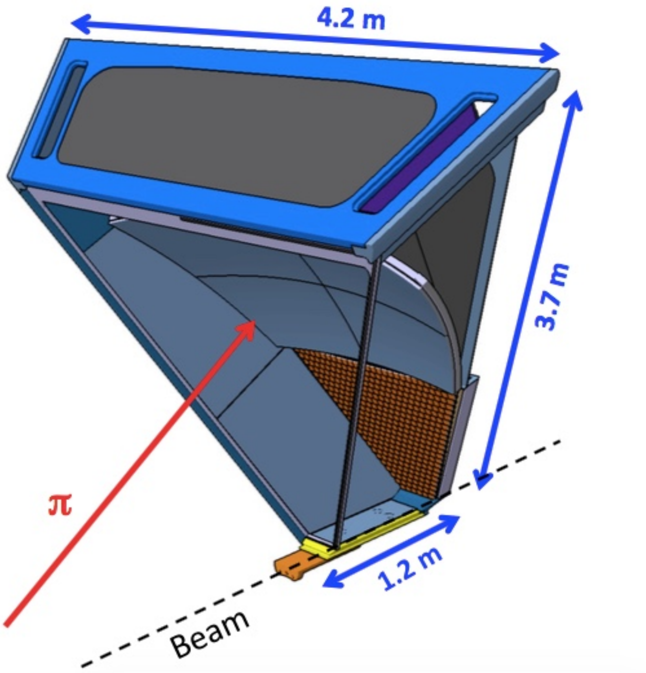

(b) Mechanical Drawing.

Figure 1.7: Mirror Configuration. The Cherenkov light produced by particle at large polar angles is reflected by a mirror system, and reach the photosensor array after two passages in the aerogel.

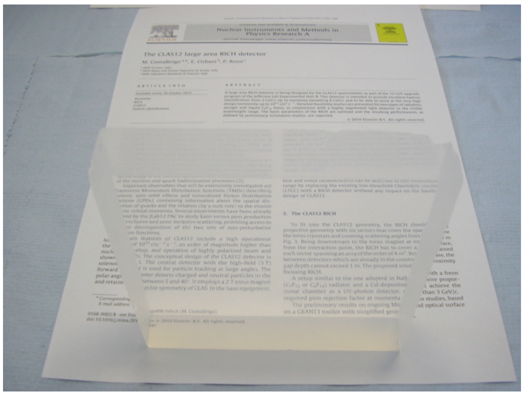

Figure 1.8: Aerogel Tile sample

density, i.e. the ratio between silica and air, is adjustable during the fabrication process and determines the refractive index. When properly produced it exhibits an excellent optical transparency in the visible light regime. In the near-UV regime however, a significant Rayleight scattering is unavoidably generated by the microstructure of the material. During the components validation campaign [8] in 2011-2012, it has been demonstrated that an aerogel with refractive index n=1.05 could meet the CLAS12 RICH specifications.

Aerogel has already been used for the upgrade of HERMES, Belle and LHCb, AMS [9] . As previously mentioned, the thickness of the bricks contributes to the angular resolution through the uncertainty of the photon emission point[1], during the above mentioned prototype study phase, it was demonstrated that the CLAS12 RICH can obtain the desired $\pi - K$ separation using 2 cm of aerogel for the proximity focusing configuration and a 6 cm aerogel in the reflected case (see Section 5.1). Aerogel is a solid and robust material, but is friable and must be managed with particular care. In addition the production process of the aerogel adopted for the CLAS12 RICH is hydrophillic, thus requires a continuous flux of nitrogen at normal pressure to avoid that moisture and impurities could penetrate the bricks altering their optical quality. As a consequence all the feedthrough elements and in particular the electronics panel frame must be light tight and for this are equipped with custom seals.

[1]A possible strategy to overcome the uncertainty due to brick's thickness is to use successive thin layers of aerogel with different refractive indexes to align the rings. This technique is called Focusing Aerogel RICH reported in [10] and [11]

1.4 The RICH active area overview

Given the quality of the radiator element and the one of mirrors system, two elements remain crucial for the minimization of the emission angle reconstruction. They are the number of detected photons per track and the uncertainty on hits position. A large photosensitive surface with high granularity, minimum dead space and excellent single photon readout capabilities is the solution designed for the CLAS12 RICH detector. This active area is arranged on a 1 squared meter trapezoidal electronic panel tessellated with compact detection units that play an essential role in the overall performances.

The choice of light sensor model, the mosaic idea conceived to minimize digital resources and cabling, together with a general layout of the detector services are presented in this section. Specific requirements for the readout system are summarized and explained in the last paragraph.

1.4.1 Photon detectors

The RICH module will be located in CLAS12 outside of the toroidal magnetic field. However, by extrapolating the existing field map calculations, a weak residual fringe of less than $300\,\mu$T is expected in the position where the Cherenkov photons will be directed. Looking at the present position sensitive photon detection technology, this field does not appear a serious concern, neither for solid state detectors nor for vacuum tubes [12].

Different solutions have been considered for the instrumented area during design phase few years ago. For example, matrices of SiPM are compact and robust devices, insensitive to magnetic field, but high costs and high background emission per unit of surface limit their use. In addition their are quite prone to radiation damage [13, 14]. Very promising are also the Large-Area Pico-second Photo Detectors (LAPPD)[15], based on micro-channel plate photomultiplier technology and combining the best advances in material science and front end electronics (e.g. PSEC project [16]). LAPPD represent really the next generation of single photon detection , as the name of the development consortium created in the 2009 suggests, but few more years are required before it became commercially available.

The only affordable solution for the RICH photodetectors has been the flat-panel Multi-Anode Photo Multipliers Tubes (MAPMTs). They offer the required single photon sensitivity, a high packing factor, important to minimize the risk of photon loss and can be placed side by side to create a large detection surface with minimum dead space. Among the different types, Hamamatsu H8500 and H12700 models are the best compromise in terms

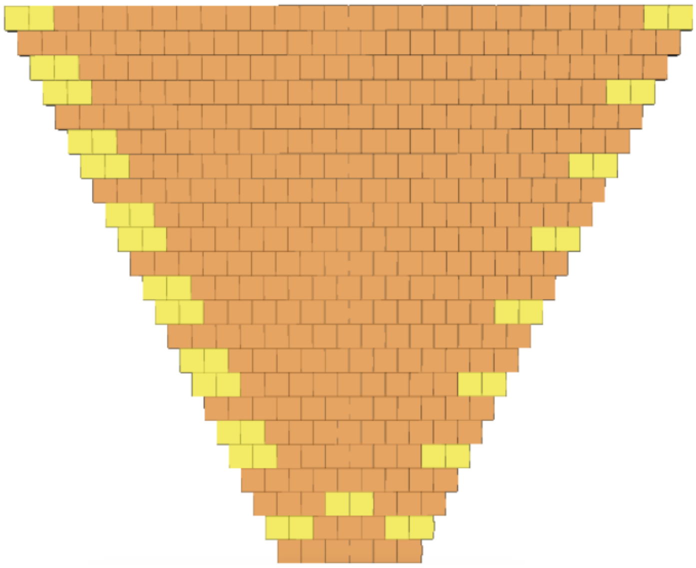

Figure 1.9: Electronic Panel Front View. The photon detection surface will be composed by H8500 and H12700 MAPMTs for a total area of about 1 squared meter, 25024 pixels and only 1 mm gap between sensors.

of costs and performance. They are 8 × 8 pixel matrices with $52 \times 52\,\mathrm{mm}^2$ dimensions and have a high fraction of useful (sensitive) area, close to 90% of the surface. The bialkali photocathode, deposited on a borosilicate glass window, gives a high quantum efficiency (around 30%) compared to other materials. The electron amplifier is done with metal channel dynode structure and is provided with a voltage divider without the need of developing a custom base for the MAPMT. Pixel pitch is 6mm, thus more than the minimum requirement derived from RICH simulation of 1 cm. For both models the high voltage bias for optimum performance is between 10 and 11 hundreds volts. The older H8500 model was originally developed, about ten years ago [17], for position sensitive scintillation counting and have been successfully adopted for PET [18] and mini-gamma cameras [19] in molecular imaging studies. Although not explicitly designed for single photons many studies confirmed the validity of its use at single photon level, for example one from Glasgow University [20]. In response to explicit demand from high energy physics groups the Hamamatsu company has developed a single photon dedicated H12700 model that is substantially a specialization of the H8500 with higher first stage accelerating field and revised collection geometry [21].

Figure shows 1.9 a schematized view of the final assembly, with 391 MAPMT, positioned on a trapezoidal shape that cope with the mechanical constraints. The total number of pixels is 25024 to be acquired with the dedicated electronics.

1.4.2 Electronic panel

Since 25k pixels is a quite big number for a standard approach (with the electronics far away on a patch panels or positioned at the service racks) an *on-detector* solution has been developed for the MAPMT readout. Indeed even shrinking the set of candidate front end ASIC to the ones implementing a differential input circuit, mechanical considerations about the cable encumbrance have determined the choice of *custom* proximity solution. In facts digitization and buffering is performed just behind the sensors and the use of only few fast serial links realizes the connection of the front end with the data acquisition system.

The number of local concentration nodes has been chosen optimizing simultaneously the digital resources and the necessary power lines. This choice is corroborated from the RICH prototype studies that estimated less than 20 photons per track hitting the photosensitive surface. All the electronics hardware resources has been modeled, as a consequence, for low occupancy with benefits on speed, dead time and material budget.

The readout is assembled around a so-called *electronic panel* that acts as a septum between the inner detector volume and the experimental hall. The inner volume of any RICH detector is typically filled with a purified gas to do not interfere with the light propagation or affect the optical elements. The panel could supply several features, from mechanical support to insulation or heat transmittance. In the CLAS12 RICH, a continuous nitrogen gas is fluxed to prevent moisture absorption by the aerogel radiator. The electronic panel has a trapezoidal shape of about 1 squared meter area and 1 cm thickness, and is made of carbon fiber reinforced polimer foils (CFRP) with a honeycomb core to sustain the around instrumentation weight. Role of the support is to provide a planar surface for MAPMT. This flatness is important for imaging the optical flux thus the panel must resist to mechanical stress without plastic deformations. Carbon fiber has been the material choice for construction as it combines lightness and rigidity. Moreover it can be easily worked to creates raised borders for anchoring elements and holes for printed circuit board feedthrough connectors.

On the inner side of the panel, the MAPMTs are mounted onto tessellating boards to provide the sealing against air and light contamination. The front-end electronics and the readout controllers are housed on the outer side, where an effective cooling is possible. The boards are organized in 138 compact units called *tiles*. As previously mentioned the grouping is a consequence of the optimization of the hardware lines: the panel have to receive an adequate voltage supply for the bias of electronics circuits and have to send out the data about its status and optical flux impinging the photosensitive area.

MAPMTs draw typically 200 μA at 1000 V operating voltage. Commercial HV power sources usually supply each channel with a power from 1 to 10 Watts. In principle tens of devices can be fed by a single channel, but for robustness of the system (in case of failure and in case of current anomalies) it is better to keep the number of devices fed by the same HV channel well below this limit. Effective digital resources savings can be obtained by gathering a large number of pixel readout channels on the same transmission line. For simplicity of the design it was decided to have one data line for each power line. Finally, for manageability and possible reuse in other applications, the optimum number of MAPMTs to be gathered was found to be three for a total 192 channels served by a each module. For completing the coverage of the trapezoidal shape of the panel there is the need to also have two MAPMT units so the RICH will be served by tiles of 2 and 3 MAPMTs each.

Cabling within the module, as sketched in figure 1.10, is conducted mostly along lateral raceways to minimize the copper in acceptance. The mosaic idea was exploited to create patterns within the detector cabling, as well at patch panel and distribution boxes to match the RICH tile multiplicity with the rack modules.

Within the detector the high voltage bias is distributed using small diameter coaxial cables. For the power distribution to the electronics a custom solution has been designed with sense cables that arrive at the distribution box positioned on two patch panels and a tailored wire gauge to keep the voltage drop within the detector below 0.25 Volt thus minimizing the contribution to heat production along the lateral raceways.

Transport of the event data from the front end cards to the event builder network is done using a multicore optical fiber cables that serve groups of 4 tiles each. RICH will not be part of the trigger logic scheme of CLAS12.

1.4.3 Electronic requirements

Having in mind the need of a complete compatibility with the general CLAS12 architecture, the electronics calibration, monitoring and readout systems of the RICH have to be designed following general principles that are itemized here and whose implementation is described in detail in section 2.2.4.

- *Simplicity*: Already existing infrastructures for data transport have to be reused. RICH will interface directly with JLAB Sub System

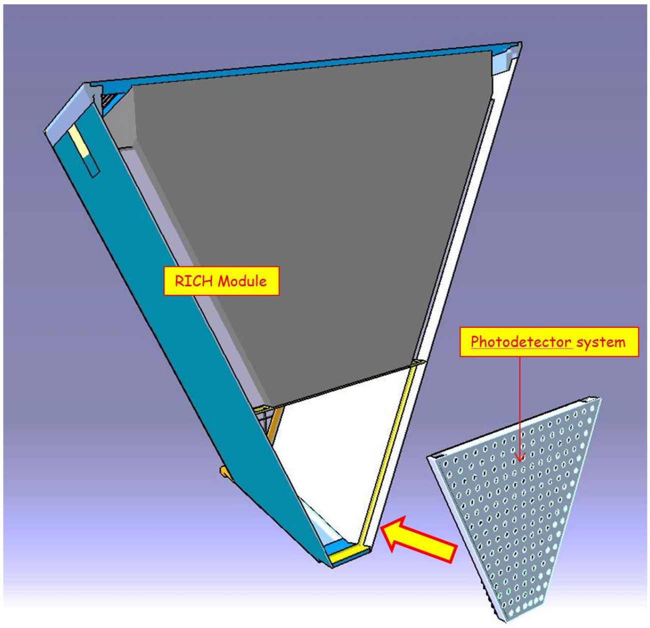

(a) Electronic Panel Position

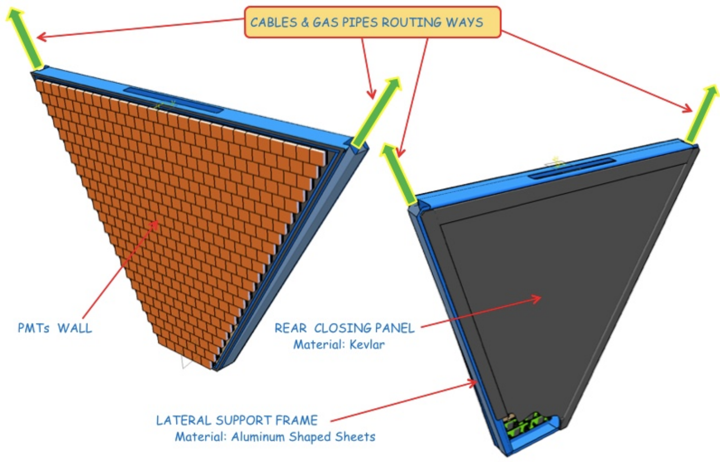

(b) Front and read view of the electronic

Figure 1.10: Electronics panel supporting the active area of the RICH detector. Sensors and Electronics are in the acceptance. Power and data cabling as well as and gas pipes routing is realized along later raceway in the shadow of the forward detector frame.

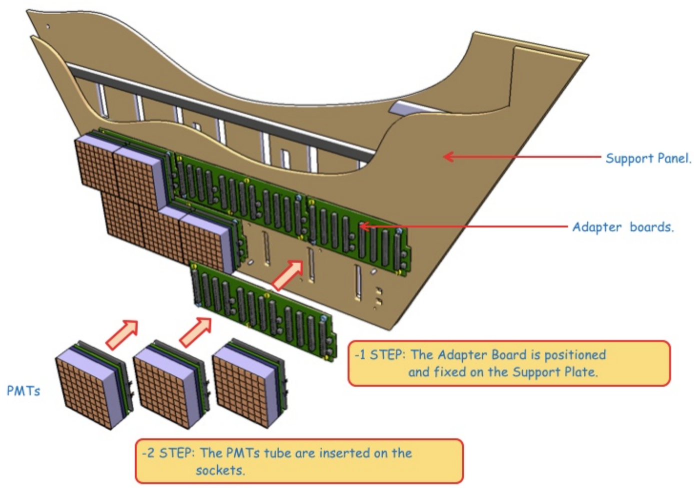

Figure 1.11: Electronic panel mounting sequence (simplified)

Processor Boards (SSP) that will provide synchronization signals and clock with a precision of 1 ns. The trigger for building the events is distributed by the SSP with a maximum latency of 8μs along the optical fibers.

- *Flexibility*: Whenever possible the functions have to be implemented at software level before in-situ programmable logic. The latter of course have to be used for implementing solution that cannot be provided by non-programmable elements.

- *Automation*: All system should be running unattended or with minimal human intervention. Automation should be minimal at the beginning but capable of being developed as the operation experience is gained.

- *Autonomy*: RICH should be capable of running autonomously as far as possible without the need for automation systems or global infrastructure. This holds for the single tile too that must have the possibility to be used independently from the others for testing, debugging and in general during all the prototype phase.

- *Reliability*: RICH electronics should be reliable and fault tolerant with fast diagnosis tools.

- *Low costs*: The total cost of the RICH electronics including cabling and service equipment should be as low as possible.

- *Local Running*: Local running will be extensively used during commissioning and beam shutdown periods. Runs with or without recording data should be possible as well as partial readout of the detector. The local running should reproduce the condition of global running as closely as possible and exercise the same hardware and software becoming a powerful tool for diagnostic and set-up.

As a conclusion of this first chapter the specific requirements for the RICH detector readout electronics circuits are summarized here. Some of them are related to the MAPMT signal processing, others are imposed by the data acquisition system of CLAS12, others are related to small space available and to he inaccessibility of the electronic panel during the long data taking periods.

1. a RICH sector will have about $25k$ channels. The electronics must provide the same amount of readout channel.

2. Electronics must be single photon sensitive. This translates to a minimum detectable charge at the level of 1/3 of photo-electrons. Considering a minimum MAPMT gain of 10^6 electrons the electronics must provide 100% detection efficiency for signals greater than 50fC

3. Channels shall be considered independent. In order to do this the cross-talk between electronics channel must be smaller than photo-detector cross-talk. A level of few % is considered acceptable.

4. The electronics shall be able to compensate the gain dispersion among the anodes of the MAPMT that typically is $1:2$ but can be as high as $1:4$

5. Time precision must be at the level of 1ns in order to be able to separate direct photons to from reflected ones.

6. Expected trigger rate in CLAS12 is 20kHz and maximum latency of 8μs. The readout shall be able to sustain such a rate with dead time smaller than few % and have to keep on a local buffer event data occurred up to 8μs before the trigger is issued to the front end by the logic of the experiment. The probability of soft errors (data corruption) shall be small or compensated by adequate parity checks.

7. RICH detector must have a minimum impact on the downstream detection elements like FTOF. This implies that a maximum temperature of $30°C$ has to be reached on the exit panel which is close to the bars and

the readout elements of the FTOF. In addition cabling material budget in acceptance must give a negligible contribution compared with the MAPMT array.

8. Availability must be as close as possible to 100% over the entire spectrometer life cycle. This means that all the components must tolerate the radiation field present in the spectrometer volume without deteriorating the performance. Recovery operation for the configuration bit stream corruption of the programmable parts have to be fast and compatible with the CLAS12 operation.

9. Detector installation in the spectrometer can be a long operation (can take days). Is a fundamental requirement that the detector have tools for monitoring the performance in-situ

10. Compactness both of electronic board itself and of cabling that convey signal to the external modules

11. Maximum reliability because the cards cannot be physically accessed during data taking

12. Remote configuration and debug. Again due to inaccessibility the electronics must be configured and tested as much as possible through a remote system

Chapter 2

Readout system design

2.1 Goals

The purpose of the project is to design an electronics module for the read out of multi-anode photo-multipliers tubes (MAPMT) working at single photo-electron fully compatible with the CLAS12 hardware and software architecture. Many of these modules, disposed in parallel and tessellating a large trapezoidal surface, will realize the active element of a Cherenkov light ring imaging detector (RICH) dedicated to improve the particle identification system in one of the JLAB experimental halls.

If on one side the module have a specific use, the single photon imaging is a technique used in a wide range of applications that goes beyond the fundamental physics studies. It's not hard to find examples of its usage in human health technologies or in biology experiments, whether or not coupled with the use of scintillators to shift the imaging sensitivity in the range of high energy photons.

Our modular compact multi-channel design arrived at the end of an intense prototype testing phase that validated all the required features for its use in CLAS12 RICH, whether in terms of electronics, mechanics, thermal or speed performances and could be potentially interesting to serve as readout electronics in other experimental conditions. In facts to develop and fully test the prototype units a small configurable setup has been adopted with a standard PC directly connected to the assembly using a TCP/IP communication protocol. The developed software tools, that allow a full exploitation the potentialities of the hardware resources and that were used for the validating tests, will be presented in the central part of the chapter. The first two sections are dedicated to the hardware resources and integration of the modules in the CLAS12 environment. In the rest of the chapter the main

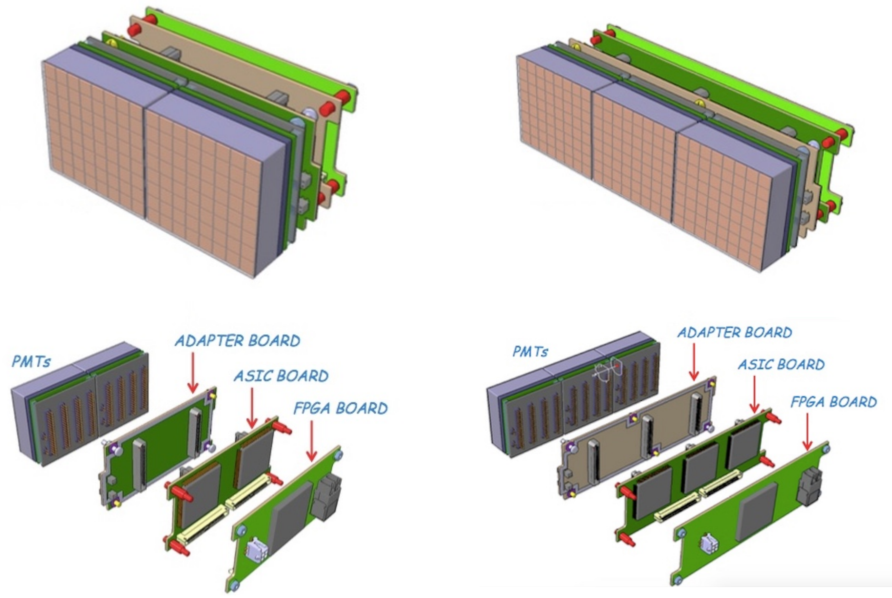

Figure 2.1: MAPMT tile assembly mechanical drawing (2014)

operating modes are presented showing the potentialities and the autonomy offered by the design.

2.2 Hardware Resources

Each readout unit is organized in a stack of three boards that can be optimized or upgraded separately. In practice this is a good compromise between geometry and cost when a limited space available impose the printed circuits to be parallel to the sensor surface and the number of routing layers cannot diverge. The use of rugged board-to-board high speed headers allow to split the functions on different printed circuit but, to operate like on a single extended surface. The three boards carry out different functions that are listed below and described in the next paragraphs:

1. The ADAPTER board is for the mechanical and electrical matching with the sensor and detector geometry.

2. The MAROC board is for the digitization of current pulses produced by the single photon hits.

3. The FPGA board is for configuring, controlling the front end circuits and interfacing them with the data acquisition node

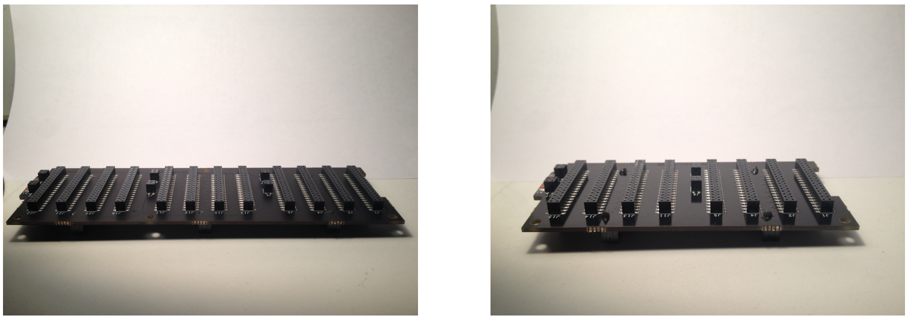

Figure 2.2: ADAPTER board, 2 MAPMTs variant, INFN Genova, 2014

The assembly have to be provided with power and data cables only resulting in a very compact photon detection module tailored for MAPMTs as shown in figure 2.1. Because of the modular design the units are called *tiles* and can be in principle used to tessellate arbitrary large surface or more complicated geometries.

2.2.1 The ADAPTER board

The task to match light sensors with the front end electronics is a crucial element for any readout system, including the ones in which these two elements are embedded in the same device. Considering the CLAS12 RICH, the adaptation should also accounts for MAPMT mechanical support, high voltage distribution, optical and gas sealing.

A passive feedthrough board, called ADAPTER, has been designed to be mounted on the inner side of the electronic panel. The board comes in two variants, to house 2 or 3 MAPMTs respectively as shown in figure 2.2 Shape is rectangular with dimensions that replicate exactly the MAPMT base providing a minimum dead space between sensors. A small extrusion and a correspondent cut off had been necessary to achieve a 1 mm gap between MAPMTs in all directions when mounted on the panel because of the dedicated high voltage pins of the MAPMT socket. The ADAPTER receives one high voltage power line and distributes it to groups of MAPMTs (2 or 3 depending on its version). The HV connector is a 3 pin model polarized with a two 10 MΩ resistors that keep the voltage between adjacent pins always at one half of the MAPMT operating voltage.

As specified by the manufacturer, there is no light sealing in the MAPMT base so the ADAPTER boards are painted black and surrounded by a black custom rubber sealing (Viton). As a further prevention against light transmission, all the mounting holes of the connectors could be eventually sealed using a small black silicon deposition after the assembly.

Anode signal paths are kept as short as possible to minimize their reactance. Special attention has been taken to map neighbor anodes in separated readout channels. With this expedients the cross-talk introduced by the electronics can be decoupled from the one of the multi-anode sensors.

2.2.2 The MAROC board

In a modern readout system each detection element (pixel) is served by an independent front end circuit responsible of signal processing and digitization. High performance multi-channel apparatus like CLAS12 RICH make often use of an ASIC coupled with a programmable device, the first providing a highly specialized function, the latter giving flexibility, versatility and buffering resources. Among available ASICs designed for single photon sensors readout (e.g. MAROC [22], CLARO [23] , DREAM [24] , etc.) the choice has been placed on MAROC since its specifications fulfill all the CLAS12 RICH requirements, because of the existing expertise within the Collaboration and for its mature stage of design.

Multi Anode Read Out Chip (MAROC)

MAROC is a 64-channels, BiCMOS 0.35 μm integrated circuit designed by Omega Group of IN2PR3-LAL (Paris, France) for the ATLAS experiment to readout fast negative current pulses such as those provided by MAPMTs. As shown in figure 2.3, the chip consists in a highly configurable system dedicated to signal discrimination and charge measurement. The first is a prompt operation with parallel binary output while the latter, offering information about pulse height, is slower and serial. Each channel has a preamplifier followed by two shaping sections. One, preceding a comparator and called *fast channel*, is intended to produce reliable signal discrimination for pulses above 50 fC, the other, called *slow channel*, offers a linear response in a wide range of charge and is followed by a sample-and-hold circuit.

The chip can be configured using a 829 flip-flop shift register and allows individual channel probing thanks to a second shift register, 64 bits wide (called *static* and *dynamic* respectively). Both registers can be daisy chained for saving pinout resources in case of large systems. Each individual channel preamplifier is a low-offset low-impedance adjustable current mirror. Its gain can be tuned in the range 0 to 4 with 8 bits resolution allowing for an optimal detector gain spread compensation; once equalized each pixel injects on average the same amount of current in response to single photon. An embedded 10 bits DAC is employed for tuning the discrimination threshold accordingly to the desired sensitivity. Two operating modes are available for

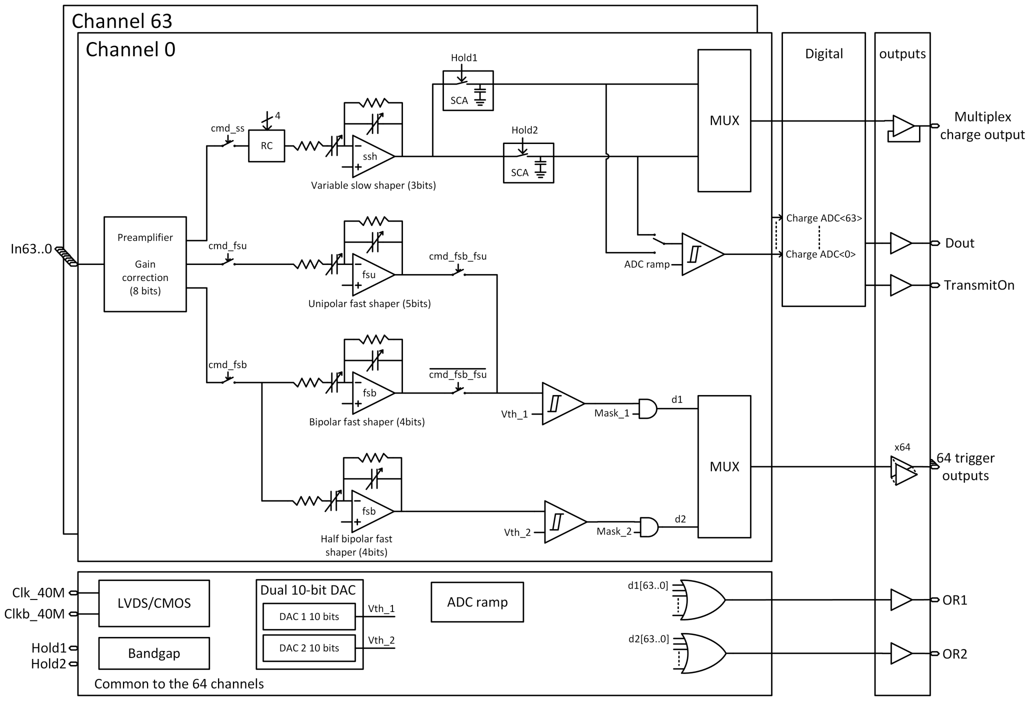

Figure 2.3: MAROC3 block scheme

Specification	Description
Version	MAROC3A
Detector Readout	MAPMT, SiPM
Channels	64
Dimension	16mm^2
Packaging	PQFP240 (240 pins)
Technology	BiCMOS SiGe $0,35\mu$m (AMS)
Signal Polarity	Negative
Sensitivity	100% efficiency above 50 fC
Time Resolution	$\leq$ 40ps at 1 pC
Dynamic range	up to 5pC with 2% integral non linearity
Inputs	64 analog + 1 channel test (CTEST)
Outputs	64 binary + 1 masked OR
	1 charge (12 bit ADC, multiplexed)
Configuration	Individual gain, range 0 to 4 (8 bits)
	Common threshold (10 bits)

Table 2.1: MAROC features summary

the DAC, a full-scale allows to span the entire pulse height of the fast shaper output while a reduced scale is intended for finer adjustments in the low charge discrimination region. For optimizing the match with sensors and fully exploit the dynamical range all the shaping amplifiers have a configurable feedback network with peaking time 15-25 ns for the fast channel and 60-100 for the slow one.

MAROC offers great versatility not only in view of the highly configurable analog processing section, but also for the options available on its digital output stage. Charge is digitized by using an embedded ramp ADC with adjustable resolution. The choice among 8, 10 or 12 bits is a compromise between resolution and speed. Maximum conversion time is a bit less than 100μs for 50 pC. The binary parallel output polarity can be selected to be compatible with any subsequent stage device. A masked OR of the 64 parallel discriminated outputs is also available for minimum latency triggering in case of data driven acquisition.

In addition, a test input pin connected to the preamplifiers through a logic network of switches and 2 pF capacitors (not shown in figure 2.3) can be used for response characterization in absence of the detector element (CTEST) using an external step function generator. A summary of the MAROC features is presented in table 2.1.

MAROC in CLAS12-RICH

Usually the binary output is used in imaging systems as topological trigger for realizing efficient event selection at hardware level. In single photon applications and specifically in the CLAS12-RICH physics quality runs, where the hit multiplicity per event is small and the arrival time precision has greater importance than the amplitude the binary output is the primary source of information about the optical flux impinging the photosensitive surface while the autotrigger will be used for monitoring the sensors only.

The main reason to that is the CLAS12 trigger maximum latency of $8\,\mu$s. This is a too large value the use of the MAROC slow channel (charge measurement) during physics runs of the spectrometer. Since the RICH technique is ultimately binary and the time precision of the MAROC is better than the photosensor even if the chip was not explicitly designed for timing, this choice appears perfectly adequate. Moreover the binary output have a much smaller impact on data throughput of the apparatus. The price to pay, in absence of any shape information, is the need of a complete knowledge of the discrimination properties in order to digitize the light flux in a reliable way.

Charge information can still play an important role in the apparatus cal-

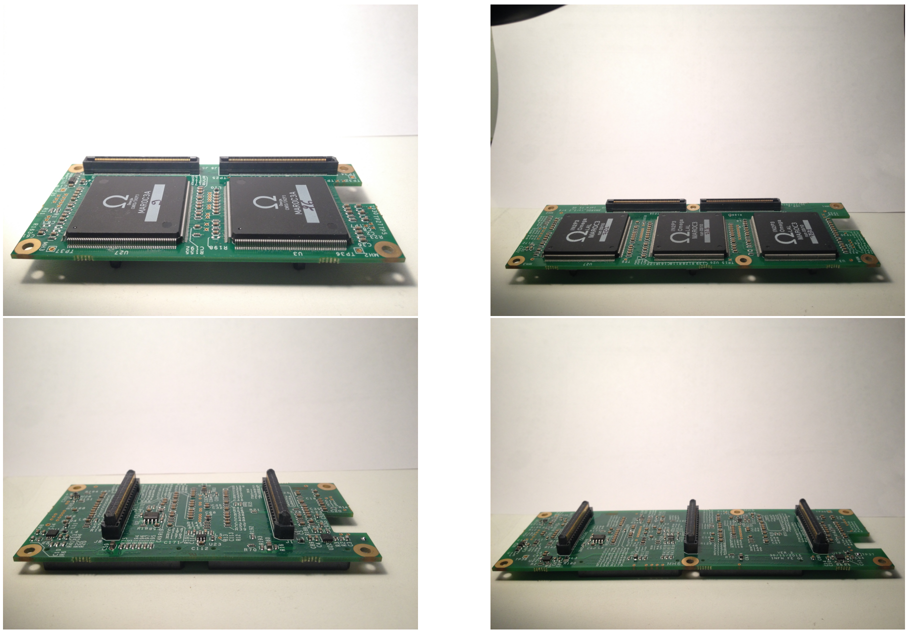

Figure 2.4: MAROC boards layout view

ibration. Indeed the charge measurement linearity, extended in the whole MAPMT output range, offers a powerful mean for characterizing and debugging the electronic response after installation in the spectrometer. For example, the MAROC self-triggering capability can be used for capturing the thermal noise of the sensor (typically few tens of Hz per pixel in case of MAPMT) and characterize the electron multiplier gain *in situ* during the life time of the experiment.

MAROC board description

The board that houses the front-end chips is called MAROC board. This is the middle element of the readout unit stack and converts the analog signals from the sensors into digitized information for the acquisition node. It houses voltage regulators for chip biasing and a test pulse circuit. It is strongly coupled with the controller unit and shares with it a dense board-to-board contact, not only for data and control lines, but also for receiving form it the power supply. This latter choice goes in the direction of cabling reduction and reinforces the unitary vision about signal processing: have a compact unit dedicated to single photon acquisition with minimized external connections.

Low-voltage power supply (+5 Volts) is fed into four linear regulators to produce stable voltage references for the on-board chips. MAROC requires

Line	Resources [Number of pins]
Power supply (+5 V)	11
Common reference (GND)	42
Binary outputs	192
OR outputs	6
ADC measurement	12
Static register	4
Dynamic register	6
Test pulse	4
TOTAL	277

Table 2.2: Usage of the interface connector between MAROC board and FPGA board, the identical pin assignment for the two front end variants allows only one firmware development

standard TTL for the digital section and slightly more for the bias of analog part (3.3 and 3.5 Volts respectively). The binary output levels are are VHSTL, custom values have been chose to cope with the FPGA discrimination threshold with the minimum reliable swing (1.2 V and 0.6 V).They are generated by two identical regulators (*TPS79501DRB*) conditioned with different passive feedback networks. The total current absorbed is pretty small, around 55 mA/chip or 0.86 mA/channel.

Actual ASIC version used is MAROC3A, available at the moment of design in a 240 pins Quad Flat Package[1] (*QFP240*). Inputs are bonded on one side while binary outputs are on the opposite side. All of them are single ended signals referred to the same ground level. Remaining pins, on the other two sides of the package, have bias and control functions. Every ASICs is mounted on the MAROC board with the same orientation, with the binary outputs close to the connection with control unit. The large package, 35×35 mm^2, occupies a substantial fraction of the board surface. As a consequence the space for additional components and circuit routing is limited and special care has been taken in order to minimize cross-talks among the lines or digital signal induction on the sensible analog inputs.

The MAROC board accommodates an adjustable test pulse circuit implemented with a single logic gate (*74LVC1GU06*) and a 10 bit programmable DAC (*AD5620BRJZ*). The logic gate is driven by a standard *TTL* signal and its output voltage can be modulated by the DAC before entering the

[1]Future fabrication runs will adopt a smaller Ball Grid Array (BGA) package, 12 mm side and 0.5 pitch, helping the routing at an increased price

CTEST pin of the MAROC where is it converted in a fast current pulse by an embedded 2 pF capacitance connected to the input preamplifier.

The described MAROC board comes in two variants of 128 and 192 channels sharing an identical interface with the controller. This choice permits to have only one FPGA board, with only one version of the firmware. As previously mentioned, the front-end and the controller board form a single functional unit, that is the reason why the connector between them is so important. Table 2.2 lists the amount of pins dedicated to each function. The majority of lines are used by MAROC digital outputs, power supply and common voltage reference. The other connections are dedicated to configuration and control lines. MAROC static registers are daisy chained on the board and thus require only 4 pins. Test pulse requires 3 lines for serial configuration of the DAC and one for driving a logic pulse. Finally 12 pins are devoted to the MAROCs internal ADC control and readout.

2.2.3 The FPGA board

The third element of the RICH electronic assembly is a board that acts as controller unit. It mediates the information exchange between an external data acquisition node and the front-end. Specific tasks are the translation of configuration parameters, the data aggregation and readout in response to commands or signals. The board is built around a FPGA device to allow maximum versatility in terms communication of protocol choice and features addition or debug, especially as the design evolve.

The FPGA is chosen among the Artix-7 family for its low power consumption, small form factor and, of course, adequateness in terms of I/Os and digital resources; all attractive features when a small space is available and compactness of the entire unit is essential. The Artix-7 is complemented by a not-volatile memory (EEPROM) that stores the firmware image onboard allowing self initialization at power up.

The board is provided with a small form factor optical transceiver (Finisar Endurance-FTE8510N1LCN duplex LC) for high speed communications, likewise performing in terms of power consumption, thus adequate to contain the board within the mechanical and thermal specifications.

The use of different technologies impose the presence on boards voltage regulators and translators to provide a correct and stable reference to all the chips and use the proper signal range for signaling. An example is the transceiver that requires a 3.3 V voltage bias for its functioning and a level shifter (from HSTL - used by the FPGA- to TTL) for its configuration. Voltage regulator are also mandatory for the FPGA block RAM (1.0 V) and MGT (1.0 V and 1.2 V). The most used voltage on board is the 1.8 V for

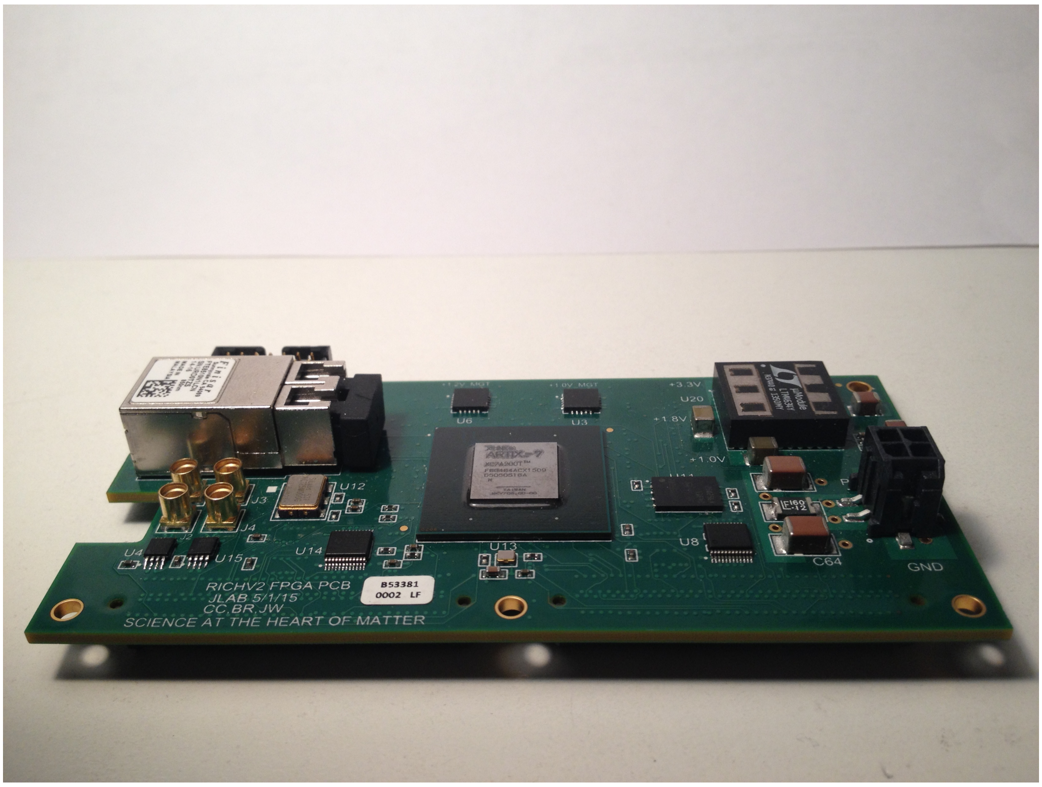

Figure 2.5: Fpga board. An optimized organization of the pin out connector allow to have one single FPGA unit to readout both tile variants i.e. 128 and 192 channels.

the FPGA itself and the EEPROM. In total the current consumption of the board is of the order of 700 mA at 5 V depending on the working condition.

The board is completed by a local 250MHz clock source and a JTAG port that allows flashing the firmware image directly on the FPGA or burning it into the EEPROM. Four miniature micro-coaxial connectors (MMCX) allow to interface the board with other devices for testing purposes. For example they can be used to drive an external pulse generator or a laser unit. Their I/O standard is TTL and have been precious to synchronize the unit with an oscilloscope for checking the front-end response by probing the many test points available on the MAROC boards. They are intended purely for testing and will have no use in the final system since all the information will go over the optical fiber link.

The FPGA board has been realized with the same dimension of the 2 MAPMT variant of the ADAPTER, but it supports both versions, up to 192 front end channels with the same firmware.. Board layout is illustrated in figure 2.5.

2.2.4 Integration in CLAS12

The RICH front end electronics will be positioned inside the detector module and connected with the external through power and data connections using a couple of patch panels out of the acceptance. The readout control elements as well as the power supplies and gas system services will be positioned 15 meters away from the module in the Electronics Trailer of the experimental Hall.

Readout

The RICH will enter the CLAS12 data acquisition system interfacing directly with Sub System Processor (SSP) boards that are existing JLAB modules participating in the L1 trigger logic of the experimental Hall. Five SSPs are needed for the 138 tiles of the RICH sector, they are housed in a VXS crate connected with the central controller of the experimental hall by means of a 200 MB/s copper link.

Each SSP is provided with 32 full duplex optical fiber link for high data transfer rate, 4GB of memory buffer and is in charge of distributing the clock, the trigger and the synchronization signals to the RICH front end boards.

Considering the transmission capacity of the VXS crate and that the physics run trigger rate is 20 kHz, about 10 kB per event or can be extracted without introducing dead time. This amount of information corresponds to 2.5 kwords using the current data format. As the total number of channels of the RICH electronic module a theoretical maximum occupancy of 10% can be sustained, something less including the overhead. This performance is more than adequate for the RICH application because the expected occupancy due to Cherenkov photons is less than 1% (actually 0.1%).

For running condition different from physics run, i.e. calibration and monitoring, that could have a larger amount of data the system is adequate, accepting few percent of dead time.

Power supply

A single tile consumes around 4 Watts. An adequate voltage power supply should be provided to the electronic units. Photon sensors require an high voltage line drawing few hundreds of μA in the working range from 1000 V to 1100 V that will be routed along the two services raceways with micro coaxial cables. Each controller unit requires about 1 A at 5 V, supplied by AWG20 copper cables, and therefore consumes about 5 W. A remotely accessible CAEN SYS4527 power supply will be used to drive both the low- and high-voltages. More detail on the power distribution system can be found in the appendix.

The heat load has been carefully studied. As shown in figure 2.6 the warmest element is the FPGA. This unit is certified to work up to 85 Celsius degrees and may undergo damage if the temperature is greater than 125 Celsius degrees.

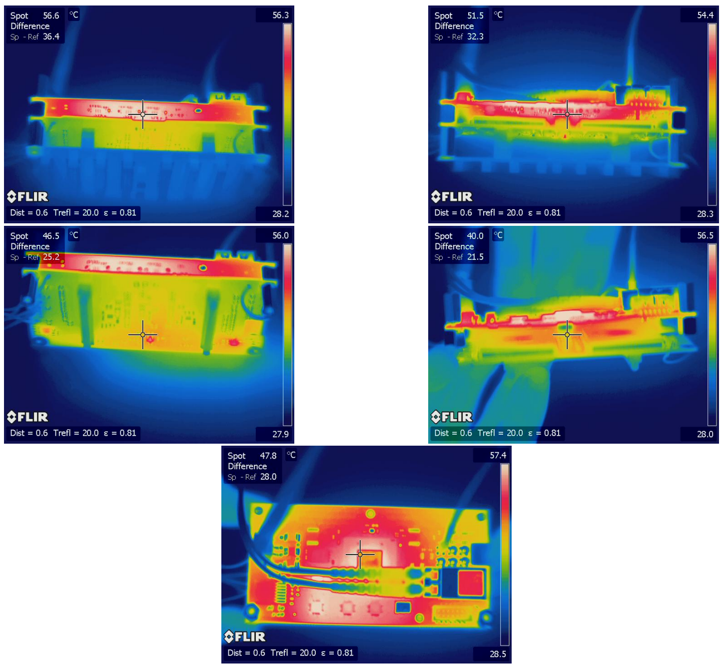

(a) wsrite me fpga

Figure 2.6: Thermographic camera pictures, color scale pretty reliable.

The total power dissipated at the electronic panel is about 500 Watts. To avoid perturbation on the RICH itself and adjacent detectors, the thermal load should be minimized and temperature controlled. The volume surrounding the electronics is limited and almost thermally isolated, and can not be accessed without disassembling the RICH detector. As a consequence a reliable cooling system has been tailored and complemented by a sophisticated slow control and interlock systems.

Slow Control

In addition to the distributed temperature information, dedicated temperature sensors will be placed in relevant positions along the electronic panel, cooling circuit and adjacent detector. A compact-Rio control unit will take care of collecting this data together with the status of the cooling line (flow meters, pressures and air compressor status) stabilizing the temperature of the readout circuit. This module will be connected with the CLAS12 computer through an Ethernet interface to pass all the information to the slow control program.

Supply Voltage and current values are also transmitted by SY4527 to the compat-Rio and to the CLAS12 slow control monitor. To minimize the possibility of oscillations in the feedback network due to finite propagation time, the voltages are regulated on board. For safety reason each channel is enabled only if simultaneously enabled by the control program in the data acquisition computer and by the interlock system of the front-end.

In case of alteration or emergency, the compact-Rio immediately takes the programmed actions to avoid data corruption or hardware damage and the relative information is passed to the slow control monitor of the experiment.

Complementary information on detector status consists not only in the power and cooling system monitors but also in the correctness of the configuration data. Dedicated tests during the development of the readout electronics assessed that a 10 years integrated fluence at full luminosity has low probability to create permanent damage to instrumentation. The passage of particles can alter the configuration register content positioned in acceptance creating unexpected behavior. As a consequence, a system to control the correctness of the configuration data is mandatory. A dedicated check can be performed to detect and eventually correct possible bit upsetting during CLAS12 operations. It consists on the comparison of the read-back register content with the expected configuration pattern.

2.3 Firmware Resources

The firmware is the operating system of the tile assembly. It is a microcode (bitstream) describing sequential and combinatory logic operations to manage the on board resources in a versatile way, in fact it can be upgraded without modifying the hardware resources as the design evolves. Once loaded in the configuration memory of the FPGA device, the firmware allows the information and commands to be transferred by means of read and write operations on appropriated registers.

Starting from the MAROCs configuration, many features has been added to support the testing and to prepare the RICH electronics for the integration in CLAS12. At the moment of writing the following features are supported:

- TCP/IP communication protocol
- MAROC registers configuration
- Counters for a quick control of the discrimination performance (scalers)
- Pulse burst generation with adjustable frequency and duty cycle
- Trigger logic management with internal, external or data driven modes
- Event building with up to 8μs latency from trigger
- Charge measurement using MAROC embedded ADC
- Time measurement of the MAROC binary outputs with 1 ns resolution (TDC)
- Temperature and voltage monitors
- Module for radiation tolerance test
- Serial Peripheral Interface (SPI) with the flash memory device

The chosen Artix-7 device has 9Mbit of configuration data (bitstream length), stored on board in the associated EEPROM device and loaded at any power up. During the development a JTAG port allows to flash the EEPROM, in the case of CLAS12 the operation will be done using the optical fiber link as well as data transfer, clock, trigger and synchronization signals. For a greater robustness against bitstream corruption, multiple compressed bitstream will be held in the EEPROM device that has a capacity of 16Mbits. Periodical reconfiguration will ensure the proper functioning of the unit.

2.3.1 Event Data Format

In order to minimize the porting effort when moving from the bench to the experimental hall setup the adopted data format utilizes the same encoding scheme defined for other JLAB boards (e.g. FADC250). The word length for is 32 bits and the total event size depends on the number of channels involved.

Data words are divided in two categories: the *Data Type Defining* (DTD) word that specifies the kind of information carried and the *Data Type Continuation* (DTC) word to provide additional data payload to the last specified data type. DTC words permit to span multiple words allowing for an efficient packing of various data types. The types used for the RICH event readout are:

- Event Header indicating the start of an event and including the trigger sequential number and the identification of the FPGA device to ensure the proper alignment for the event building.

- Trigger time specifying the time interval from the most recent global reset. It is measured by a 48 bit counter that is clocked from the 250 MHz system clock. This information is essential to ensure synchronization and proper alignment of event fragments coming from different electronic tiles.

- TDC hit containing the indication of the channel involved in the event, hit edge polarity and the timestamp referred to the beginning of the readout time window.

- ADC charge with MAROC ADC values and the channel identification number.

2.4 Software Resources

As any in board resources should be made available to the user in a organized and friendly way, the a software library has been developed in parallel to the firmware. In this section the software for the stand-alone setup will be described. Some of this tool could be ported directly in the RICH software suite, others like the configuration database and the logbooking must be changed because of the larger environment of CLAS12.

Any readout action foresees several steps: front-end configuration, start and stop of the data-taking, raw data storage on disk, log-booking, data parsing, analysis, diagnostics and plotting. The current software architecture is object oriented. A C language set of low level instructions is wrapped into custom C++ objects for an easier maintenance, upgrade and porting. The data reconstruction and analysis is performed with the help of ROOT library. Operations take place from a shell command line or by automatize small scripts. At that level any external device (e.g. laser, room temperature) can be integrated in the data stream.

2.4.1 Configuration

Before performing any operation with the front-end, the MAROC chips have to be configured. The FPGA unit takes care of this operation receiving data from the PC and translating them on the MAROC registers using dedicated lines on the board to board connector.

In each front-end board, the MAROC slow control register are daisy chained. This solution brings advantages that go beyond the simple configuration:

1. A random initialized configuration can be used to check the presence of the front-end board and determine, by the depth of the daisy chain, which board variant is connected to the controller unit. This operation is called automatic detection or discover. It iterates the configuration process and compares written and read data, avoiding the need of hard coding the board type information, .

2. A configuration read back can be used during the short breaks of the physics run to check possible alterations of the MAROC static configuration registers due to the passage of particles, contributing in such a way to the data quality monitor. In case any alteration is encountered, the corrected bit value can be restored and the repair action can be logged into the database.

To configure the entire unit the following procedure has been adopted.

- First the front end card variant is identified by sending random bit sequences to the shift register of each MAROC and reading them back; in case of a broken card or a not connected card the read bit are different from the written ones.

- Once established that a card is present and working, the configuration bytes are sent.

- Trigger logic is then defined together with the proper synchronization of the measurements. The event builder latency is regulated in order to capture the hit in an adjustable window of time, before the trigger is issued. The same have to be done with the ADC single cell sampling time which could be tuned to catch the pulse height amplitude at it maximum in order to have the best dynamic range for the charge measurement.

- Event and time preset criteria for the data acquisition to stop as well as identification data are provided for a complete logbooking and to avoid overwriting (optional).

An example of the configuration file is given in appendix.

Log-booking

Many control parameters have to be set and recorded to ensure the correct functioning , obtain the expected results from the readout and optimize the performance. The system parameters are managed using a local database and a C++ interface library called LIBCONFIG. The latter allows the creation of a default configuration file (.cfg) and an easy utility to export the parameters values in plain human readable text file, saving a lot of coding time and allowing for automatic log-booking at the end of the run.

Before saving the configuration file to disk (.log), other run-time information can be added to the database. Examples are the number of events and duration of the run for offline efficiency and rate calculations. Other parameters, e.g. the individual channel gain, or the binary output polarity, can be used by the analysis program to interpret the data and generate for example a coherent title in the plots or used in multiple run analysis like in the case of a gain scan study. Also the sequence and logic of the required actions can be controlled by the configuration file, e.g. the kind of analysis to be performed or the kind of plot to be generated can be selected without the need of recompiling.

An important functionality inserted in the software tool is the possibility of inline substitution of the default value of any parameter at run time. This gives a lot of flexibility to the program, allows automation of the operation and integration with independent devices (by dedicated shell .sh scripts). In particular it is possible to scan all the registers on the boards allowing sophisticated analysis as will be presented in next chapter.

2.4.2 Data Acquisition

Slow Control

This is the simplest readout case because it does not require a trigger signal. Data can be read at any time, written on local registers of the FPGA and transferred to the acquisition node. RICH slow control includes temperature, bias voltages and configuration errors conveniently measured with FPGA embedded resources. In addition, each channel is provided with a counter. Scalers have to be reset, started and latched using dedicated instructions. This information can be used to assess the data quality and monitor the status of hardware and prevent any sub-optimal working condition or damage.

Event

In the Event Mode the TDC information and optionally the ADC can used for the triggered event description. This mode requires the configuration of several elements in the system. The pre-amplifier gain for each channel, and the fast and slow channel shaper response can be tuned to the input signals. A specific discriminating threshold can be defined in each chip to allow the digitization of the fast channels. ADC data can be added or not to the streamed data using an enable flag on a dedicated FPGA register.

If events are built using an external trigger signal, asynchronous with the time stamp clock (250MHz), the measurements are affected by an intrinsic uncertainty equals to a clock period or of 8 ns. When using the the on board pulser (i.e. internal trigger mode), the on board clock is used both to drive the injection and to build events so the timestamp has full 1 ns resolution. The frequency, duty cycle and number of repetitions of the PULSER can be defined at run time. This signal can be used also for triggering the event builder, so that ADC and TDC data can be extracted for each injected pulse. Another use of the internal trigger is to drive external units such as laser and pulse generators. This expedient allows to achieve a timing precision of 1 ns even when using external modules.

Data Analysis

The first step is data parsing and storage into root trees. The tree structure allows a compact and ordered data organization and provides a C++ interface for convenient data inspection, efficient data selection and a powerful graphical interface. The following phase foresees the loop on the events to access ADC and TDC individual channel data, and the TDC hit reconstruction from the leading and trailing edge information. The last step is data selection and histogramming to study the distributions, correlations and statistical significant features in the data.

2.5 Example of operations

In this section a series of procedures are summarized and explained. Example of acquisition modes both for running and for testing are presented as example cases. This option has been preferred to a sequential presentation of the firmware registers and commands.

The electronic inputs can be fed using a light sensor or an external pulse generator. Both signals enter the ADAPTER and reach the input pins of the front-end. Alternatively, the on board pulse generator can be used to verify and calibrate the electronic response. Several acquisition modes are possible, from the trigger free monitor to the triggered event stream. The acquisition can be triggered in external, internal and self trigger modes allowing complete studies of the detector response and sensors phenomenology.

Slow Control monitor

This acquisition mode allows to check and monitor the status of the detector. It is a trigger free readout mode and can be operated during any few second break in the data-taking or as a standard alone system for electronic performance characterization. Temperature data are feed back to the air conditioning system and to the logbooking. This monitor has been used during the stress tests (radiation damage, time stability, ...) and will be used to assess the detector status during the physics rus of the experiment.

Standard CLAS12

RICH operation mode is basically a time correlated reconstruction of the optical flux impinging on its photosensitive surface. The system goal is to stream hit patterns at every trigger distributed by the experiment on the fiber link with 1 ns precision. Only the TDC information will be readout to cope with the trigger latency of 8 μs and be almost dead-time free.

Dark Monitor

In the real condition light sensors produces current pulses from the photons generated by the experiment, or from background excitation. The background has two contributions. The first is due to thermal excitation of the electrons in the photo-cathode and produces single photo-electron signal. The second is produced by by the passage of high energy cosmic particles and can create signal of arbitrary multiplicity and amplitude in the electronics.

This type of data acquisition is performed in auto-trigger mode using the low latency MAROC OR outputs (see MAROC configuration) or an FPGA logic OR, generated considering the entire tile. In the latter case, a 192 bit mask allows to select which MAROC discriminated output can participate to the trigger formation. The availability of single or multiple channel triggering allows the investigation of all the phenomenology of the RICH detector. In this event driven data acquisition mode, no limitation exists from the trigger latency so both TDC and ADC information can be extracted. During the RICH life cycle this mode will allow to monitor the performance of the MAPMT in terms of gain and photo-cathode stability, i.e. monitoring the photon-sensor aging.

Internal Test Pulse

The presence of an adjustable amplitude pulse generator on board allows for detailed and systematic electronic calibrations. The linearity of response can be checked periodically and the information used to update the reconstruction algorithms like the time over threshold correction. Time stability and drift can be also checked. The information relevant for the detector calibration will be saved in the database.

External Test Pulse

For testing purposes a pulse generator with an appropriate dynamic and temporal range can be used to emulate the sensor signals in a controlled way. For example fixing the injected charge to study the transfer function of the preamplifier or creating a burst of pulses for efficiency estimations. The external pulse generator plays an important role during the development and characterization because it offer the chance of full signal path debug. For example it can be conveniently used for a cross-talk estimation between adjacent electronic channel. It provide an essential reference for absolute charge calibration.

Pedestal

The mean value and fluctuations of the baselines can be studied in the absence of light signals by using a random trigger for the analog lines (ADC) and a threshold scan scalers acquisition for the binary lines (TDC).

Laser Test Bench

This mode is used for the full chain characterization of tiles before the detector installation in the experimental hall. Based on the stability of the picosecond laser pulse, it allows a measurement of the absolute detection efficiency, to verify the discharge property and equalize the response of each channel.

Conclusion

Custom RICH readout electronics has been introduced together with the elements necessary for the integration of the RICH module in CLAS12. The

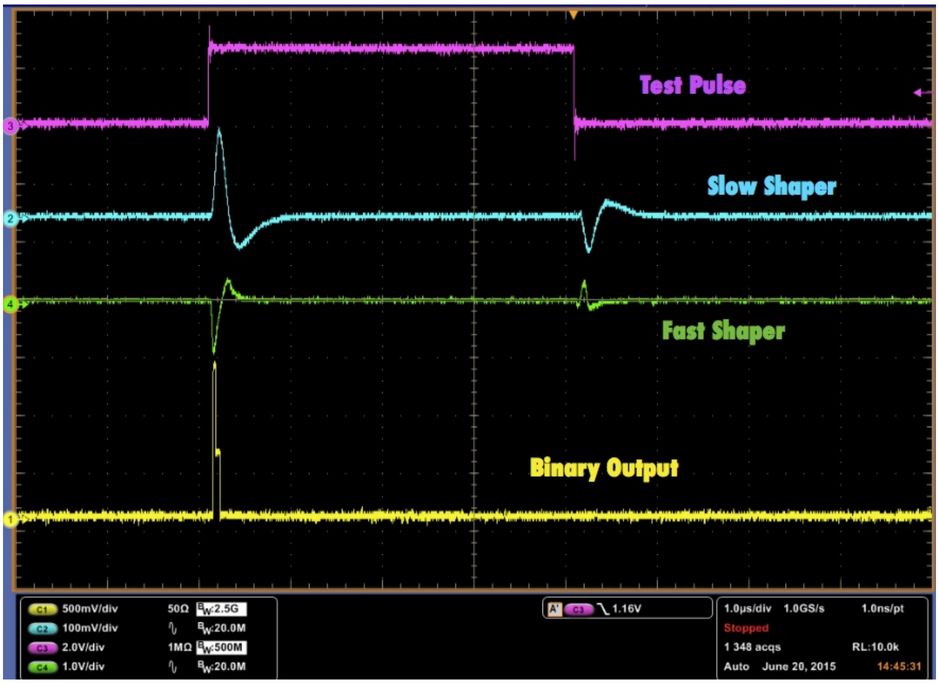

Figure 2.7: Signal processing debug at the oscilloscope

main operating modes have been presented together with their configuration protocols, firmware and data acquisition resources and analysis tools. With the next chapter the focus will be on test bench protocols for acceptance, characterization and calibration of the electronic tile assemblies. Few picture of both variants are presented in the next pages.

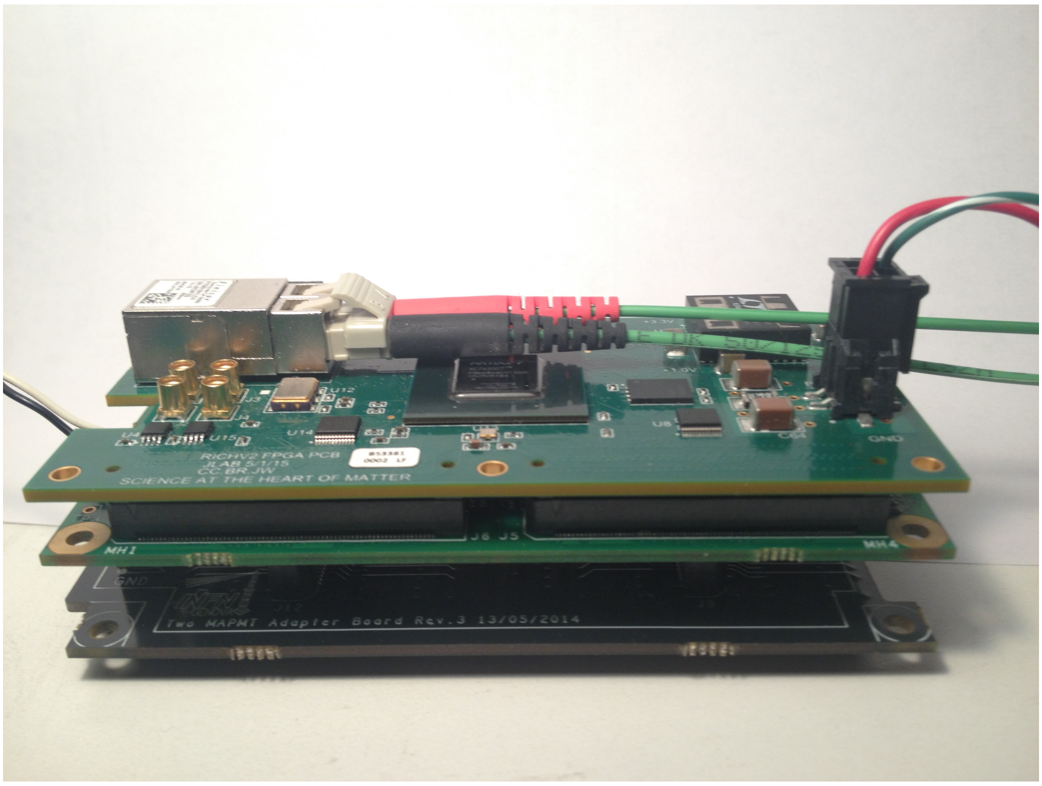

Figure 2.8: 2MAROC tile

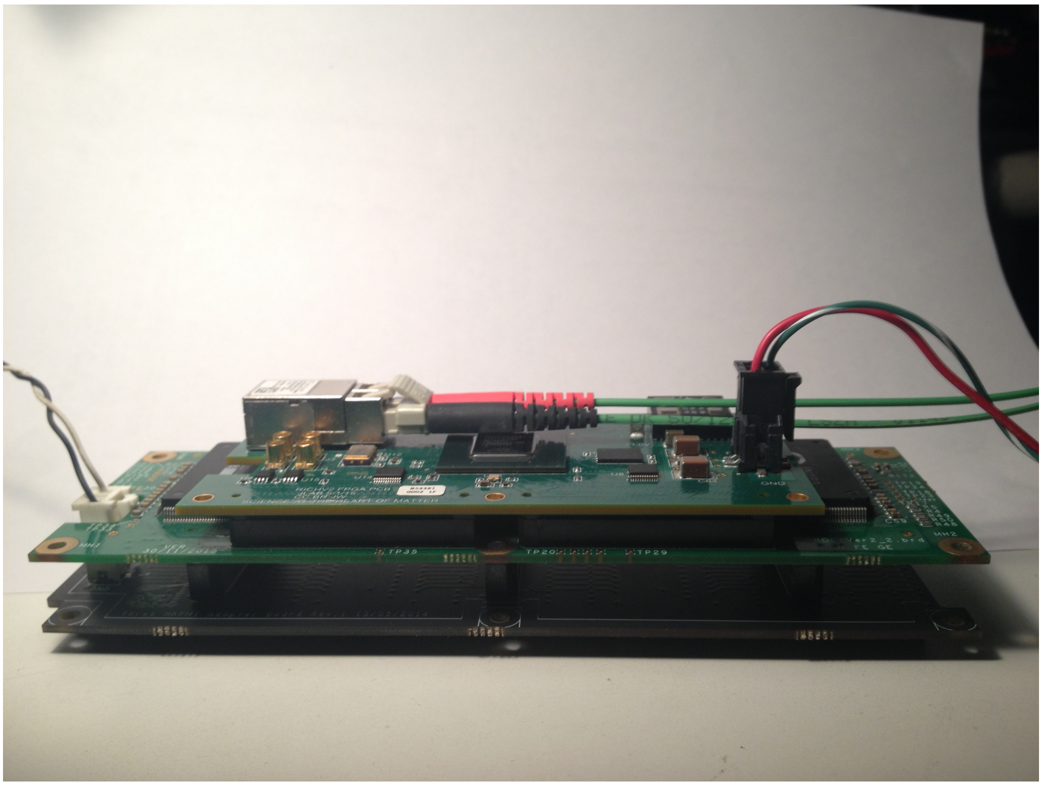

Figure 2.9: 3 MAROC tile

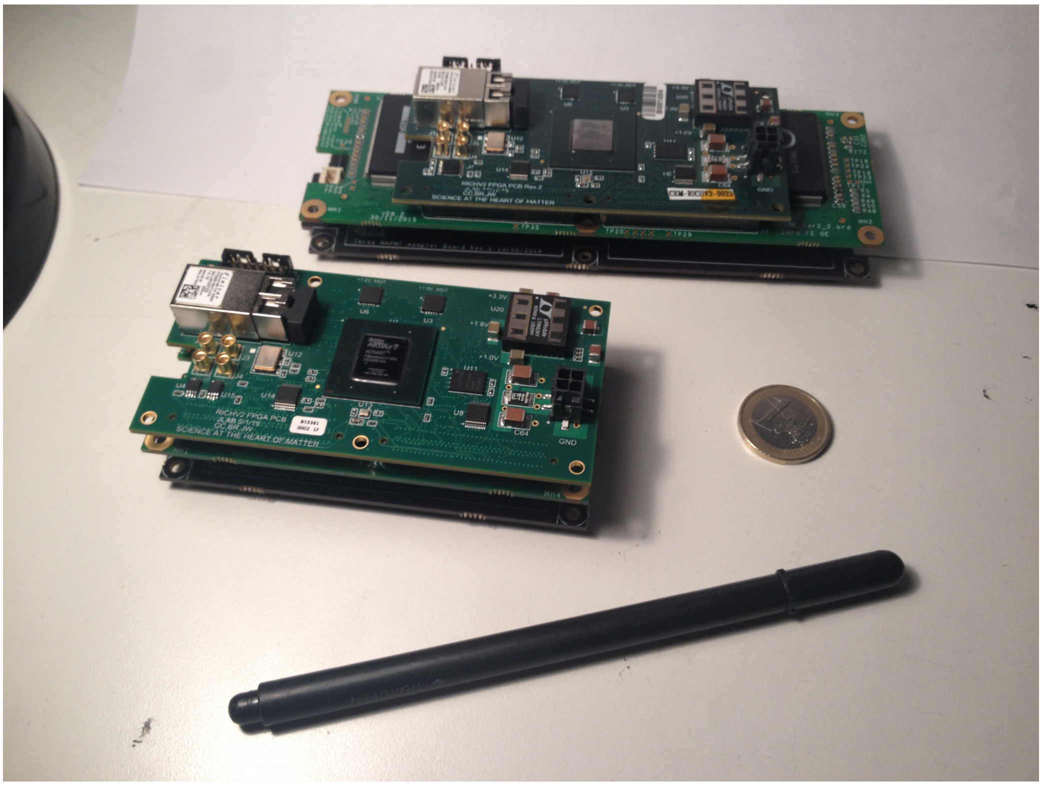

Figure 2.10: Assemblies view

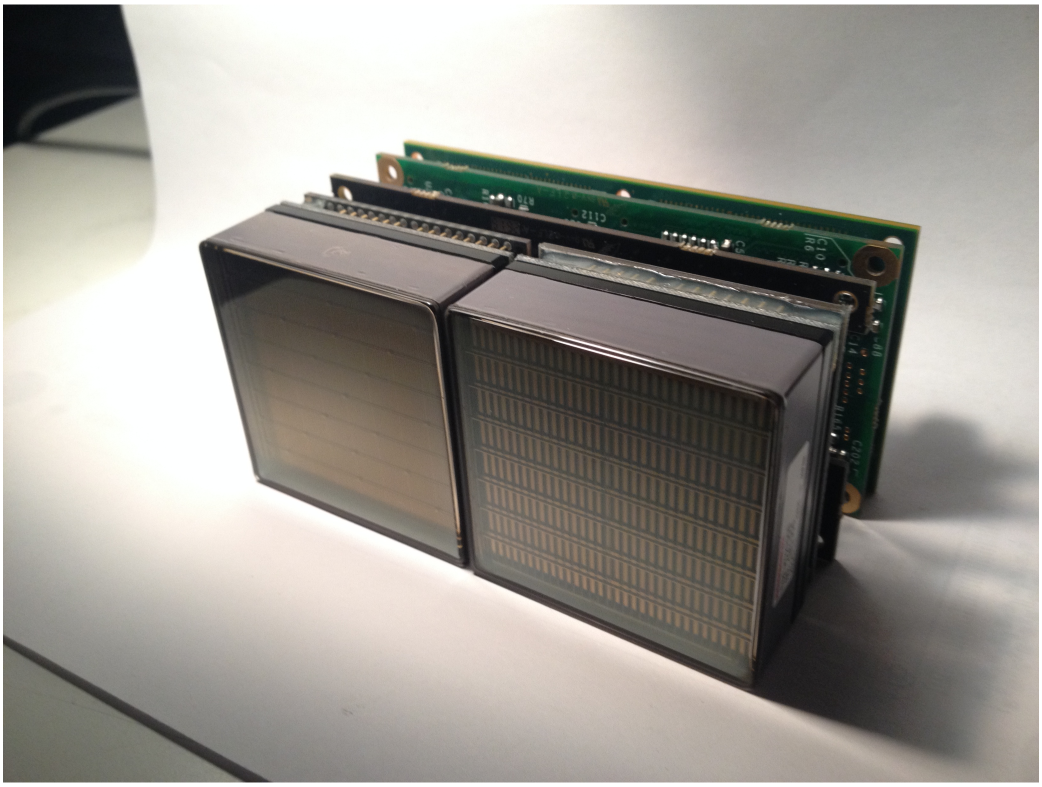

Figure 2.11: Full Tile Assembled with the two tpes of MAPMT, H8500 (left) and H12700 (right)

Chapter 3

Performance

Single photon imaging requires a read out system with negligible response fluctuations to do not deteriorate the intrinsic uncertainty associated with the detection of single quanta of radiation. After having presented the electronics design the focus turns now on the performance characterization. A precise knowledge of the system is in facts essential to optimize the signal processing with am appropriate choice of the front end parameters, compensate the non uniformity on the individual channel basis and correct offline the data depending on the signal intensity.

Tests and protocols presented in this chapter have been developed for the RICH application in the safe environment of a laboratory where realistic but controlled conditions have been reproduced using adequate pulse generators. In particular a bench unit has been adopted in combination with a single channel injector to provide a stable reference for calibration and explore the limits of the response at single photon equivalent excitation level. The on board adjustable pulser have been studied in parallel to develop systematic procedures for *in-situ* channel monitoring independently from the light sensors.

The chapter presents first this basic validation tests and the protocols to produce an effective channel equalization by means of the charge measurements available on the front end chip (MAROC embedded ADC) Then, with increasing complexity, the discrimination sensitivity as a function of the threshold is presented with results that demonstrate a clean single photoelectron (SPE) capability down to few tens of *femtoCoulomb* (fC). In this region special attention has been given to crosstalk that can be an issue in the discriminator performance if not adequately treated. The last argument presented is a timing correction that allow to effectively suppress the spurious hits without loosing counting efficiency. It exploit the time over threshold information to improves significantly the time precision in the charge range spanned by MAPMTs.

3.1 Preliminary validation

Before using a MAROC card as front end element, some of its basic feature have to be validated by means of electrical checks. The correct current absorption as well as voltage bias of all the chips mounted on the printed circuits board and all the configurable voltage levels can be validate separately from the data readout by direct measurements in DC mode. The results can be compared with the expectation by the data acquisition program in order to accept the board or rejecting it and later understand which part of the assembly is broken or badly mounted. Such kind of automation tests are essential for the validation of the mass production (150 cards) and have been manually operated on the first prototypes. A special validation board was designed during the summer of 2016, produced in two samples to test both versions of the MAROC cards, is presented here. It offers the chance to study the stability and temperature dependence of the on board DC levels, providing an independent data set on the RICH front end electronics.

3.1.1 Acceptance

In preparation of the first mass production[1] a DC voltage test board has been designed and implemented at INFN-Ferrara for quick acceptance operations. This passage is important for three reasons: the production quality can be estimated by measuring the frequency of bad mounting and infant failure of the parts; the safe compatibility of the MAROC boards with the rest of the RICH electronics can be assessed verifying the absence of abnormal current absorption; it is a chance to collect an independent data set on the voltage levels generated on boards including pedestals and threshold characteristics.

The board depicted in figure 3.1 has been therefore designed to probe not only the basic bias, but also to access the many test points that were included in the design for debugging purposes. It consists in a pattern of needles connected to a microcontroller with a builtin 10 bit ADC for data acquisition. The needles position is derived from the mechanical drawings of the MAROC boards in a way that allow to probe the test points when the two board are aligned. In fact it replaces the ADAPTER in the RICH assembly stack leaving unaltered the possibility to use the FPGA to program the chips. The microcontroller configuration data are held in a small non

[1] In the second part of February 2017 a gran total of 25k channels will be produced for the first RICH module of CLAS12 using 400 MAROCs on 150 boards

Name	Value	Unit
Absorption (128 channels)	110	mA
Absorption (132 channels)	165	mA
VDDA	3512	mV
VDDD	3280	mV
VHSTl High	1208	mV
VHSTL Low	648	mV
CTEST DAC	1244	mV

Table 3.1: Voltage regulator test results for the two pre-production boards

volatile memory and basically describe the ADC operations using a USB communication protocol with a standard PC. The power can be supplied from the USB port directly or by an independent module using a jumper.

At the moment of writing only two production-quality boards have been tested (320 channels, 5 MAROCs, 1.25% of the gran total production).The most elementary information collected is reported in table 3.1. It comprises the regulated voltages for the MAROCs, the bias of the on board injector's DAC (an *AD5620* part) and the total absorbed currents. Values are expected to vary in a 5% range from board to board.

After having assessed the correct voltage bias, the validated MAROC boards can be configured and their basic programmable feature tested. A RICH-FPGA board is thus plugged and connected to the PC using the optical fiber link. A data acquisition shell script alternates configuration operations and slow control FPGA monitors, described in the RICH software library, with ADC measurements on individual needles. Data are timestamped using Unix time and stored in plain text format for each tested tile. As a further independent monitoring element, a temperature and humidity sensor, can be added to the setup in order to have the air condition in proximity of the boards stack recorded with the same time stamp. Three registers are scanned and the corresponding voltage level measured, they are:

1. the 12 bits CTEST DAC i.e. the part that is used to modulate the charge injection in the MAROC's CTEST pin. One single chip serves all the ASICs of the board.

2. the 10 bit MAROC DAC. This is the portion of the MAROC slow control dedicated to adjust the signal discrimination level. The resulting threshold is common to the 64 channels. Two operating modes are available one for complete span and the other dedicated for optimization in the low charge region (called coarse and fine).

Name	Average	Unit	Dispersion[%]
Pedestal ADC	1041	mV	1.05
Pedestal TDC	1935	mV	0.62
Fine threshold intercept	2326	mV	0.13
Coarse threshold intercept	2336	mV	0.13
CTEST intercept	5	mV	25
Coarse threshold slope	-2.20	mV/DAC	1.36
Fine threshold slope	-1.12	mV/DAC	3.6
CTEST slope	604	mV/DAC	0.77

Table 3.2: Mean values and dispersion of the MAROC boards quality estimators obtained with DC voltage test board and simple fit analysis. Results are narrow distributed except for the CTEST intercept due to the limited resolution of the ADC adopted (4mV)

3. the 64 bit MAROC probe register, used to access the individual channel shaper output i.e. the ADC and TDC baseline levels.

Examples of the measurements can be found in figures 3.2, 3.3 and 3.4. The microcontroller ADC resolution (10 bits over a range of about 4 Volts) is adequate for characterizing the DAC slope and the regulated voltages, but results insufficient to resolve the little spread among the pedestal levels within a chip and to determine the CTEST intercept which have to be determined by other means. Pedestals and DAC voltages are fitted with a line whose parameters, slope and intercept, are used as characteristic estimators of the chips. During the test only few points of the DAC register are acquired for contain the test duration within one minute. The average results are presented in table 3.2 for the pre-production boards.

3.1.2 Stability and temperature

Using the complete setup described above, with the temperature and humidity sensor positioned in the tile cutoff, two test have been performed to study the temperature dependence of the parameters.

Test 1, fixed temperatures

The first test has been conducted in a temperature controlled room at 25°C with and without a cooling fan (visible in figure 3.1).

As shown in table 3.3 the presence of the fan dispersed all the irradiated heat produced by the electronics while its absence produces a higher thermal

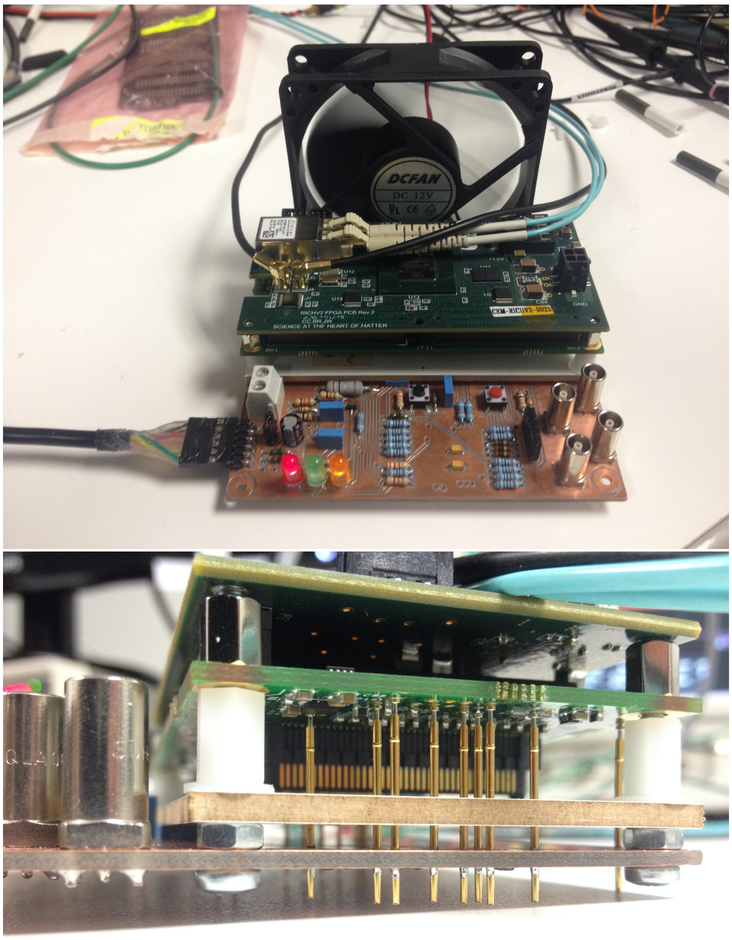

Figure 3.1: DC voltage test board setup.the MAROC board under test is positioned in the middle of the stack between the large PCB of the DC voltage board and the FPGA. The fan is used to disperse the heat produced creating a stable condition of about 25°C in the air surrounding the MAROCs. On the top picture a detail view on the needles.

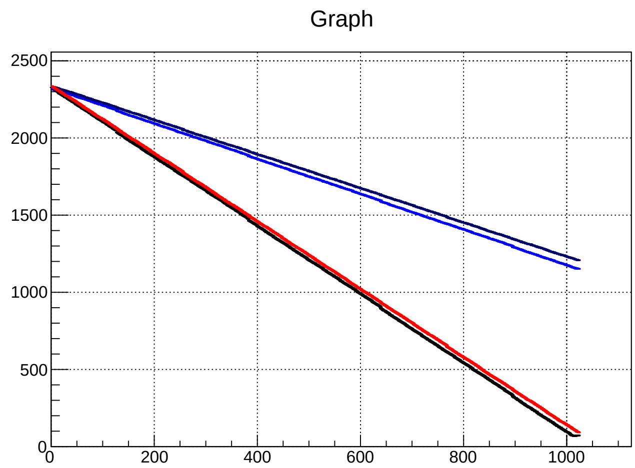

Figure 3.2: Characterization of MAROC's 12 bit DAC, common to the 64 channels ans used to generate the voltage level for signal discriminating. The plot presents the output voltage in millivolts as a function of the DAC word for two chips. The different DAC operating modes have different colors, in blue the FINE mode, in red the COARSE full range mode.

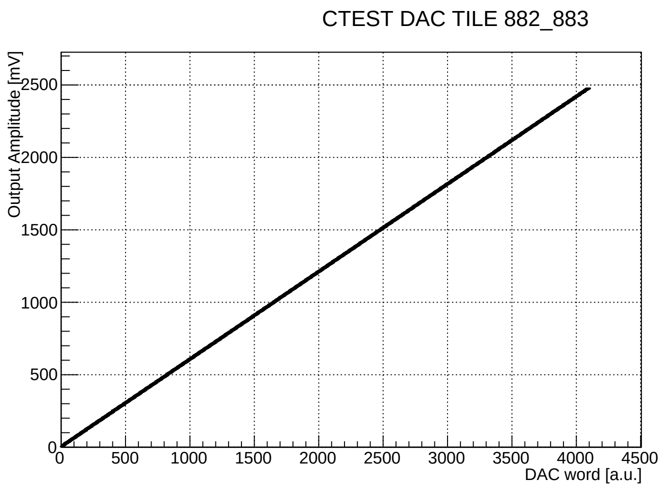

Figure 3.3: Characterization of CTEST DAC. Giving that the input CTEST capacitance of a single readout channel is 2 pF, this DAC allows to span the charges from 0 to 5pC with a precision at the level of fC and an offset of about 6 fC.

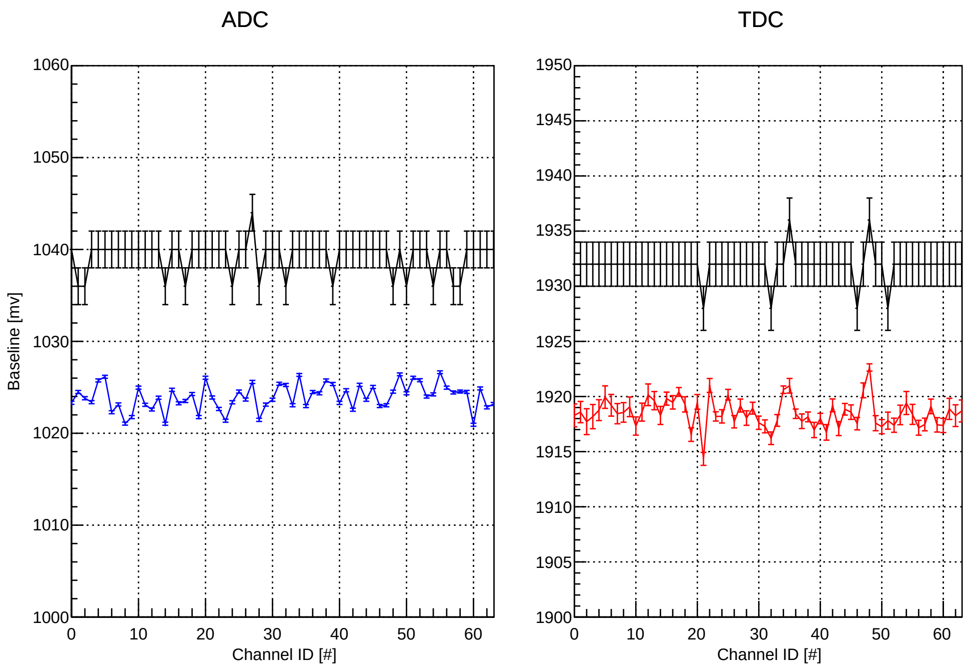

Figure 3.4: Baseline levels vs channels for chip 882. Test board measurements (in black) can be compared with TDC (red) and ADC (blue) voltage calibrated data. The latter, explained in section 3.2, have been slightly staggered for clarity.

	FPGA °C	Air °C
with fan	45	25
without fan	65	35

Table 3.3: Fixed temperature test conditions. The air around the board stack is measured with a temperature and humidity sensor positioned in the tile cut off in correspondence of the MAROC board

Name	T=25°C	T=34°C	Variation (%)
Coarse intercept [mV]	2341 (1)	2338 (1)	1.3×10^{-3}
Fine intercept [mV]	2340 (1)	2337 (1)	1.3×10^{-3}
Coarse slope [mV/DAC]	-2.223 (0.004)	-2.241 (0.004)	8.1×10^{-3}
Fine slope [mV/DAC]	-1.151 (0.002)	-1.143 (0.002)	7.3×10^{-3}

Table 3.4: Threshold Stability for MAROC 882 for the two temperature condition reproduced in test 1.

,

field around the boards. More than a hundred iterations have been performed in the two condition obtaining precious indications about the reproducibility of the measurements and the order of magnitude of the temperature induced variations.

MAROC baseline behavior, for chip 882, is visible in figure 3.5 where hotter temperature data are depicted in red while cooler are in blue. When the temperature is fixed the values are stable well reproducible with an error of about 1mV. By comparing the mean values at of the distributions the MAROC ADC pedestal results less sensitive to the temperature with a gradient of -0.1 mV/°C that for the TDC pedestal is -0.8 mV/°C.

Similar plot have been obtained for the other monitored parameters giving a general and wide on the MAROC board stability. If the temperature variation are limited to few celsius degree the global performance is very reproducible. In absolute the most stable chip is the CTEST DAC for which the temperature fluctuation are smaller than the systematic error as presented in the next paragraph. Because of its importance for the RICH sensitivity, the MAROC DAC parameters are reported in table 3.4. Temperature drift of the slope parameter could propagate, if not corrected, in the calibration data because high value of the DAC register are used to estimate the pulse height of the binary output.

Test 2 continuously varying temperatures

Since the air temperature condition of the tiles in CLAS12 is expected to be around 45°C with a maximum FPGA temperature of 80°C, a larger temperature span test has been conducted by wrapping the tile with a blanked. The heat generated by the electronics was used to provoke a slow increase in the air temperature surrounding the tile by progressively closing any aperture.

Because the FPGA operating condition cannot exceed 125°C, the warming was interrupted at an FPGA temperature of 100°C, removing the blanket

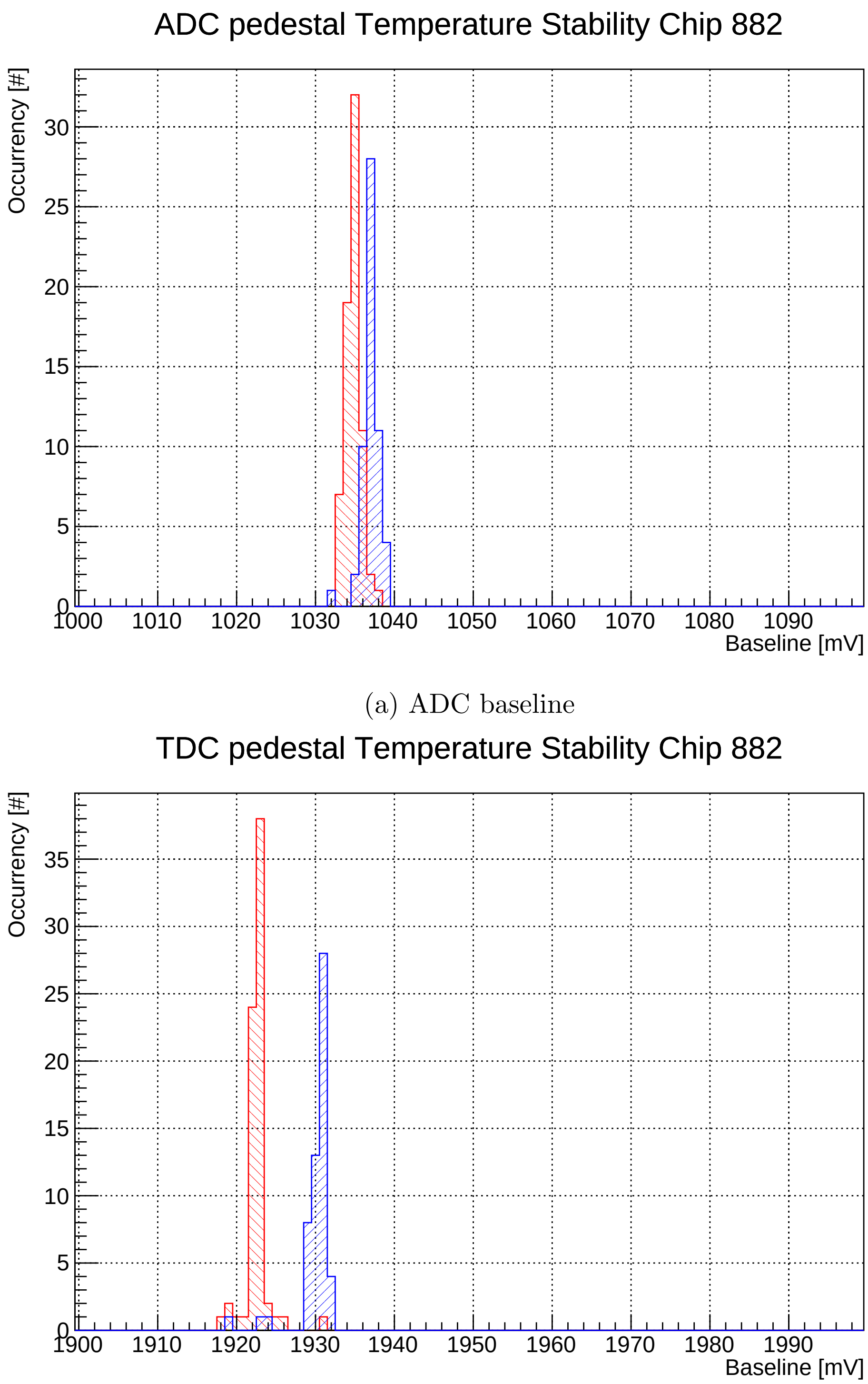

(a) ADC baseline

(b) TDC baseline

Figure 3.5: MAROC baseline stability at two different air temperature 35° (red) and 25° (blue).

and letting the boards thermalize again with the room temperature. FPGA and air temperature have been continuously monitored. Globally for an FPGA excursion thermal excursion from 65°C to 100°C and back, the air temperature varied (linearly) in the interval from 35°C to 69°C and the humidity moved from 30% to 7%.

Examples of the obtained temperature dependence are shown in figure 3.6 where two significant parameters, the MAROC fine threshold slope and the CTEST DAC slope are plotted against the FPGA temperature. Within the spanned range the CTEST DAC slope showed negligible thermal fluctuation compared with the measurements resolution. Its estimated value along all the spanned range is $604 \pm 5\mu$V/DAC. The MAROCs were still stable, but a little drift has been noticed on all the estimators. Something to be known, but that do not represent an issue for the detector performance.

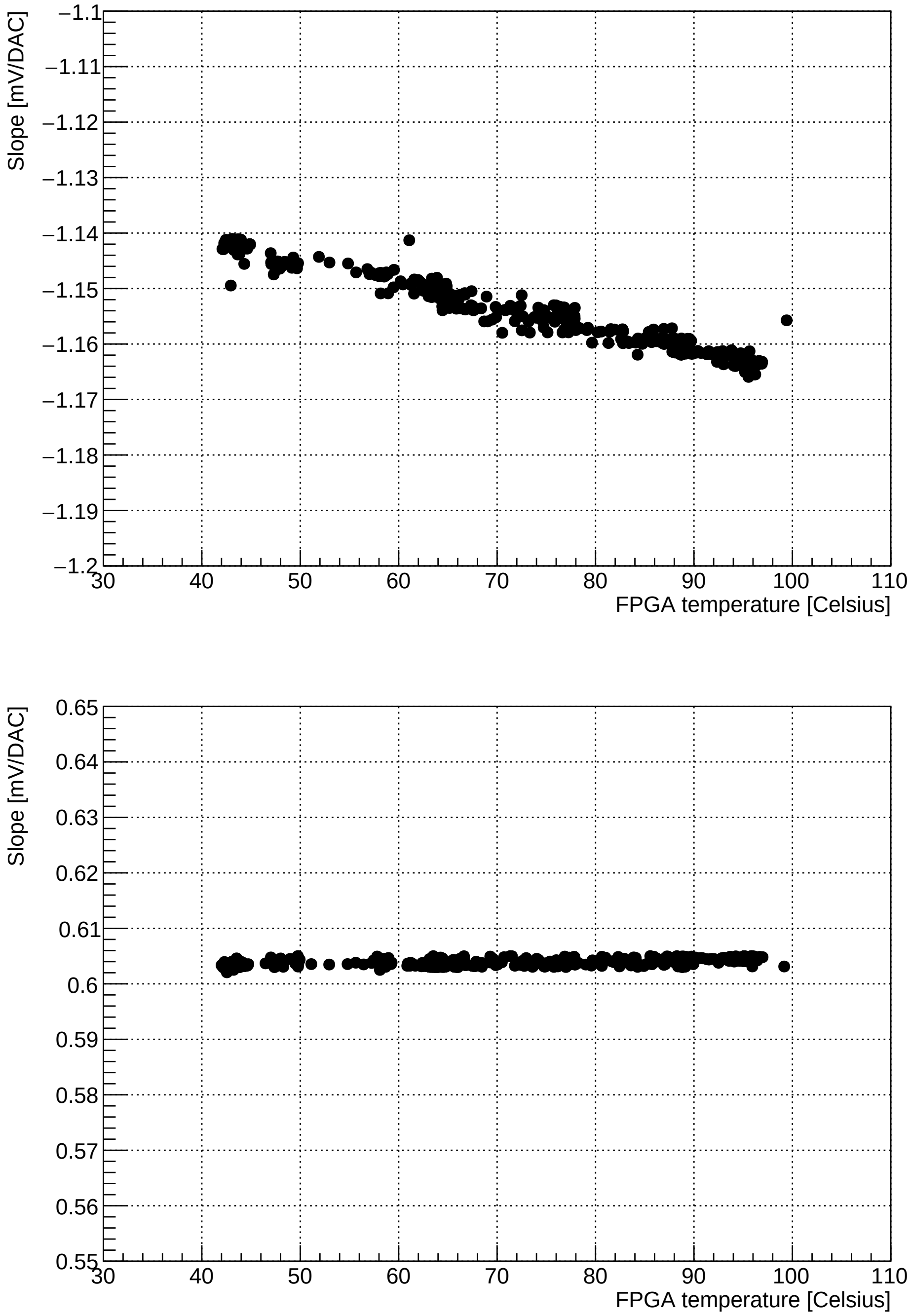

Figure 3.6: Temperature dependence of MAROC discrimination threshold slope (top) and test pulse DAC slope (bottom)

3.2 Pedestal characterization

The pedestal of a readout channel is its response when no signal is injected. It is a simple, but relevant, information that contributes to delineate the global performance of the measurement system. It can be described as a continuous part to which a fluctuation is superimposed. If the first represent just an offset, the second has a deep impact on the quality of measurements and its treatment is one of the most fascinating aspect of the mathematical models of physical systems.

Our objective here is to describe the procedure developed for the MAROC pedestal measurement and to discuss its impact on ADC and TDC. In facts three aspects are interesting in the RICH operation, they are: the inferior limit for a clean single photon detection, the effects introduced by the individual channel input preamplifier and the possible limitation due to the use of a common threshold for the 64 channels of the MAROC. More in general an accurate electronic noise characterization allows to foresee the consequences of the signal response, for superposition principle, and tailor the digitization elements accordingly. As we will be presented in the next paragraphs MAROC pedestals distribution are very narrow with a negligible contribution to both amplitude and timing performances.

3.2.1 Binary output (TDC)

TDC pedestal is the DC voltage level of the fast shaper output and can be estimated with repeated data acquisitions at different comparator thresholds, here referred as *threshold scans*. The DAC register has 2.2 mV LSB.

An example of a reconstructed pedestal for one single channel is presented in figure 3.7a where the number of logical pulses are plotted against the threshold value in DAC unit. The probability to have spurious hit is negligible everywhere except a narrow region where a gaussian-like distribution appears. Measurements are done in scalers acquisition mode (i.e. without building the events) to do not saturate the readout capability. Counters are reset and latched after 100ms in order to extract the information in a small amount of time and reasonable small statistical error. The mean value of the obtained histogram corresponds to the baseline DC level while its RMS is taken as a measure of its fluctuation. No model is used because this estimator already provide good quality indication: in a register of 10 bit the pedestal the noise level is about few DAC units. More over some channels tends to have a tiny periodical oscillation superimposed to the baseline determining a flattening in the distribution. The minimum working threshold is then determined for each channel as the DAC value positioned five times RMS above

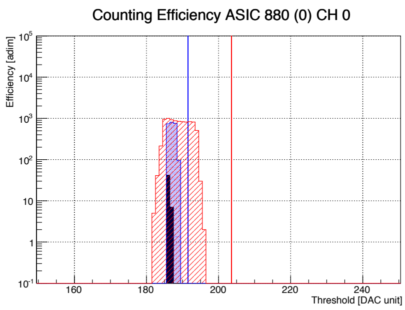

(a) Pedestal counts distribution for a single channel as a function of the threshold for three different gains

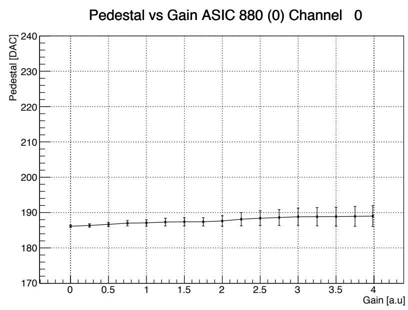

(b) Single channel pedestal as a function of the gain. Error bars are the RMS of the distribution.

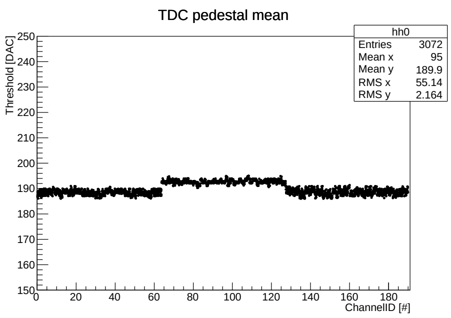

(c) Mean pedestal value vs channel ID for an entire tile (3 MAROC,i.e. 192 channels). Data at different gain superimposed.

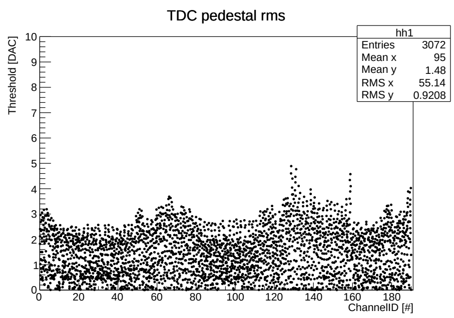

(d) As in (c). Maximum noise does not exceed 5 units. The basin shape, i.e. the correlation with the channel ID, is due to different routing length on the PCB.

Figure 3.7: TDC pedestal single channel and tile uniformity. The electronic noise is at the level of of few mv even at the highest input preamplifier gain.

the pedestal (vertical lines in figure 3.7a). The threshold scan is repeated at different gain from a minimum of zero and a maximum of 4. A typical curve is shown in figure 3.7b where the points of the graph indicates th mean value of the pedestal and the vertical bars are its RMS. The distribution results very narrow even at maximum gain with a small drift of few DAC channels probably due to the non perfect gaussian shape of the baseline.

Since scalers (as TDC) have a parallel readout, with a single threshold scan all the channels can be characterized. This information is presented in figure 3.7c and 3.7d by merging all the data obtained at different gains as a function of the channel id. As the noise depends on the capacitance at the inputs level, few channels shows higher fluctuation because of a longer path on the board, anyway never exceeding 10 mV. The “basin” behavior can be explained in terms of printed circuit board layout: the path of first and last channels of each chip are longer in comparison to the lenght of the path used to route the central channels. This lake of equalization in the path length was unavoidable since the small space available on board and is due to a orthogonal orientation of the input connector with respect to the MAROC input pins line.

Since fluctuation depends on the capacitance the pedestal estimation must be repeated when the MAPMT are plugged. Fortunately, the developed procedure is fast (few seconds for each gain setting), so the TDC pedestal estimation can be part of any preliminary operation with the hardware. It is important to notice that the pedestal mean value within a chip has a very small spread, at the same level of the single channel, therefore the use of a common signal discrimination threshold does not represent a limit for the performance. In addition the drift observed for different preamplification gain is negligible therefore the input equalization can be done with complete freedom.

3.2.2 Analog output (ADC)

ADC pedestal is the slow shaper output DC level and corresponds to the baseline of the charge measurement. In contrast with the signal discrimination operation, the ADC is an instantaneous measurement of the amplitude. As a consequence, excluding the case of self trigger measurements, no threshold is used and no overload on the readout system can be generated. The converter is embedded in the MAROC and is a Wilkinson converter so it’s speed is determined only by the ramp slope and by the amplitude to be converted.

The ADC pedestal of each single channel is estimated by triggering repetitively the event builder and histogramming the values obtained for each channel. Since the dead time is not critical a high repetition frequency can be used together with the maximum resolution of 12bits.

At fixed gain a typical plot is showed in figure 3.8a, while a fine gain scan plot is presented in the adjacent figure 3.8b, both refer to a single channel. As found for the binary lines, the pedestal of the charge measurements is narrow and almost independent from the preamplificator gain.

Chip uniformity is visible in figures 3.8c and 3.8d for a 3 MAROC tile. A reduced spread among channel is less critical than in the TDC case since the pedestal information is used for offline software alignment. However no deviations larger then 1% have been observed among the chips of the prototype boards. Also baseline fluctuation are very uniform and small. In comparison with figure 3.7d that shows the TDC pedestal fluctuation the ADC ones are more uniform because of the longer time constants and smaller gain, reflecting a deep difference in the two system: one dedicated to pulse height measurements operating in a linear regime over a wide interval of input charge, the other with high gain for abrupt separation.

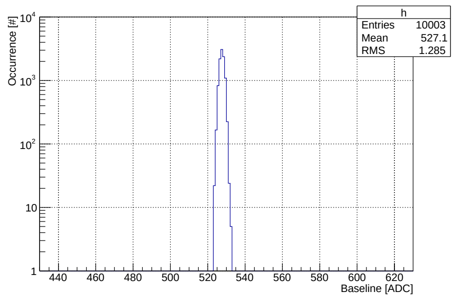

(a) Single Channel pedestal ADC measurement. RMS is about 1.3 ADC units

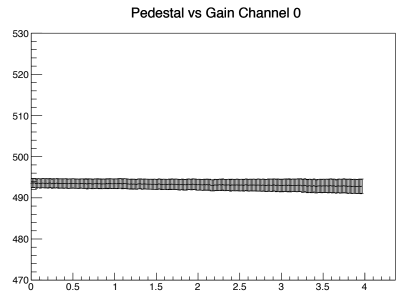

(b) Single Channel pedestal as a function of the gain for a single channel

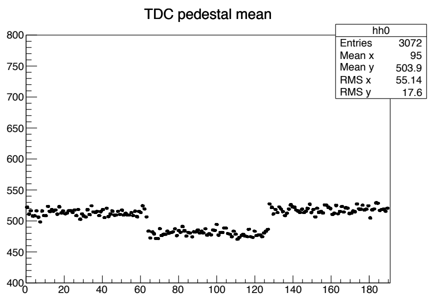

(c) Pedestal Mean as a function of the channel ID of a tile. 16 gain settings are superimposed

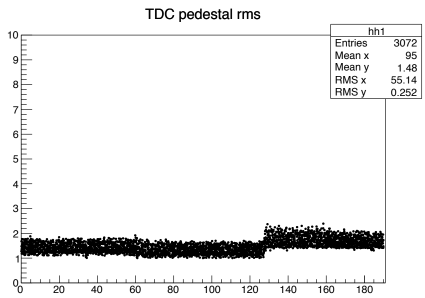

(d) Pedestal RMS as a function of the channel ID of a tile. All the gains superimposed

Figure 3.8: ADC pedestal study. Boards final revision shows extremely small baseline fluctuation even at maximum preamplifier gain. ADC was used in 12 bit modes to have maximum resolution

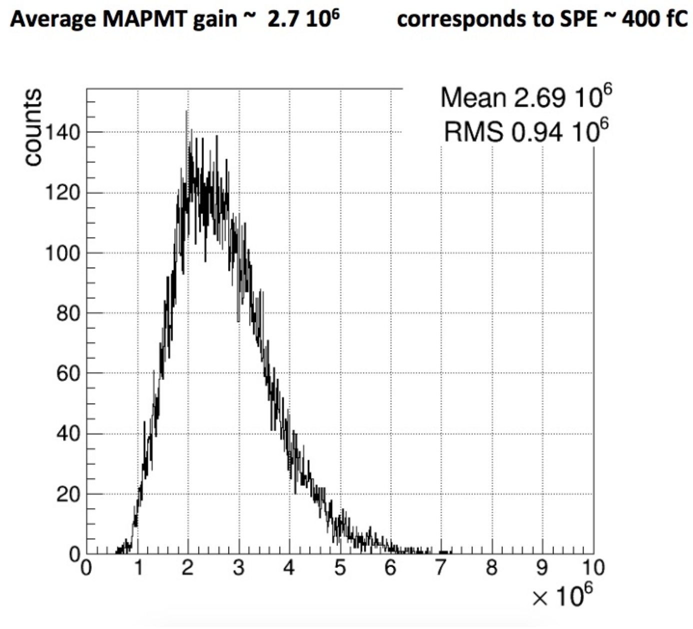

Figure 3.9: Histogram of the amplification gain of the 391 MAPMTs used for the first RICH sector construction. A single photo electron (SPE) produces on average 400 fC pulses

3.3 Charge response

In this section the reader will be guided through the use of ADC and TDC readout system, their configuration, and optimization. The section is organized as a review of all the studies performed during the development phase to validate the tile assembly as readout unit for the MAPMT. The first section is dedicated to the single photo-electron (SPE) signal range and the use of pulse generator as an adequate alternative to the real sensors for the study and the optimization of the signal processing chain. A set of pulse height measurements is used to characterize and tune up the MAROC embedded ADC after having synchronized it with the trigger signal. All the signal processing elements are presented with particular attention to the linearity properties that allow an effective compensation of the pixel gain spread. In particular the excellent sensitivity down to 10 fC is demonstrated. This feature combined with the TDC firmware precision of 1 ns perfectly satisfy two important RICH detector requirements.

3.3.1 Dynamical range

Light sensors can be thought as light controlled current generators positioned at the input of the signal processing chain. About 25k MAPMT pixels compose the detection surface of the RICH with average gains that are presented in figure 3.9. Looking at the distribution a typical (reference value) pixel would produce 2.7×10^6 electrons for each detected photon or equivalently 400 fC.

In practice an intrinsic variability of the charge generated by each pixel is expected at single photoelectron level (SPE) due to fluctuations in the gain mechanism of the amplifying elements. Because the number of carriers increase at each stage the most important contribution to the fluctuation arises from the first stage of amplification where a single electron, emitted by the cathode, is accelerated towards the first dynode and, hitting it, generates a number of secondaries that give the start to the avalanche. Assuming a Poisson model for the secondary emission process and considering a typical[2] first stage gain between 5 and 10 the variance of the single pixel gain can be assumed about 3. This means that when working at SPE level the dynamic range can extend over 3 order of magnitude. Taking 400fC as a reference a conservative estimation gives a typical charge range in the interval from few tens of fC to few pC.

3.3.2 Pulse injection setup

Single photoelectron sensors are refined and delicate devices that require to be used in a completely dark environment and, in the case of MAPMTs, an high voltage source. For practical reason, the adoption of pulse generators with similar signal characteristics is very convenient in the laboratory as it allow the study of the signal processing performance in a controlled and reproducible way. Pulse generators are therefore used to adjust the system parameters and develop the protocols for response optimization. During the preliminary commissioning with the real generators,i.e. the light sensors, all the procedures can be verified in the final electronic configuration (e.g. capacitance, slew rate, jitter).

An external step function generator has been adopted as a reference for the system calibration. The injection circuit is composed by a simple capacitor mounted at the end of a LEMO cable. The injection circuit is completed by a $10\,\mathrm{k}\Omega$ termination resistor and two pins for an effective signal injection into one single channel of the ADAPTER board. The amplitude od the

[2]More details on the first stage secondary emission estimation for the the H8500 and H12700 models used for the RICH construction can be found in [25]

voltage step across the capacitance, adjusted with the generator knob and measured with an oscilloscope, determines the amount of charge contained in the produced current spike. This is a typical scheme for testing the pulse processor chain and thanks to a proper choice of the capacitor, 1 pF in our case, allows to adjust very precisely the charge level. Namely, by definition of capacitance, 1 fC for each mV of step amplitude. The only inconvenient is that, because of the squared wave produced by the generator, two current spikes are generated with opposite polarity. Fortunately the MAROC response to positive charge injection is weak and can be easily identified at the oscilloscope. During the tests the only precaution is therefore to keep well separated in time the dummy from the true pulse by acting on the driving signal duty cycle.

Different models of injector have been and will be used for board testing and validations, included multiple channel versionS, but none of them will be available *in situ* when the detector will be installed. For this reason an adjustable amplitude pulser has been designed *on board* using the same architecture of the one just described. The advantage of it is that any pattern of channels can be tested thanks to a configuration mask in the MAROC slow control register[3]. The disadvantage is that the actual capacitance,$C = 2\ pF$ when a single channel is selected, varies with the number of channels and that a time spread between channel is observed, a still not completely understood[4]. From the name of the input pin of the MAROC, this injector is called CTEST.

Both injectors, external and on board CTEST, are trigger by the FPGA internal pulser for the maximum TDC measurements precision and span can the charge interval from 5fC to 5 pC.

3.3.3 Charge calibration

To calibrate the on board test pulser, CTEST, the following procedure has been adopted, based on the fact that identical stimuli produces identical responses, at least in linear regimes. An external precise pulse generator and the injection circuit described in the previous section 3.3.2 is used as a reference.

1. a CTEST value is configured and a pulse burst is started by the data acquisition program working in *configuration only* mode.

2. The pulser signal is taken from one of the MMCX resources of the

[3]The on board pulser resources is shared by all the MAROCs of a front end card

[4]The MAROC test input was probably designed only for a dead or alive test of the channels, so not particular care has been putted on timing performance

FPGA, delayed by 1μs to avoid pulse response pile up and used to trigger the external injector

3. The fast shaper output (20-25 ns peaking time) of the selected MAROC channel is monitored at the oscilloscope in order to have both responses on the same acquisition window.

4. The amplitude of the external one is adjusted until the pulse height are identical.

5. The amplitude in mV as well as the programmed CTEST DAC values are recorded.

The procedure is repeated for some points in the linear region of the fast shaper response and the calibration parameters are derived from a linear fit as shown in figure 3.10. Since 1 pF capacitance is used for the external injector its slope is unitary and its intercept is null by definition (blue curve). The CTEST show a similar behavior except for a little offset estimated as 5.6 fC. This is due to a few mV output of the CTEST DAC when programmed with the word zero (DAC=0)that can be also measured by probing directly the pin. Apart from this little offset it can be assumed for all practical purposes that the CTEST injector provides 1 fC/DAC resolution when a single channel is enabled.

This is the first mode adopted for calibration. A second method more adequate for systematic studies substitutes the oscilloscope measurement with the MAROC embedded ADC and is done in two passages. First the ADC is calibrated using the external injector. Then in a second moment the CTEST DAC register is scanned until it reproduces the same ADC response. As both methods gives the same results they are considered equivalent. The only important passage is to have available a data set (in mV or ADC units) obtained in response to known reference charges. As presented in the next section the time step for ADC synchronization is 8 ns (from the 250MHz main clock) and in view of a setup dependent injection delay the reconstructed waveform thus the ADC calibration can be slightly different for the two cases, internal and external. This can be compensated by using an analytical model derived from the transfer function of the shaper of by getting a finer tuning step with the addition of a a frequency multiplier firmware module.

Knowing the amount of the injected charge and by repeating the operation for few input charge level, the response of the system can be expressed in physical units both for the pulse height measurement and the discrimination threshold level.

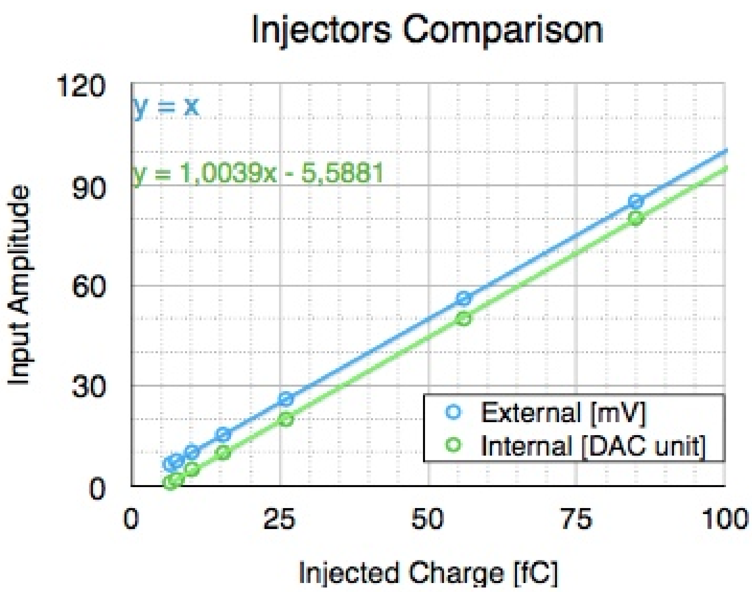

Figure 3.10: Test pulse calibration. CTEST and Anode input shows the same response in the small charge region. The little offset of 5.6 fC is due to few mV output of the DAC when programmed with DAC word = 0

3.3.4 Pulse height measurements

MAROC provides charge measurement thanks to an embedded Wilkinson ADC with a ramp common to the 64 channels. When the all the amplitudes are converted the chip its self assert a strobe line and start the serial data readout by means of a 40MHz clock. The Wilkinson digitization can be configured to be 12, 10 or 8 bit with impact on the speed of conversion which maximum can take 90 μs and in general depends on the highest amplitude to be converted.

This amplitude depends on three analog processing circuits and by the timing of the HOLD signal that freeze the information on an analog memory cell of 2 pF. All the necessary information is represented in figure **??** and is described in the following paragraph. The transfer function of each block can be adjusted using dedicated bit groups in the slow control configuration register of the chip. To help with the tune up a fast *waveform reconstruction* data acquisition mode has been developed. The procedure acquires a significant number of ADC samples in each condition, calculates average and variance of the samples on a individual channel basis and for each distinct HOLD delay value (given in 250MHz clock ticks units). After having considered all the possible hold values (8 bits) scans each single channel data set recording the peak amplitude, the peak time and the zero crossing time to determine the best parameter choice in terms of uniformity, dynamical range and linearity. The three blocks are:

1. *Preamplifier*: An 8 bit adjustable gain current mirror amplifier is present at the beginning of all the readout channels for detector gain spread compensation. The values from 0 to 255 are mapped on the interval 0 to 4. It offers a small input impedance of the order of 50-100 Ohm. Its transfer is linear in a great input charge intervals and the overall linearity limit can be controlled by the coincidence of the zero crossing points. See for an example the bottom pane of figure **??**.

2. *RC Buffer* An RC buffer, configurable at chip level, is devoted to the current-voltage conversion. By default the conversion is purely resistive , $R = 50\,\mathrm{k}\Omega$; various capacitances up to 3.75 pF can be added in parallel to match the with the sensor signal slew rate and extend the linearity of the charge measurement over a wide range of charge (up to 30pC if needed).

3. *Slow Shaper* A slow shaper, configurable at chip level, is available for improving signal to noise ration thanks to a a CR-RC amplifier. The different settings allow to varies the signal to noise ratio at different

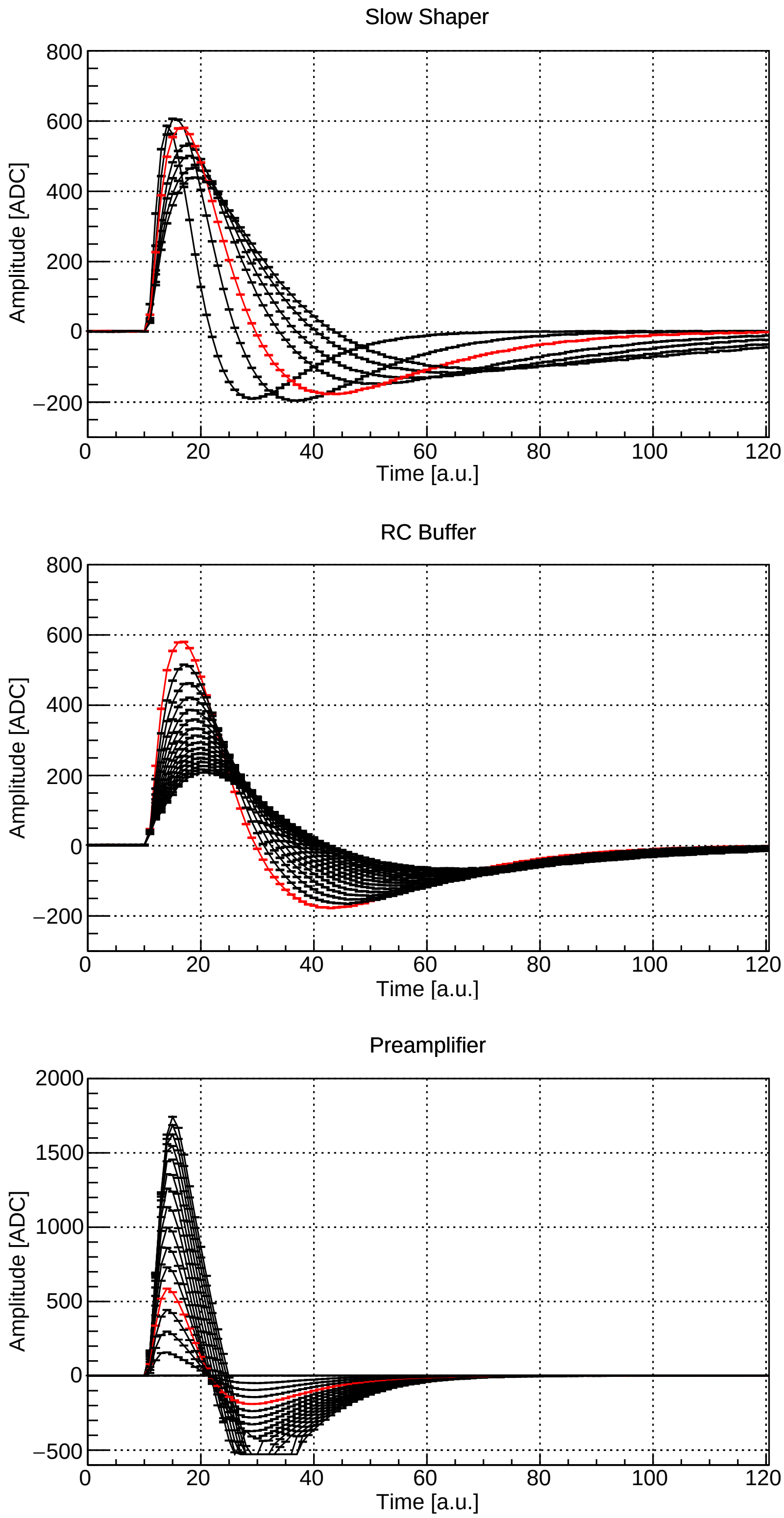

Figure 3.11: Reconstructed waveforms for different shaping parameter of the MAROC slow channel. Injected charge pretty high i.e. 825 fC to highlight the lost of shaper linearity for high preamplifier gain (bottom plot) and the possibility to attenuate using the RC buffer (central plot). In red the adopted choice guarantees an adequate linearity on the ADC data. Time is in clock tick units (8 ns).

rise time settings with measured peaking time varying from 50 to 150 ns;

The preamplifier is in common between the slow and fast channel of MAROC in order to exploit the input equalization, verified with the ADC, to the signal discrimination. More details about these an other shaping settings can be found in appendix B

Even with the slowest peaking time configuration and the poorest resolution, the trigger can not be delayed more than 150 nanoseconds: any greater latency would results in a lost of the signal and a pedestal measurement. For example, the CLAS12 trigger latency is of the order of few microseconds and prevents the sampling of the signal pulses during physics runs. On the contrary, in test conditions like electronic calibration and dark rate monitor, the trigger is available few nanoseconds after the event and useful information can be extracted from the pulse height spectra obtained at a fixed optimized delay.

Another characteristics shown by the figure **??**is the small electronics noise associated with the pulse height measurements, in practice at the level of the quantization error, i.e. 1 ADC only. With such noise free condition, high quality spectra of the light sensor response can be obtained as described in the next chapter.

An ADC calibration can be obtained by recording the pulse height as a function of the input charge. Results are in the range from 0.6 fC/ADC to 2 fC/ADC, depending on the shaping configuration and gain

The standard configuration for operating at single photoelectron level is highlighted in red in figure **??** and allow linear operation up to 2 pC.

3.4 Discrimination and timing

The excellent signal discrimination capability of the system is presented with particular focus the small charge region where the calibration procedure allows to set the working threshold down to few fC. The timing performance of the TDC algorithm implemented in the FPGA is briefly presented satisfying all the specifications. Finally the protocol for the time walk correction is presented.

The MAROC parallel binary outputs are obtained from an high gain fast shaper amplifier (with 20-25 ns peaking time) followed by a discriminator with a programmable threshold. The shaper rise time settings can be configured to best match the input signal to the discriminator dynamic range. The FPGA houses TDC units that process the digital information, assigning

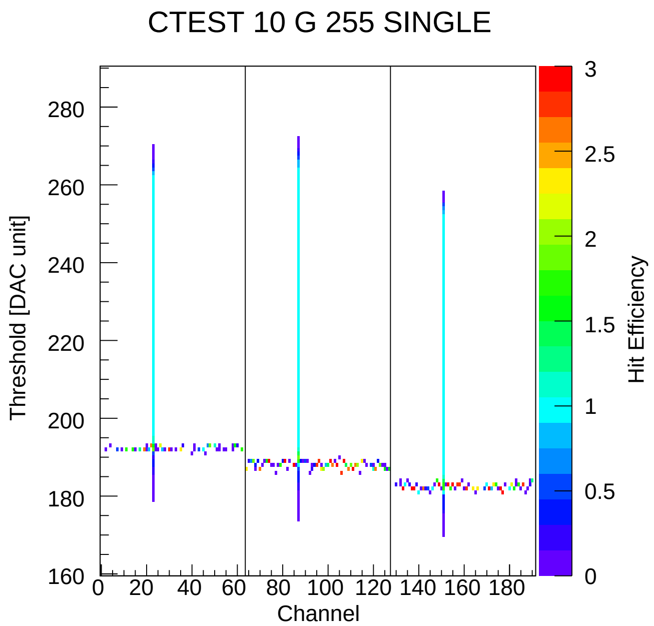

Figure 3.12: Integral pulse height spectra for 3 channels out of 192 with maximum preamplifier gain (factor 4). The step function is provided by the on board pulser (CTEST), charge level is 60f.

a timestamp with 1 ns resolution to the leading and trailing edges of the MAROC discriminator output.

3.4.1 Sensitivity measurements

Charge discrimination offers, as a great advantage compared to the pulse height measurement, a smaller data size. Using this output mode indeed, the state of each photosensitive element is specified by just one bit of information with a natural zero suppression and a boost on the read out speed. For experiments with a large number of readout channels and low occupancy the benefit on rate and dead time can be significant. The binary readout is an effective choice in single photon applications where no other information is needed except the presence or the lack of radiation quanta in a given time window. However once a signal from a single photon detector has been discriminated, some information is lost (like the pulse height), as it is transformed into a logic pulse equal in amplitude to any other logic pulse. Actually, some information about the shape can still be conveniently extracted from the logic pulse as it is contained in its duration, called *time over threshold*.

A MAROC fast channel is composed by three active analog blocks devoted to signal amplification, shaping and discrimination. The first element is in common with the slow channel and its linearity has been demonstrated in section **??**. Here the focus is on the fast shaper and integral discriminator to find the optimum working point in terms of sensitivity and time resolution. Figure **??** shows the measured discrimination voltage level as a function of the 10 bit adjustable threshold for the two available operating modes. The full range can be spanned using the standard resolution mode (2.3 mV/DAC, in blue) while for a finer tuning in the low charge region a 1.1 mV/DAC step is available. In the following, data are presented in the standard resolution mode only.

In order to estimate the shaping characteristics with integral discriminators, a threshold scan for evaluating the detection efficiency of all the channels is needed. Efficiency is defined as the number of counts divided by the total number of trigger which can be 10 thousands or more to guarantee a statistical error below 1%. When only a single channel per chip is injected the readout introduce negligible dead time up to 100 kHz thus the data collection time for a complete is determined just by the range spanned by the threshold. Figure 3.12 is a typical 60 fC efficiency monitor plot for a 192 channel front end board. A single bipolar signal is present for each of the 64 channel MAROCs standing on a baseline positioned few units below 200 DAC. The analysis program reconstruct completely the hits using both edges information being responsible of the suppression of incomplete hits(out of the window) and causing the observed inefficiency at undershoot threshold level. Thresholds too close to pedestal cause a huge amount of spurious hits from electronic fluctuation of the baseline that saturate the readout capability. As a result blank spaces of 16 contiguous channel sharing the same TDC firmware resources are present in the pedestal region. With threshold positioned few units above the pedestal of each MAROC, an clean discrimination power down to few fC is obtained.

Fast shaper has been designed for self-triggered charge measurements with a high gain transfer function to select all the channels participating and events thus allowing precise energy and position reconstruction in scintillation pulse analysis system. A characteristic curve is shown in figure **??** where the pulse height of the fast shaper in DAC units is plotted as a function of the injected charge. The cut off position can be changed in the range 100-200fC by adjusting the feedback network of the shaping amplifier.

This kind of plots can be conveniently used to estimate the threshold DAC in physical unit. Numerical method would allow the conversion in all the dynamic range, loosing sensitivity as the charge exceed the cutoff. For sake of simplicity and because the range of interest is in the small charge region,

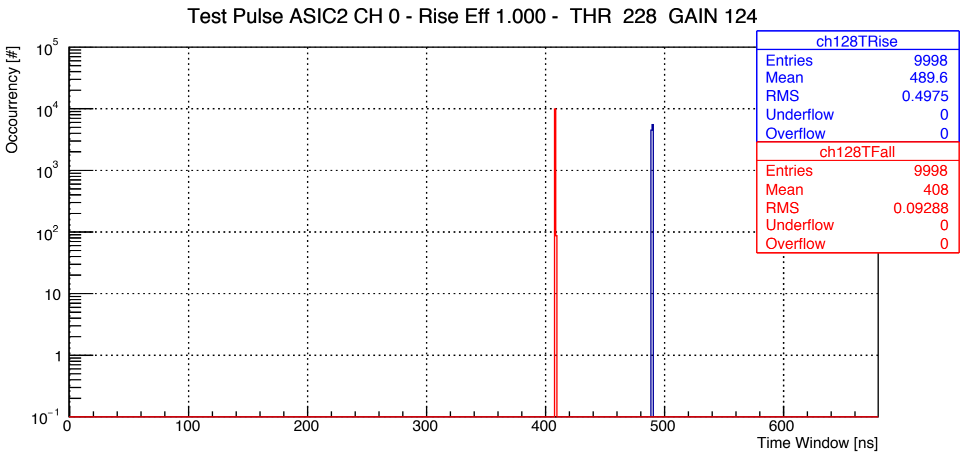

Figure 3.13: TDC response to on-board pulse generator at fixed charge

below $100fC$, a linear calibration has been attempted giving 1.3DAC/fC as visible in figure **??**. The important results is that the system exhibit an excellent sensitivity down to 5fC, ten times smaller than requirements.

3.4.2 Timing characteristics

A typical TDC spectrum for leading and trailing edges of the logic pulses obtained with the on board pulser at fixed threshold is shown in figure 3.13. The distributions appear as spikes in time with RMS fluctuating from 0 to 500ps depending on the phase shift with the 1 ns clock. Generally the fluctuation of a logic pulse is called jitter and it is minimum for steep slopes or, in other words is a decreasing function of the charge collected by the sensor and occasionally by the signal processing system. In fact MAROC manufacturer declares 40 ps jitter at 1 pC and 200 at 50 fC (PSHP14 Workshop, Frascati) well below our sensitivity. Since the CLAS12 trigger will be distributed with 1ns precision, the firmware has been designed to do not exceed this limit. We can conclude that the TDC system satisfies all the requirements for the RICH use in CLAS12.

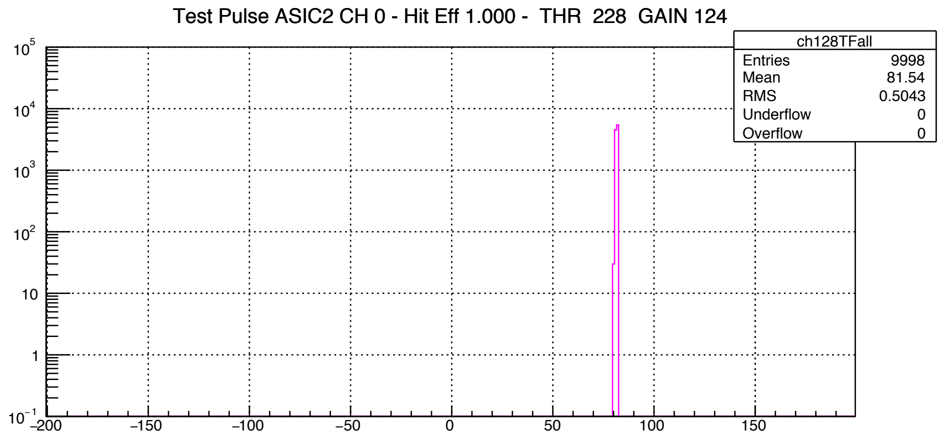

Figure 3.14: Time Over Threshold distribution for on-board pulse generator at fixed charge

Time walk correction

Edges information can be used to reconstruct the hit duration and correlate it with the injected charge. An example is showed in figure 3.14 This operation becomes our standard allowing for logic pulse duration studies but its completely equivalent to the study of the pulse shape by means of leading and trailing edges.

At fixed threshold the correlation between time and duration is below the system sensitivity (1 ns). When the charge is varied a walk effect can be observed due to the finite rise time of the fast shaper output. For studying this effect the on board pulser is used in sliding mode allowing completing the single channel calibration with a simple correction. Since this correction is a precious resource when the electronic is used to read out real sensors to optimize the timing performance, it is described in 4.2.3.

3.5 Crosstalk

In an ideal imaging system every channel is an independent signal processing element. Whether current is measured, the activity of one channel does not affect any others. In a real a multi-channel system this is not the case. Spatial proximity of the signal paths and bias lines sharing determine some level of mutual contamination that can be responsible of artifacts in the data depending on the sensitivity of instrumentation. By a punctual investigation of crosstalk effect in the MAROC board and ADAPTER board it is possible to use the this knowledge to mitigate this undesired effects.

3.5.1 External injector test

During prototyping of the mixed analog-digital front end boards many sources of coupling have been identified and fixed by deeply changing the initial routing. However the spatial proximity of the input circuits was unavoidable even in the production layout resulting in some level of coupling between adjacent input lines. With the injection of a controlled amount of charge in the anode input, one channel at time, it is possible to estimate the characteristics of the signal induced on the neighbor channels and possibly reduce the impact it in the readout data quality. Few level of charge were used to estimate the amount of crosstalk in terms of a fractions of truly injected signal. Even if unrealistic condition of operation,sometimes the preamplifier input was set at its maximum value of 4, to better highlight the effect on both analog and digital measurements.

3.5.2 Estimation using ADC

ADC was used, at the beginning, in waveform reconstruction mode, to understand the nature of the coupling by looking at its shape characteristics. Figure 3.15 shows an example. The two panel refers to the injected channel (top) and one of its neighbors (bottom). The spurious signal appears small and early, a clear indication of a capacitive coupling for its derivative-like aspects. We have to remember that what we are seeing here is an averaged signal of the slow shaper output, obtained with a hundred samples per hold delay so it is not a direct observation of the signal at the MAROC input but a reconstructed waveform after the shaping thus filtered by it. However the observations have a general validity. In particular:

1. The ADC measurements, operated at fixed delay on the maximum of the injected channel waveform, will be weakly affected by the crosstalk

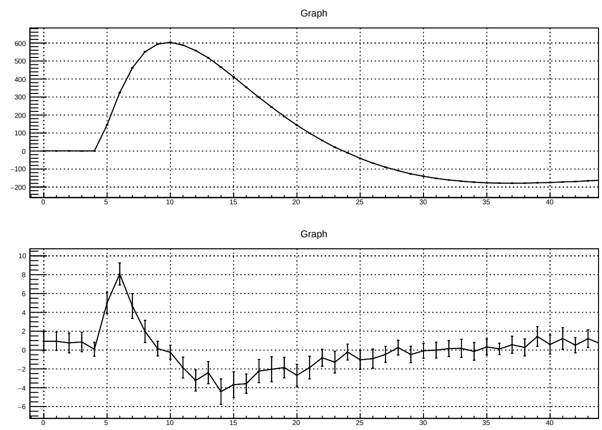

Figure 3.15: Cross talk estimation using ADC waveform reconstruction mode. Amplitude in ADC units and time in clock ticks units(8 ns)

because of the capacitive coupling. Depending on the channel and on the charge, the pulse height measured by adjacent channel will be compatible with the pedestal or constitute a feeble shoulder of it.

2. The induced signal can create ghost logic pulses on the if the binary threshold is low (which is our desiderata). The spurious hits will be produced earlier than the true one and will have smaller duration.

3. The charge induced at input level can be estimated by measuring the peak amplitude of the ADC reconstructed waveforms and the this quantification can be used to predict the presence of spurious hits in the binary data.

Tables 3.5 3.6 reports the crosstalk estimation for few charges at SPE level and for two representative channels.

What is important to our scope is to determine the amount of charge injected in adjacent channel because of its impact on the threshold settings. Since a low threshold is desirable for the detection efficiency a high level of crosstalk could deteriorate the final resolution on hit position.

After a having performed a calibration for the two channel on study the maximum ghost charge created by the readout system for true signal input at SPE is 10 and 25fC respectively.

3.5.3 Estimation using TDC

For a direct estimation of the impact of the crosstalk on binary lines a threshold scan can help in assessing the level of this source of noise. Due to a higher

Channel 158	SMALL Crosstalk		
Charge [fC]	Amplitude [ADC]	Xtalk left [%]	Xtalk right [%]
550	406	1.6	1.5
740	546	1.7	1.6
940	691	1.7	1.5

Table 3.5: Crosstalk quantification. Calibration factor, derived from this data is 1.368 fC/ADC so the maximum induced is at the level of 10fC charge for this channel

Channel 183	HIGH Crosstalk		
Input [fC]	Response [ADC]	Xtalk left [%]	Xtalk right [%]
180	125	4.0	3.1
350	245	3.3	2.8
516	360	2.7	3.0
680	471	3.2	3.2
825	564	3.0	3.0

Table 3.6: Crosstalk quantification. Calibration factor, derived from this data is 1.476 fC/ADC so the maximum induced charge is 25 fC

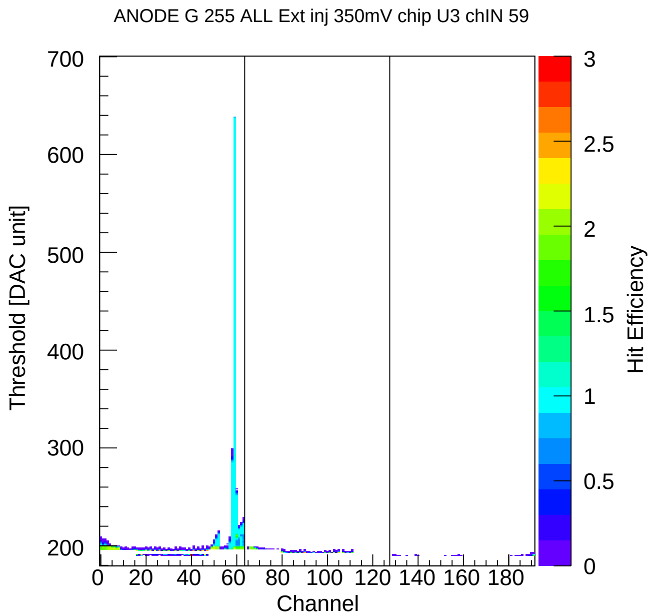

Figure 3.16: Anode input injection

gain the injected channel amplitude response is typically saturate and for quantitative estimation only the nominal charge injected can be used. On the contrary the crosstalk signal on its neighbours is in the linear region so the height from the pedestal expressed in fC is a direct measurement of the induced charge level. In the case presented in figure 3.16 the external input charge is 350 fC on channel 59 , and the first neighbours channels have an amplitude at the level of 92 and 50 DAC units. Considering that the preamplifier gain was 4 (gainword = 255) and a calibration factor of 1fC/DAC the crosstalk charge level is about 23fC and 12 fC corresponding to a 6.6% and 3.5%.

Such level cannot be considered negligible or small. Maybe acting on the shaping constant, at chip level, the amplitude of the induced signal can be reduced by limitation on the band pass, but for sure other mitigation techniques have to be put in place.

As confirmation of this evidences a more systematic study with external injector has been performed on all the channels of a tile. Three charge level has been used 200fC, 400fC and 800fC and figure 3.17 represent the crosstalk estimated as a function of the channel for one single chip.

No evident correlation has been found apart of a complete absence of crosstalk in correspondence of the side change in the input connector of the MAROC board (channel 32) and a weak effect due to reduced pitch used

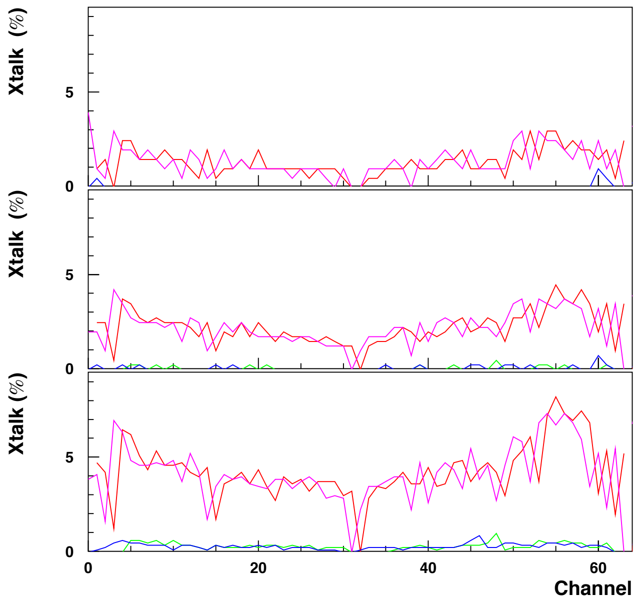

Figure 3.17: Cross talk on TDC

for lines around channel 55 (0.32 mm instead of typical 0.48 mm). Also the differences in the path lengths have been investigated as a possible source of increased capacitance between channels (minimum length is 34 mm and maximum is 55 mm) but none of these parameters justifies the crosstalk pattern observed. Probably the highest impact is given by a non ideal matching of the transmission lines impedance with the one of the MAROC inputs. In the near future more detailed studies will help in clarify this aspect.

For the moment an offline technique based on the difference in arrival time measured with the TDC has been developed and tested with encouraging results. It is described in section 4.2.3 and the results given in section 4.2.4. In terms of impact on CLAS12 and RICH angular resolution the crosstalk hits will not have a significant impact in the data throughput since the data link can sustain even one order of magnitude TDC data without introducing dead time. In addition with a complete characterization of the channels the electronic crosstalk can be identified and suppressed also during the experiments.

Chapter 4

Sensor Test

The complete verification of the quality of the pre-production front end boards can be obtained only by full tile testing with real sensors. In December 2016, as soon as the final prototype revision was ready, a setup for the full chain has been arranged at JLab for this purpose. It will be used for tuning up the optimization procedures and derive the parameters to be inserted in the CLAS12 database before the start of RICH electronic panel assembly in the clean room.

In this chapter the preliminary measurements are presented. After the setup description, example ADC spectra from the two types of the MAPMTs with the same bias will be presented and qualitatively discussed. The successive section is dedicated to the TDC response and to crosstalk studies. The chapter is concluded with dark rate measurements which are the first step of the calibration procedure developed for the monitoring of the detector after the installation in the spectrometer.

4.1 The Setup

As completion of the validation studies of the read out electronics with step function generators and in view of the full RICH tiles characterization that will take place during 2017, a setup has been prepared at JLab by adapting a preexisting experimental apparatus. The previous system was used for the systematic characterization of the 400 MAPMTs produced by the Hamamatsu for the first RICH module and was performed with standard JLAB fADC250 boards. This data set has been used as a reference.

Part of equipment was already available, tested and with software tools ready, thanks to that, the installation and an effective use of the new front end electronics was rapid. The HV power supply boards are plugged is

Tile	Number of MAPMT	X [a.u.]	Y[a.u.]
TOP	3	213	7
BOTTOM	2	199	112

Table 4.1: Laser alignment results for the diffuser setup. The final step motors coordinate for the two tiles have been obtained by scanning the position the efficiency and maximizing simultaneously the hit counts an all the MAPMTs.

a CAENSYS 4527, the same mainframe that will be used for the RICH CLAS12. An interlock system disable the MAPMT bias when the door of the dark box is open. The laser source, a PicoQuant unit with 405nm wavelength laser head, a set of optical density filters to reach single photon electron condition and the step motors for moving the laser head were controlled by the data acquisition PC. A picture of the inner part of the dark box taken during the assemble phase is shown in figure 4.1

A light diffuser has been mounted to reach a uniform illumination condition almost on an area of the diameter of 2-3 MAPMTs and accumulate statistics for the characterization without scanning pixel by pixel with a small spot. In particular the average multiplicity measured at single photoelectron (SPE) level was 7 hit per MAPMT with an average efficiency on individual pixel of about 5%, thus an acceptable SPE condition. Two tiles have been mounted on parallel slits for a total number of five MAPMT (320) channels. The MAPMT were chosen to be representative of the entire set of light detectors (shown in figure 3.9 at page 71). The top tile with a H8500 and a H12700 at the borders and a high dark current in the middle, the bottom one with high an low gain devices, 1×10^6 and 5×10^6 respectively.

The two units were readout independently, at different time, having the FPGA's squared wave generator driving the laser unit for minimum TDC measurements uncertainty. The data acquisition program was adjusted from the one developed for the electronic stand alone test with a script used to manage all the parameter of the apparatus and a logbook file to keep track of the slow control, the laser position, the HV used and all the front end and read out configuration, including the identification of the MAPMTs in use.

The laser alignment has been done at light intensity higher than SPE by keeping the readout system continuously running in scaler mode, with threshold at 0.5 SPE signal and unitary gain, and by moving the laser position along the two independent coordinate X and Y until a uniform illumination on the entire tile was reached. Final parameter are reported in table 4.1.

As the trigger is generated by the FPGA the synchronization of the ADC

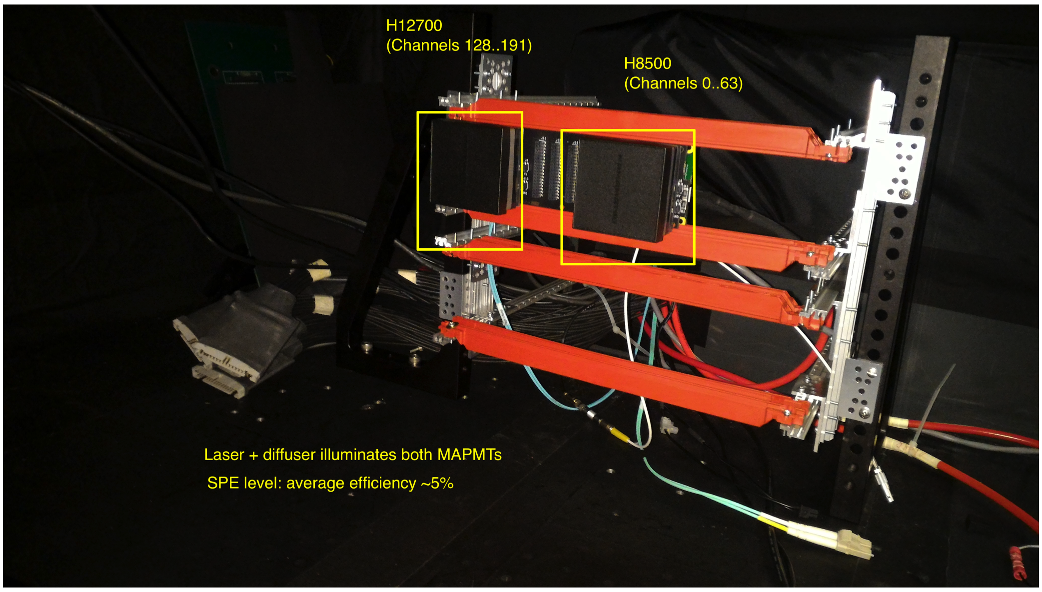

Figure 4.1: Laser characterization setup

measurement and the TC window was performed using the same method described in the 3 i.e. by a *waveform* acquisition mode for the charge measurements (see figure **??**) and by a large TDC window subsequently optimized after the individuation of the recurrent peak of delays. The standard shaping configuration showed satisfying performance and has not been modified. The systematic data taking has been done instead by varying the preamplifier gain and the high voltage bias to start the study of the MAPMT equalization procedures.

4.2 The SPE response

The extraordinary possibility to access single quanta of electromagnetic radiation offered by the vacuum tubes of solid state photosensor has, as counter part, an intrinsic uncertainty due to the unavoidable fluctuations in the detection and amplification gain mechanisms. The RICH front end electronics offers good tools to access this phenomenology and develop quality cut to have an effective hit selection for the ring reconstruction. As discussed in section 2.2.2 the pulse height measurements will be used only for monitoring and calibration while the signal discrimination and timing will be the readout mode for physics quality data acquisition. In this section the performance of both systems is reviewed based on the data collected with the two prototype tiles and on the preliminary version of the time walk correction algorithm.

4.2.1 Pulse height spectra

As a first validation of the readout electronics, pulse amplitude spectra were obtained using the embedded MAROC ADC configured with its maximum resolution of 12 bits. Figures 4.2a and 4.2b show two representative pixel spectra from a H8500 and H12700 devices respectively. The first is a generic position sensitive photomultiplier available since more than 10 years with a 12 stage electron multiplier and an equal voltage divider ratio i.e. the accelerating field of each stage is 1/12 of the applied high voltage bias [17]. Originally designed for gamma ray imaging its feasibility at single visible photon level has been demonstrated with MAROC readout in 2012 [8]. It is a good example of how the separation of the different field is a good organization for didactic purposes, but that science, as all the human activities, proceeds in a way that is difficult to rigidly schematize. I like the fact that our field of fundamental research is closely connected to medical imaging with potentially tangible results for the society we live in on both long and short terms.

The H12700 was released by Hamamatsu in 2015 as a single photon dedicated variant of the H8500 and made commercially available for the CLAS12 RICH at the same price of the older model. The main differences between the two are a revised first stage electromagnetic lenses to better focusing the photoelectron into the electron multiplier and a reduced number of stages (10 instead of twelve). Both uses bialkali photocathode thus have the same spectral response and uses a grid electrode between the last dynode and the readout to obtain the pixelization on a matrix of 8 by 8 anodes.

Looking at their spectra the specialization of the H12700 in comparison with the H8500 appears evident. As confirmed using a new analytical model to describe the SPE spectra [25], the first dynode gain is higher and contributes to form a narrower response ot the MAPMT. The higher accelerating voltage helps also in the observation of the peculiar phenomenology of photomultipliers. In facts the well separated peak, that is visible between the pedestal and main peak, can be interpreted as direct photon conversion on the first dynode. Its smaller measured amplitude is due to the fact that there is one stage less of amplification and because its arrival time is anticipated since the collection stage is covered by the photon at the speed of light instead of by the electron moving of constant accelerated motion in the electrical field.

This observation are just preliminary and will be systematically studied during 2017 by the CLAS12-RICH collaboration. For the moment it is good to observe the excellent single photon resolution offered by the designed front end system that allow to access the entire phenomenology of the sensors with

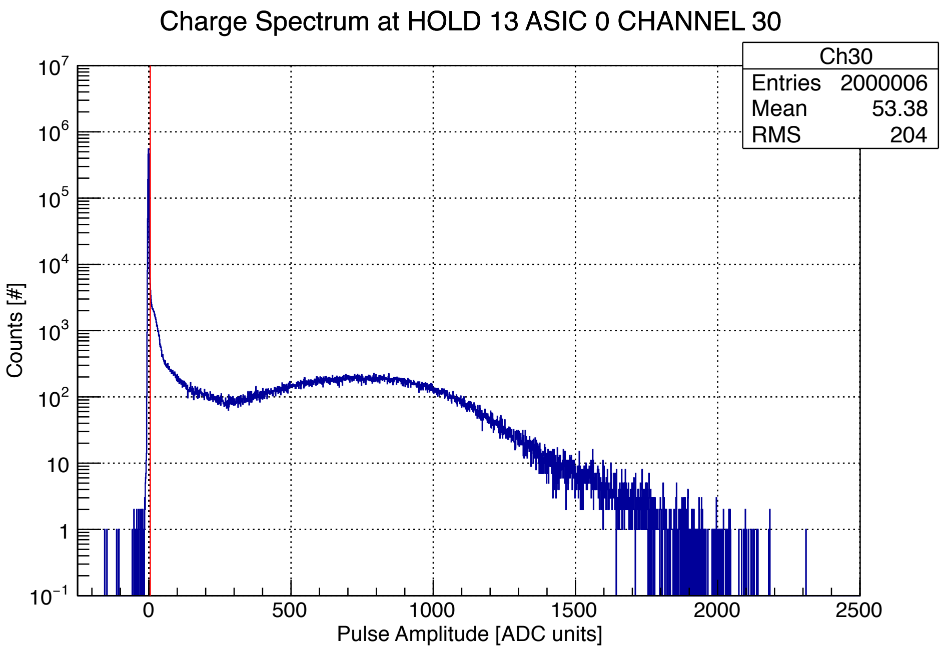

(a) H8500

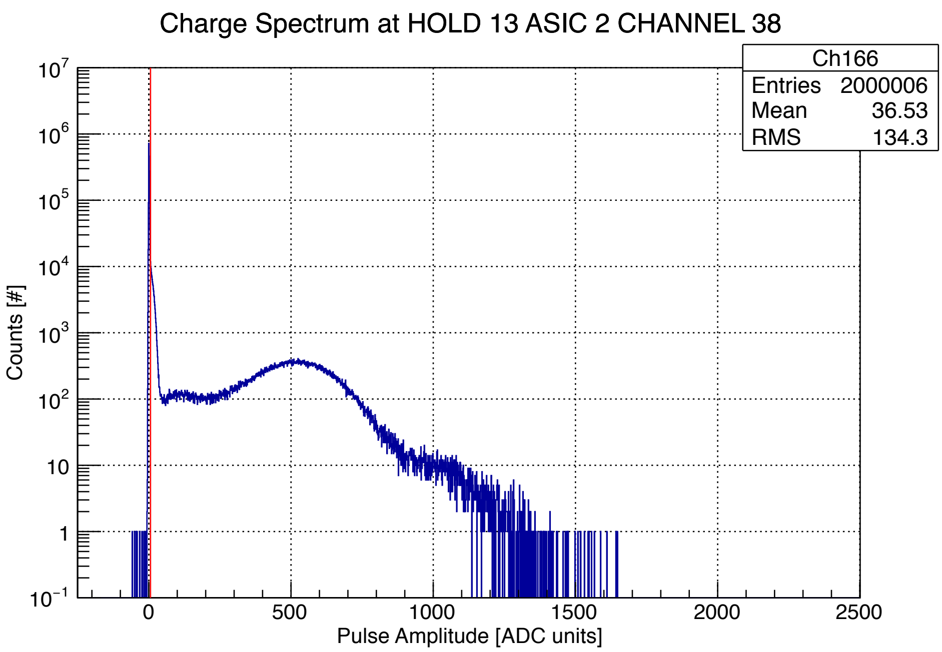

(b) H12700 individual pixel pulse amplitude spectrum

Figure 4.2: Individual pixel pulse amplitude spectra. Even if the global gain is higher for the H8500, the specialization of the H12700 device appears evident in a better SPE. Pedestal subtraction is part of the data processing as well as the five sigma cut calculation (vertical red line) for efficiency estimation with ADC

high precision. The extremely small noise pedestal presented in 3.2 allows for optimum quality data cut with a negligible fraction of signal lost (not estimated at the present).

It is also nice to observe the few events with amplitude below the pedestal. They are present also when the photon sensor is powered and the laser if off and are due to the uncorrelated sampling of the dark pulses of the photomultiplier due to thermal excitation of the electron in the photocathode. They will be detected and characterized using the self triggering capability of the RICH electronics. As will be presented in the next section this data acquisition mode has not been used yet, but some preliminary measurements have been done using scaler acquisition mode as presented in 4.2.2.

4.2.2 Signal discrimination

As a consequence of the of the late availability of the production-quality frontend board prototypes This thesis work does not present systematic studies with the photosensor. An overview of the preliminary measurements is presented instead. Complete results will be possible only after the full production of the frontend boards.

Figure 4.3 shows the detection efficiency as a function of the pixel ID of a 2MAPMT tile and of the common discriminating threshold parameter. Efficiency is defined as the number of detected hit divided by the total number of trigger sent to the laser unit. The single photon electron regime is defined as the light intensity level that produce a negligible contribution of two electron levels at the photocathode. Since that at the quantum level of operation the behavior of a photocathode can be described as Poissonian current source with average intensity (and variance) determined by the number of events in which few photons, the estimation of the average intensity can be obtained by the number of pedestal events. Values around few percent indicates that the pulses are mostly started by a single electron or, in other words, that the probability of a pulse to be generated by two simultaneous electron is negligible.

For both MAPMTs the measured efficiency is around 5% with a weak dependence on the threshold and on pixel. This tells that the charge injected in the signal processing system is on average capable to saturate the output of the fast shaper and, as a consequence, threshold can be adjusted with pretty large freedom without affecting dramatically the efficiency. Second, the presence of patters, i.e. correlation with pixel ID, is an indication that the photocathode efficiency or the laser illumination are not uniform . In absence of systematic data we cannot asses if one or both sentences are valid. We can conclude that the readout system allow us to access very peculiar information

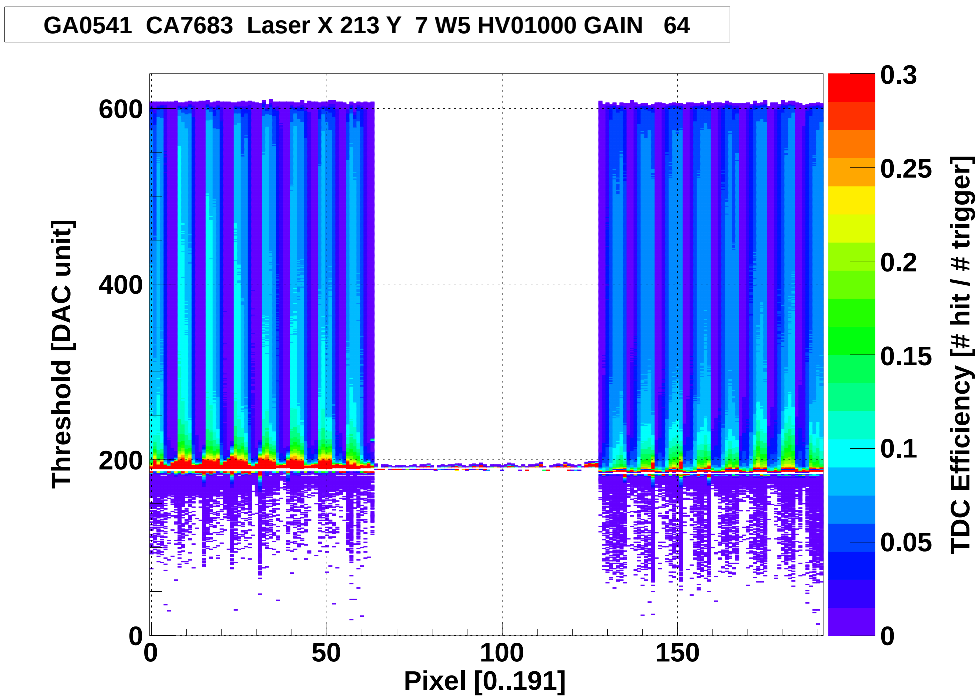

Figure 4.3: Laser detection efficiency as a function of the individual pixel of the MAPMT (*x-axis*) and of the common MAROC threshold *y-axis*. No preamplifier gain correction is applied to equalize pixels, G = 64 correspond to unitary gain for all the channels. TDC data (July 2016, JLab)

on light illumination, with a small threshold dependence, and hopefully will provide an excellent performance in reading out the RICH photon detection surface.

Dark rate current monitor

A part from the verification of the data driven acquisition mode or self-triggering, no systematic studies have been performed with this setup on the highly variable dark current of the photomultipliers of the RICH detectors. The low extraction work function of the photocathode material, that determines the visible spectral response, is also responsible for the vast majority of spurious pulses that can be observed from the tubes. In facts the thermal agitation and the presence of an accelerating field in the vacuum space between photocathode and the first dynode can occasionally extract electrons from the atoms close to the surface and generate an avalanche that is indistinguishable from the one originated by the photoemission. This phenomenon give rise to the so-called dark current which is an important parameter of

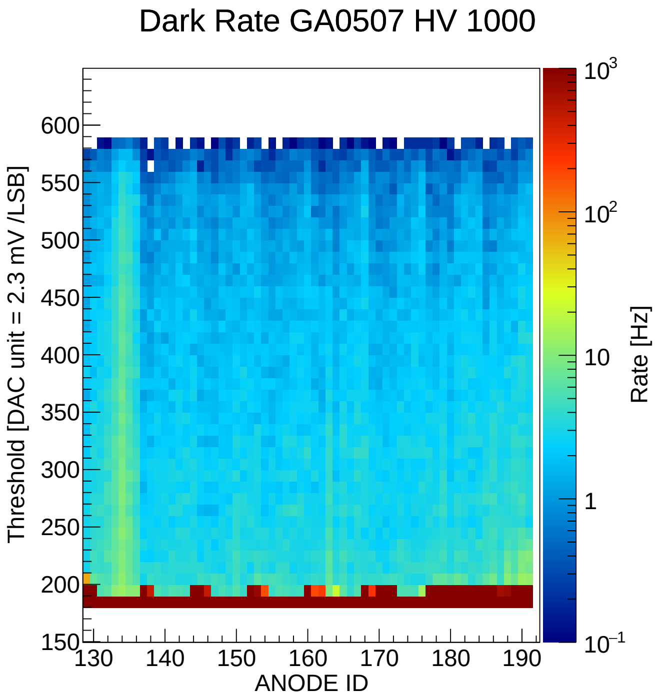

Figure 4.4: Individual channel dark rate measurement for a generic H8500 photomultiplier (scaler mode, July 2015). The MAMPT was readout by the third MAROC of the board so the pixel number has an offset of 128 channel.

any devices working at single photon level. For example the PMT exhibit an extremely smaller dark current at the level of few $\mathrm{Hz/cm^2}$ in comparison the SiPM that generates hundreds of $\mathrm{kHz/cm^2}$.

In a detector such as RICH this spurious emission can occasionally be readout together with Cherenkov light and only partially suppressed offline using spatial and time correlation criteria. The number of expected dark hit in the data can be calculated by multiplying the dark rate for the pulse duration as seen by the readout system (shaped and digitized) and dividing it by the width of the read out window. The probability is very small for single channel, but considering that the surface is composed by about 25k pixels few dark counts per event are expected to be normal in the RICH data acquisition.

A direct and simple measurements of the single channel dark rate has been performed using the RICH readout electronics in scaler mode for a H12700 MAPMT and the result is shown in figure 4.4. The scaler acquisition window was 30 seconds to have a negligible error on the measurements expressed in Hz. Values of about 10-15 Hz, on average are pretty in agreement with the one provided by the manufacturer. The majority of the channel exhibits a dark current of few Hz while a small group of pixels show some tens or counts per second. A pattern seems to emerge similar to the one observed in efficiency measurements in figure 4.3. The pixel position for these channels in the physical device coincides with part of the first row indicating that there is a lower work extraction function in that region or, in other words, that the energy levels are slightly different considering edge pixels and central ones. This non uniformity can be accessed only using independent channel electronics and is due to the combination of the photocathode non uniformity and the collection efficiency of tube.

Since the dark background is mainly composed by single photoelectron signal its acquisition in autotrigger mode using ADC will allow to accumulate pulse height statistics and monitor the MAPMT performance stability without the use of other hardware resources (laser or led), simply exploiting the noise. The use of data driven triggering mode will be extended to higher multiplicity patterns to attempt the RICH detector calibration using cosmic rays.

4.2.3 Timing

In section it has been observed that the time resolution of the TDC readout respect the 1 ns requirements for fixed charge injection. This statement is no longer true if input varies in the range from few fC to 1 or 2 pC as in the real sensor case. This fact depends on shaper transfer function's linear and saturate regimes. Figure 4.5 helps in clarifying this concept very familiar to the data acquisition expert reader.

By considering only the detection sensitivity we tend to think that lower the threshold better the performance can be, but this is not true for fixed threshold timing. When the input charge is smaller than few hundreds fC - in the case of fast shaper standard configuration the onset of saturation is around 150fC - the linearity of the response determines a drift in the measured arrival time of the hit. Vice versa higher the charge earlier and more reproducible is the timestamp. As a consequence the time distribution obtained from variable charge input appears asymmetric and with a broader aspect than the one obtained at fixed charge. Globally the time resolution results deteriorated.

The firmware TDC module can read out both hit edges polarity with negligible impact on the data acquisition rate. This allow for the possibility to estimate the charge of a hit during the event reconstruction and apply consequently a correction proportional to charge and obtain a narrower distribution for the logic pulses arrival time.

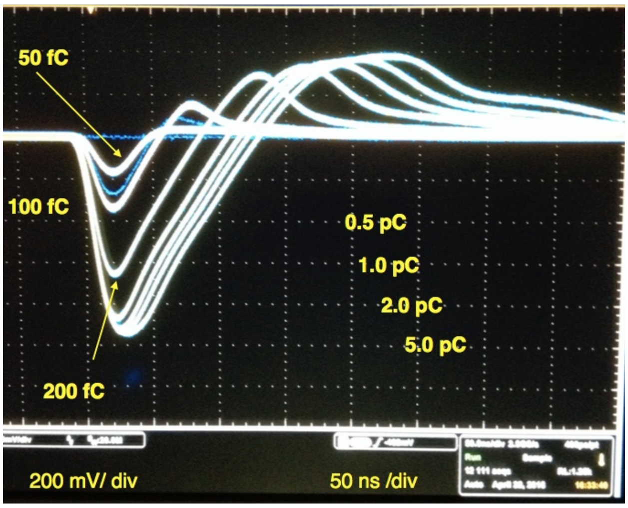

Figure 4.5: Fast Shaper Response to different charge injection. The position of the amplitude cut off can be adjusted with the a group of 4 bits in the MAROC slow control register. Depending on the feedback network of the preamplifier the gain of the transfer function can be varied roughly from 1 to 4 mV/fC.

Figure 4.6 shows as an example a real case application in which the optimization procedures is applied to a hit time distribution of a pixel illuminated by the laser at single photon electron light intensity. On the bottom left pane the raw data have an RMS of about 12 ns. The same information is plotted in the top left plot against the hit duration. The two small spots aside of the main one are delayed emission from the laser as it was verified independently using an oscilloscope, they are not properties of the light detection system and will be neglected. By using a simple two segments line model with parameters obtained from the average on the entire MAPMT, the time response is made independent from the charge as shown by the right column plots. The resulting variance is decreased by a factor 10 (RMS=1.254 ns) and the main peak has now a symmetrical shape and a fluctuation smaller than 1 ns as specified in the requirements.

The range spanned by the duration of the logic pulses generated by the MAROC in response to this particular pixel goes is comprised in the interval from 10 to 70 ns with a concentration of around 50 ns. This characteristics are observed on all the other pixels of the tested MAPMTs and depends on the charge injected in the fast shaper of the front end chip. By a proper MAPMT gain spread compensation, operated with adjustment of the preamplifier gain, the same curve can be used to correct the time walk of all the pixels.

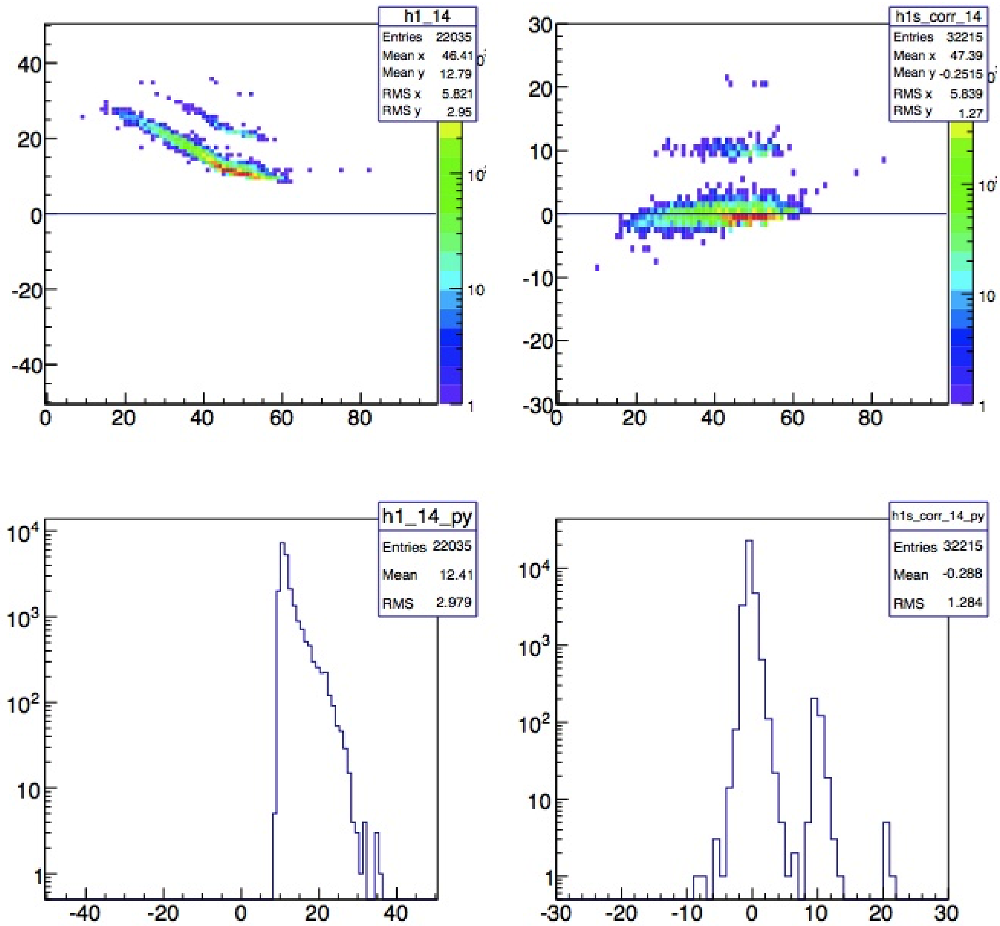

Figure 4.6: Time walk correction. Hit distribution before and after correction (bottom) in nanosecond units. Top plots show the hit time as a function of the duration i.e. the charge. The minor delayed spots are delayed laser emission as was verified independently with an oscilloscope.

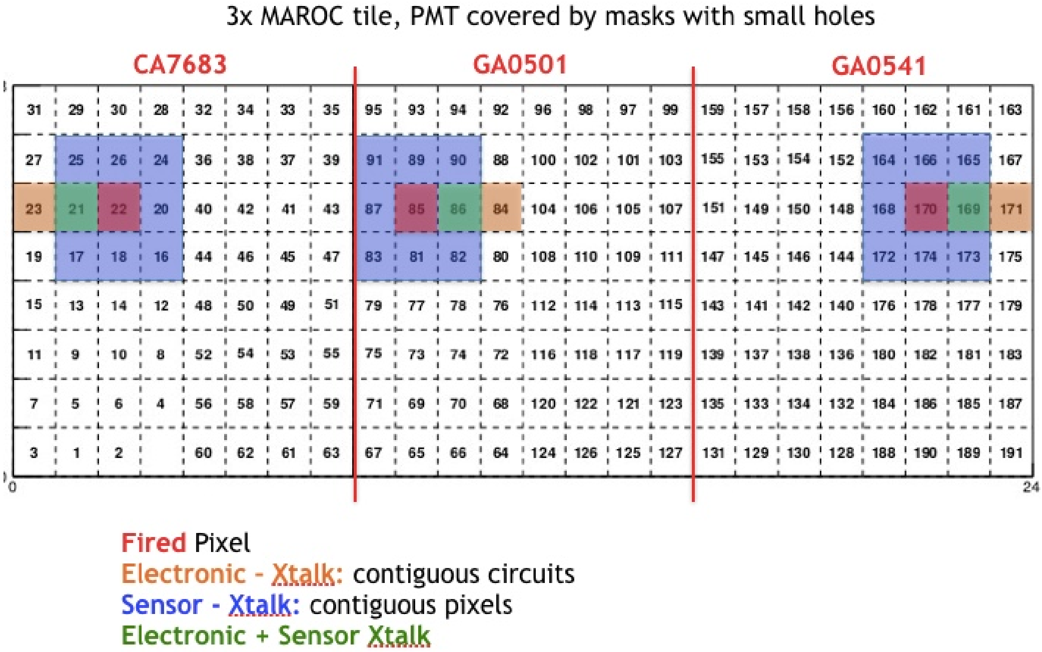

Figure 4.7: Crosstalk setup

This is a first order correction. When a larger statistics, on all the tile of the electronics panel, will be collected the best work point could be determined by adjusting the shaping constants, regulating the cutoff position and so determining the maximum sensitivity for the walk correction algorithm

4.2.4 Crosstalk study with an aperture

As mentioned in section the ADAPTER board routing has been designed with two contrasting ideas in mind: minimize the path length and map adjacent pixel in non-adjacent readout channels. The compromise solution privileged the first principle so that 16 out of the 64 channels of a MAROC have one adjacent circuit that is also contiguous on the MAPMT. Figure 4.7 helps in understanding the mapping: readout channel 22, in red on the left, has 8 neighbor pixels. Among them there is channel 21 which is adjacent also on the MAROC board. The other contiguous readout channel, number 23, is mapped at largest distance in the MAPMT. This pattern is repeated 16 times for each MAPMTs thus one quarter of the total number of pixels experience this condition.

This aspect has been investigated by covering the MAPMT's surface a black cardboard mask. A small aperture has been cut out to illuminate a

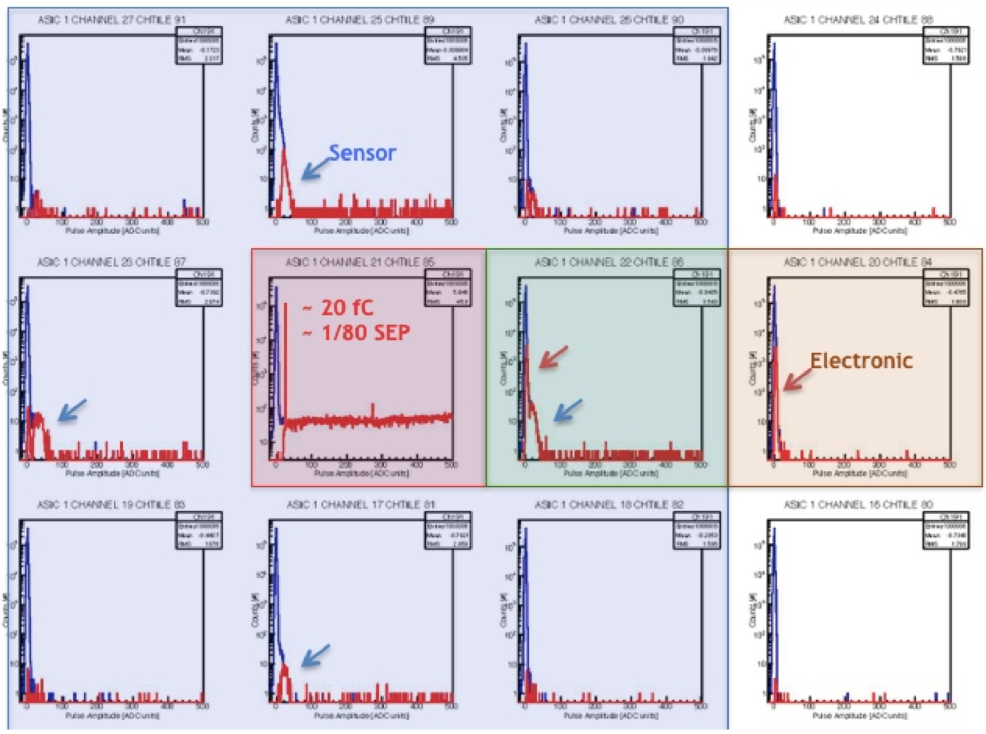

Figure 4.8: Optical and Electronic crosstalk

tiny area of the photocathode, smaller than a pixel. The mask was hand made so the aperture could be not perfectly aligned with the pixel's center however a good single spot illumination has been obtained as shown but the pulse amplitude spectra in figure 4.8. Data were collected using maximum gain for the preamplifier (input charge multiplied by a factor 4) and the x-axis in ADC units has been zoomed to show the pedestal region in detail. On all the pixels few dark pulses are registered. On the ADC information a second histogram in red is superimposed highlighting the digital hits seen by the TDC. The electronic crosstalk appears as a small right shoulder on the yellow pixel (electronic neighbor). On the other hand a more prominent shoulder is evident on the adjacent pixels, this is the optical crosstalk given by defects in the amplification mechanism, capacitive coupling at the anode levels or generally speaking charge sharing effects within the position sensitive sensor. Only one pixel colored with green background present signal coming from both crosstalk mechanisms.

From what has been presented so far in this chapter and in section 3.5 there is some regime in which the data acquisition system have to live with crosstalk. Of course the preamplifier gain plays an important role on the presence of crosstalk in the data and its not hard to imagine that reconstruction

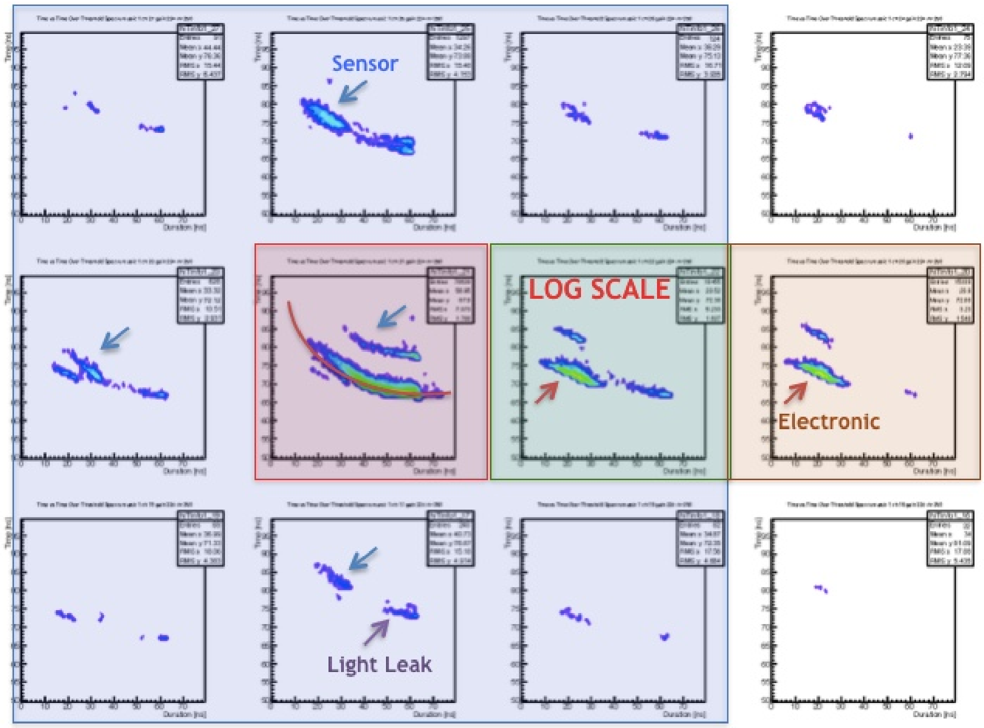

Figure 4.9: Time distribution as a function of the hit duration

algorithms can plays too some sort of suppression to do not deteriorate the RICH angular resolution. This correction is actually made possible by the demonstrated (see section 3.5) capacitive nature of it. In fact the crosstalk signal is faster than the real one and the walk correction can help in its elimination. Figure 4.9 shows the TDC measured time of arrival as a function of the time over threshold for the same the data set. Apart from the delayed laser emissions two other features are clearly visible: the early spot of small duration in the yellow box (electronic crosstalk) and the in time usual duration spots in the pixel adjacent to the one illuminated. These last can be interpreted as light leaks maybe due to the incident angle of the light maybe due to the not perfectly aligned position of the aperture with respect to center of the pixel. However as shown in figure 4.10 the walk correction allows to select good and bad hits by an acceptance time window.

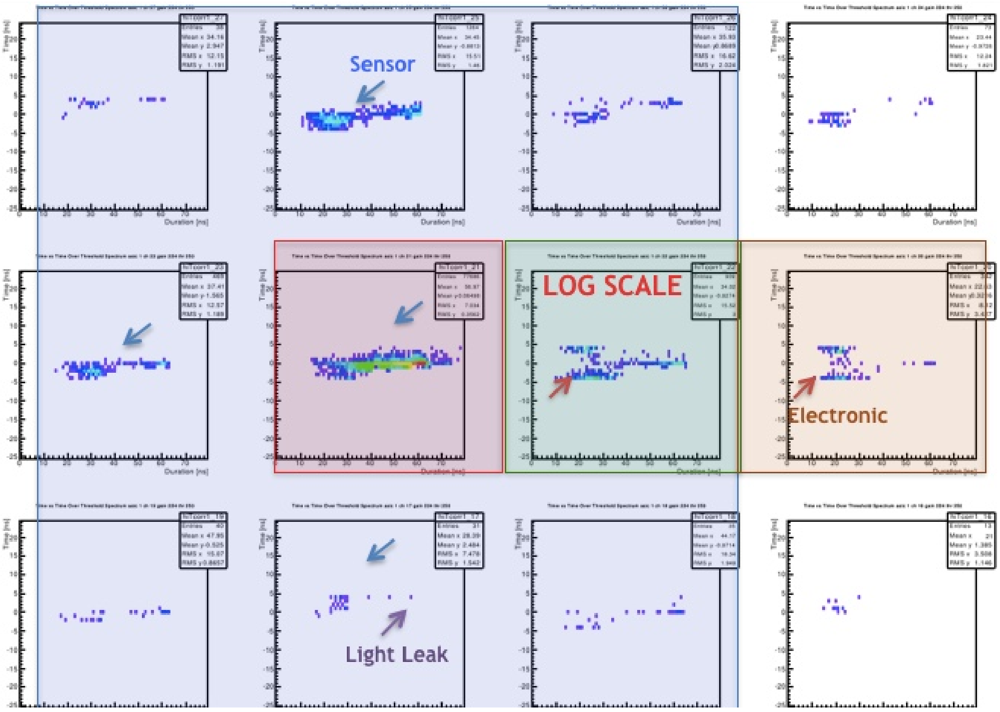

Figure 4.10: Walk corrected time distribution

Chapter 5

Real condition operations

Real condition testing provided the necessary feedback to move new hardware from prototyping to production stage and suggested the final tune up of components in respect to the computer simulation. Here the use of RICH electronics as readout unit for Cerenkov light is reported together with results of irradiation tests performed to asses its availability over the 10 years of experiment life cycle of CLAS12. In all the tests the candidate was in charge of the front-end electronics and of the data acquisition system.

A beam test was conducted in April 2016 at Fermilab in the framework of preliminary studies for the future Electron Ion Collider (EIC) facility using a 120 GeV/c proton beam, it demonstrated the feasibility of the MAROC binary readout for RICH detectors. Irradiation tests, performed in the end on 2015 using 14 MeV/c neutrons and 662 keV gammas have been conducted at two facilities in the Rome area, the Frascati Neutron Generator (FNG) and the Italian National Institute of Health (ISS, Istituto Superiore di Sanità). Another section is dedicated to the description of the setup and of the main results of the first RICH prototype readout with a MAROC electronics implementation derived from medical imaging. That prototype was successfully validated in 2012 at CERN as documented in [26] and later in [8]. Sections are presented in chronological order with the recent Fermilab test results at the end.

The R&D activity is still ongoing, for example with the adaptation of the RICH electronics to solid state position sensitive detectors. Latest contribution [27, 28, 29] have been presented few months ago at the RICH2016 and will be soon published as part of the conference proceedings.

5.1 Test beam with large scale prototype

The CLAS12 RICH configuration is challenging in two major points: (i) the 1:500 pion rejection factor necessary to correctly identify kaons at momentum as high as 8 GeV/c, that requires a large number of photons to refine the angle resolution and (ii) the number of photons surviving the multiple pass through the aerogel. Some aspects of these questions have been addressed in laboratory tests, as for example measurements of the optical properties of the aerogel **??** or the single photon response of the MAPMTs [20]. However, a necessary step of the project is the validation of the proposed RICH working principle in conditions as close as possible to the real measurements. For this, a campaign of test beams has been undertaken in 2011 and 2012, using hadron as well as electron beams and prototypes of increasing complexity.

A first, preliminary, test has been performed in July 2011 at the T9 beam line of CERN using a simplified prototype, made by an aerogel radiator of variable thickness and refractive index, about 30 cm of gap and eight MAPMTs H8500. The charge readout was derived from a compact electronics developed for Medical Imaging[30]. This first test showed that the chosen MAPMTs in conjunction with the MAROC were actually capable to detect single photons also in the real experimental conditions and that the photon yield was sufficiently high to encourage further studies. In 2012, a test has been performed at the Frascati Beam Test Facility (BTF) in order to setup the necessary acquisition system. Finally, two new test beams have been performed using a large scale prototype specifically designed to provide the proof-of-principle of the RICH detector. These tests have been done at the T9 test beam of CERN. Results of these tests will be extensively discussed in the this sections.

5.1.1 T9 experimental setup

The main tests of the RICH prototype had been performed at the T9 beam line located in the East Area of the PS/SPS complex at CERN. The primary proton beam is sent to a target to produce a secondary beam. Different targets, magnets and collimators allow to select the secondary beam composition and energy. The prototype test run hadron beams with negative charge and momentum between 6 and 8 GeV/c, the maximum range covered by CLAS12. The relative population of $\pi^- : K^- : \bar{p}$ is estimated to be $160 : 5 : 1$ respectively. The time structure of the beam is determined by the extraction of one or more spills from the primary PS proton beam. Each spill had a duration of 400 ms and the period of the PS operation was 40 s, so that the overall duty cycle was about of few percent.

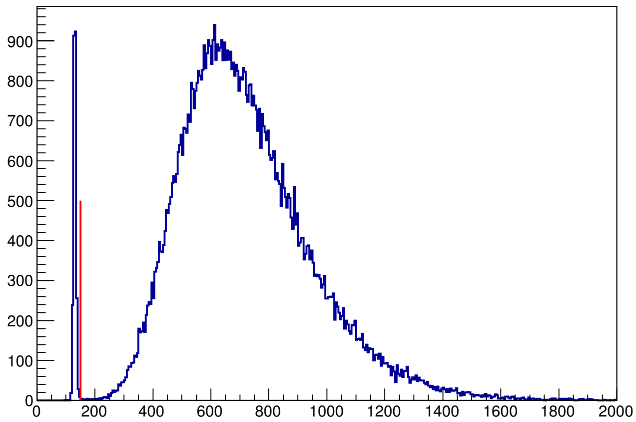

Figure 5.1: Typical ADC spectrum of the T9 Cherenkov counter. The red line indicates the offline threshold used to separate pions from heavier hadrons.

In order to assess the performance of the real-scale RICH prototype under test, the T9 experimental setup comprised several detectors for ancillary measurements, i.e. pion tagging, tracking and triggering.

A gaseous threshold Cherenkov detector (part of the T9 equipment) has been used to separate pions from heavier hadrons by adjusting the gas pressure, i.e. the refractive index. During the test it was set to have only pions above threshold. The sample ADC shown in 5.1 shows a broad distribution due to pions and a narrow pedestal peak produced in correspondence of below-threshold kaons and anti-protons. A standard 5σ cut (channel 150) is used to tag pions.

Beam particle's trajectories are measured through two planar Gas Electron Multiplier (GEM) chambers, installed outside of the RICH box at about 4 meters from each other, with the downstream one about 80 cm after the MAPMT plane. Each chamber is 10×10 cm^2 and is readout in 256 strips for both x and y. In each event, the strip signals are sampled three times at 20 ns intervals, thus good signal are searched for by looking at peaks in the strip ADC distributions of all the 3 samples. A good GEM hit is obtained by any pair of signals measured with correlated amplitudes on the two planes of one chamber. A good GEM track is reconstructed by matching one hit on the first GEM with one hit on the second GEM. The average GEM efficiency is of the order of 30%.

Finally, two small plastic scintillators were placed at the end of the beam line, just after the second GEM chamber, to define the trigger signal of the DAQ system.

5.1.2 Large-area prototype

In the real detector, the particles are revealed basically in two different conditions:

- for forward particles, the Cherenkov photons are directly detected by the MAPMTs;
- for large angle particles, the photons are detected after two reflections and a double pass through the aerogel radiator.

The third condition, in which part of the photons are detected directly and part after reflections, can be extrapolated from the two previous ones. Therefore the prototype must be flexible enough to be operated in two configuration. The RICH prototype has been build inside a large (approximately $1.6 \times 1.8 \times 1.6$ m^3) light-tight box, with internal modular supports holding the various components, that may be inserted or removed.

Direct light configuration

Figure 5.2 shows design and realization of the prototype for direct light measurements. The Cherenkov light is produced on the aerogel radiator, propagate for 1 m inside the box and is then detected by an array of 28 MAPMTs, alternated of the type H8500C with normal glass and H8500C-03 with UV glass. The aerogel support can host tiles of approximately 56×56 mm^2 and of different thickness. The MAPMTs are mounted on a circular support and can be radially moved to intercept the Cerenkov ring produced with different opening angles depending on the refractive index. The ring coverage varies between about 90% for a minimum MAPMT radial position of 280 mm and 60% for the maximum radial position of 400 mm. The main goals of these measurements are:

- study in details the Cherenkov angle resolution, also by varying the aerogel thickness and refractive index, as a function of the number of detected photons;
- measure the π/K separation up to 8 GeV/c;
- estimate the pion detection efficiency;
- study the backgrounds, in particular from Rayleigh scattering.

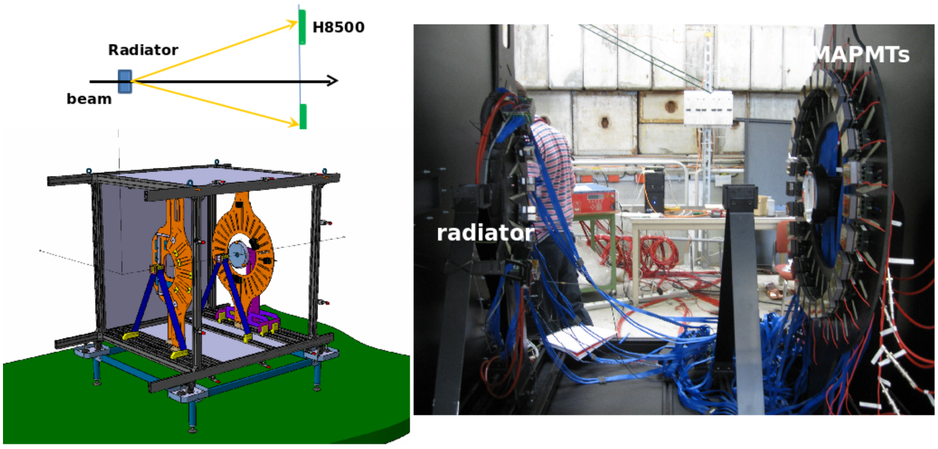

Figure 5.2: Top left: concept of the direct light measurements. Bottom left: drawing of the prototype. Right: picture of the prototype.

Reflected light configuration

Figure 5.3 shows the setup for the reflected light measurements. In this case, the aerogel support is placed closer to the MAPMTs plane, a spherical mirror reflects the Cherenkov photons back toward a system of eight squared planar mirrors which send the light to the MAPMTs. The mirros were made of glass and produced by the Marcon company. The spherical mirror had a diameter of 25 cm, a focal length of 90 cm and a hole in the center to not interfere with the beam. The planar mirrors have a 10.5×10.5 cm^2 area. The MAPMTs are mounted on a support similar to the one used for the direct light case, but optimized to better match the coverage of the planar mirrors and the bigger Cherenkov ring radius due to the larger photon path. The ring coverage runs from about 75% (minimal radial position of 350 mm) to 50% (maximal radial position of 540 mm). The planar mirrors may be moved longitudinally to optimize the total gap length with respect to the focal length of the spherical mirror and to maximize the focusing of the light cone. The supports of the planar mirrors are designed to allow the insertion of tiles of aerogel, in order to study the photon yield absorption within the aerogel.

For these measurements, the main goal is the study of the depletion in

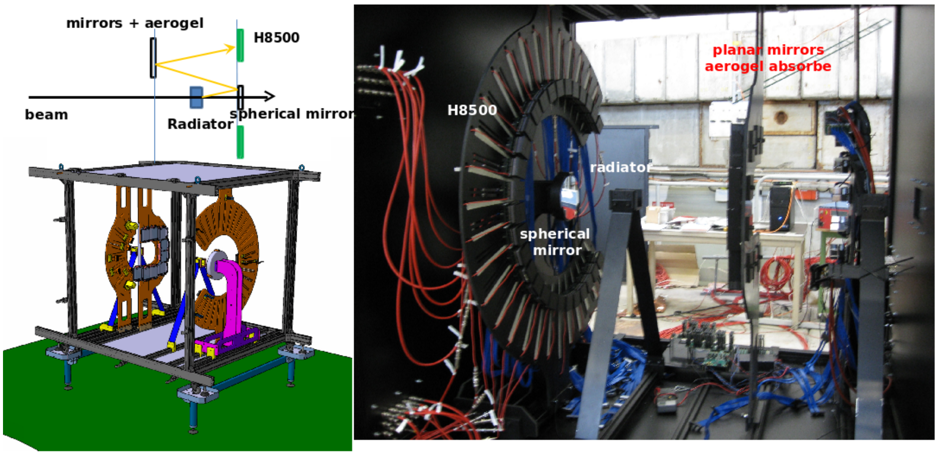

Figure 5.3: Top left: concept of the reflected light measurements. Bottom left: drawing of the prototype. Right: picture of the prototype

the photon yield due to the multiple passes of the Cherenkov photons in the aerogel, namely:

- compare runs without or with aerogel absorber in front of the planar mirrors;
- optimize the aerogel thicknesses;
- compare the optical quality of different mirrors;
- study and optimize the photon yield and angle resolution as a function of the characteristic of the optical elements.

Additionally, one could also study the π/K separation and the detection efficiencies. However, we must stress that the geometry of the prototype is different from that of the CLAS12, thus the results we have obtained will not be indicative of the final RICH performances. On the other hand, they will be used to tune the Monte Carlo simulations, that ultimately will provide us the expected performances of the detector.

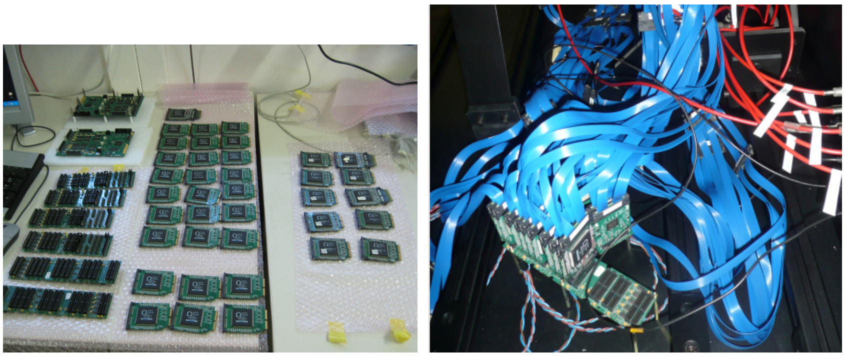

Figure 5.4: Left plot: the various components of the MAROC3 electronics. Right plot: the assembled setup installed in the RICH prototype box.

Electronics and DAQ

The prototype is made by a circular array of 28 MAPMTs. They are Hamamatsu H8500, alternated of the type H8500C with normal glass and H8500C-03 with UV glass. The sensors have a 8×8 pixel matrix for a total of 1792 pixels to be read out. The signal processing and data readout system is based on MAROC front-end. The readout system shown in 5.4 was originally designed for medical imaging investigation with Single Photon Emission Computer Tomography (SPECT) technique. It was adapted to match the geometry and the working conditions of the RICH prototype, in particular external triggering functions were added and, in view of the necessary cables, a common noise algorithm was developed to mitigate the effect of noise picked up over the 1 meter separation between anodes and front end processing circuits.. Three back planes provides power supply to the front-end cards and data connection link with controller boards. The latter, in charge of managing the configuration and the readout, contains basically a system of active transceiver and an FPGA that interface the system with the acquisition node using a USB2.0 link. At each trigger the charge is measured for all the channels and serially converted using external ADC present on board[1] Due to a big trigger latency, the pulses are sampled on the undershoot. This was a sub-optimal working condition, limiting the dynamical range, but still valid in terms of signal to noise separation.

For these measurements, the main goal is the study of the single-photon

[1]External ADCs were necessary for the first two revision of MAROC i.e. MAROC1 and MAROC2, because of a design issue that made impossible the use of the embedded one. The SPECT electronic implementation inherited this feature even upgraded, by the candidate, with MAROC3 chips.

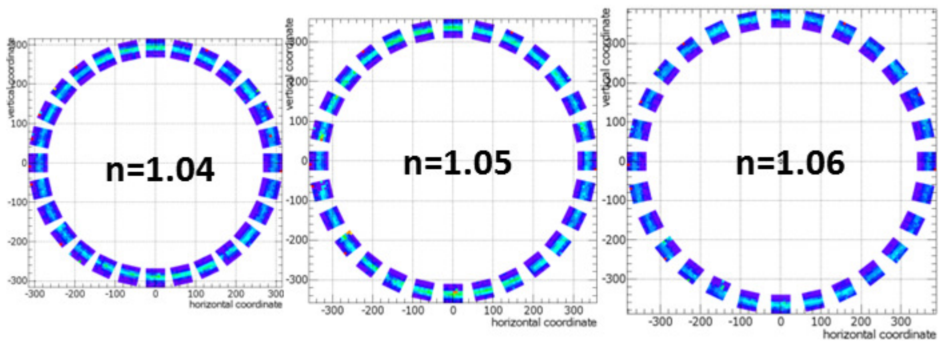

Figure 5.5: Cherenkov photon hit pattern measured with aerogel of different refractive index.

detection response of the system:

- prove the single-photon detection capability of the H8500 sensors;
- test the analog signal processing based on the MAROC3 chip for single photoelectron range applications;
- verify the ability to work in the single photo-electron regime in real conditions: noisy environment and large number of readout channels;
- identify the best configuration for the Cherenkov light readout.

5.1.3 Ring reconstruction

In the prototype configurations, for the direct as well as for the reflected light measurements, the expected Cherenkov photon patterns are rings centered on the projection of the particle's track onto the MAPMTs array plane. MAPMT hits are identified by applying a 5σ cut above the pedestal peak. Examples of the measured hit distributions for different aerogel refractive index is shown in Fig. 5.5.

The Cherenkov rings are reconstructed by minimizing the quantity

$$S(R, X_C, Y_C) = \sum_{i=1}^{N_{pe}} [(x_i - X_C)^2 + (y_i - Y_C)^2 - R^2]^2 \tag{5.1}$$

where (x_i, y_i) are the coordinates of the i_{th} photon hit, (X_C, Y_C) are the coordinate of the ring center and R its radius. The minimization can be performed either analytically or using MINUIT.

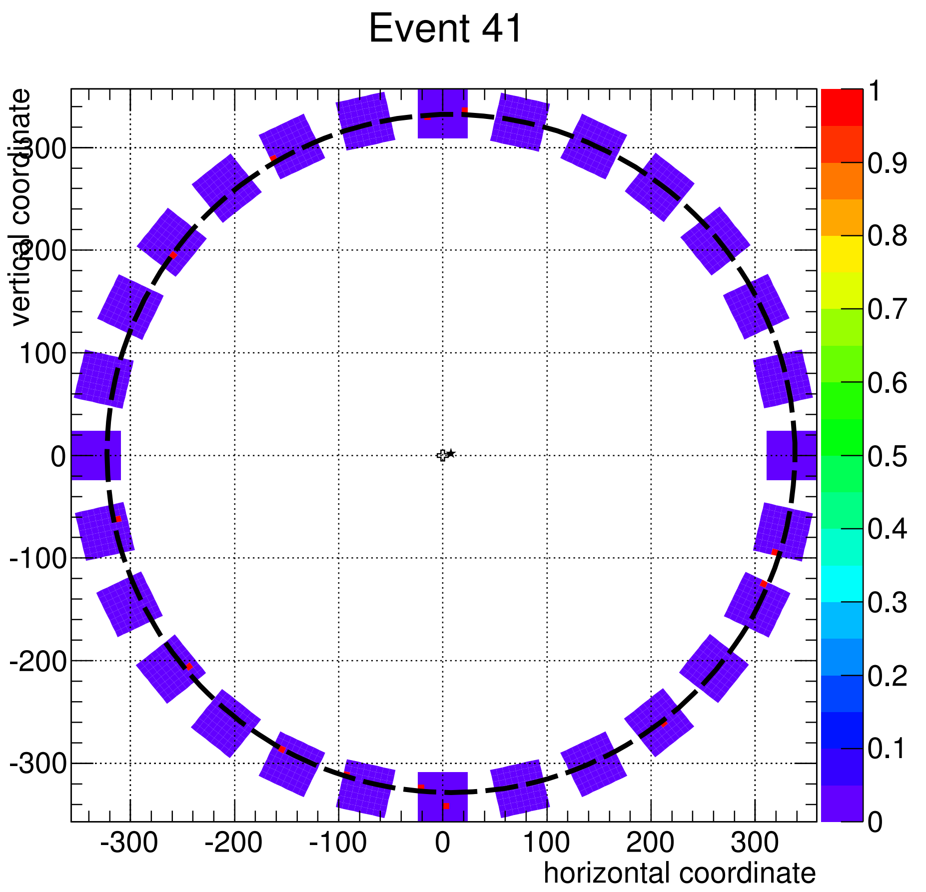

Figure 5.6: Hit distribution of one event measured with $n = 1.05$ and $t = 2$ cm aerogel. The circle show the Cherenkov ring fitted to the hits.

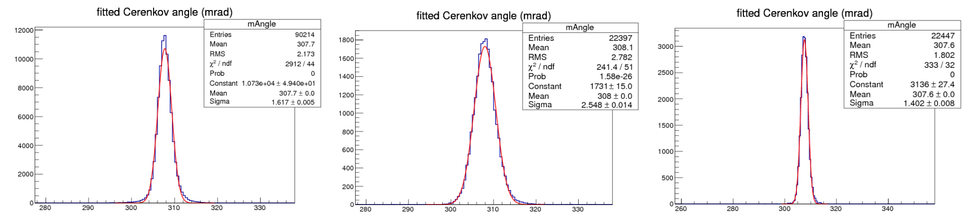

Figure 5.7: Cherenkov ring radius from the *3par* fit (left), from the *1par* fit before (center) and after (right) the GEM alignment procedure.

The Cerenkov angle is then calculated from the known distance D between the MAPMT plane and the center of the aerogel radiator from

$$\tan(\theta_C) = \frac{R}{D} \tag{5.2}$$

In the analysis, one can make the ring reconstruction using only the MAPMTs array, fitting at the same time the center coordinates and the radius (a *3par* fit), or using the center information from the GEM track and fitting only the radius (a *1par* fit). In the latter case, a better resolution is expected, because of the reduced number of free parameters. Figure 5.7 shows the Cerenkov angle distribution from the *3par* fit (left, $\sigma = 2.1$ mrad), from the *1par* fit before (center, $\sigma = 3.3$ mrad) and after (right, $\sigma = 1.8$ mrad) the offline alignment. An improvement of more than 10% in the ring resolution has been obtained from the *3par* to the *1par* fit. In principle, in the *3par* fit 3 hits are sufficient to reconstruct the ring, while in the *1par* fit just one would be enough. However, with such small number of hits the background may lead to incorrect particle identification, thus a minimum number of 4 hits is always required.

5.6 shows, for example, the hit distribution of one event measured with $n = 1.05$ and $t = 2$ cm aerogel, together we the fitted ring. We can identify in this event 12 good hits laying on the ring, plus one hit (in the bottom center MAPMT) far enough from the ring that can be considered as background. Thus, an iterative procedure has been implemented in order to suppress background hits. A hit is considered as background if its distance from the fitted ring is bigger then some cut. In this case, the hit is removed and a new fit is performed taking into account only the remaining good Cherenkov hits. The cut value has been optimized to the data. In fact, a too loose cut will include too many background hits, thus worsening the resolution, while a too tight cut will remove good photons, again worsening the resolution. An optimal value of 12 mm has been found. In 5.8, the total number of

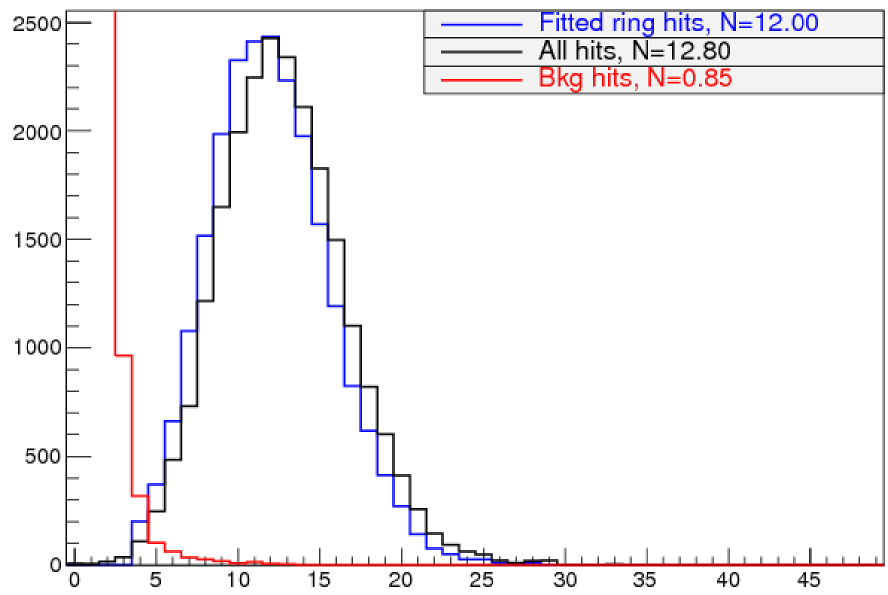

Figure 5.8: Number of MAPMT hit per event: all hit above threshold (black histogram), background hits (red histogram) and Cherenkov hit (blue histogram). Mean values of the distributions are reported in the legend.

hits (black histogram), background hits (red histogram) and Cherenkov hits (blue histogram) are shown. On average, with respect to about 12 Cherenkov hits, we have less than 1 background hits per event. Taking into account the total number of channels in the ring region and the loose time coincidence provided by the ADC measurement, it corresponds to a dark count rate of about 10^{-4}.

5.1.4 Direct light measurements

Because the prototype geometry is very close to the one of the CLAS12 RICH, the results provide a good estimate of the performance of the final detector.

The reference run conditions foresee aerogel with nominal refractive index $n = 1.05$ and $t = 2$ cm thickness and beam with $P = 8$ GeV/c, the highest reacheable in the CLAS12 RICH. After GEM alignemnt, the Cherenkov ring reconstruction is performed with a *1par* fit on events with at least 4 MAPMT Cherenkov hits (after background subtraction).

Pion Reconstruction

Pion events are tagged by requiring a gas Cherenkov counter signal above threshold, see Fig.5.1.

The left panel of 5.9 shows a scatter plot of the Cherenkov angle versus the number N_{pe} of photoelectrons. The distribution get narrower as N_{pe} increases. For a fixed number of N_{pe}, the angle distribution has been fitted with a gaussian to extract mean and width. The mean values do not show any appreciable deviation from the one obtained in the integrated fit (see 5.7 right). The gaussian widths are expected to follow the statistical law:

$$\sigma_\theta = \frac{\sigma_{1pe}}{\sqrt{N_{pe}}} \tag{5.3}$$

where σ_{1pe} is the single photon detection resolution. The latter can be decomposed into three contributions from pixel size (σ_{pix}), chromatic effects (σ_{chr}) and emission point uncertainty (σ_{emi}):

$$\sigma_{1pe}^2 = \sigma_{pix}^2 + \sigma_{chr}^2 + \sigma_{emi}^2. \tag{5.4}$$

To take into account possible spurious contributions, the results in the right plot of 5.9 has been fitted with the function

$$\sigma_\theta = \sigma_0 + \frac{\sigma_{1pe}}{\sqrt{N_{pe}}}. \tag{5.5}$$

The fit gives a constant term compatible with zero and a single photon resolution $\sigma_{1pe} = 5.90 \pm 0.03$ mrad.

Identified pions correspond to those events with an angle within $\pm 3\sigma$ around the mean value, with the σ given by the fit in the right plot of 5.9. The pion detection efficiency, calculated as the ratio between the number of identified pions and the number of events with a gas Cherenkov counter signal above threshold, results $\epsilon(\pi) = 98.4 \pm 0.1\%$. No beam energy dependence has been found.

Kaon Reconstruction

Events below the gas Cherenkov counter threshold include both kaons and antiprotons. 5.10 compares the Cherenkov angle distributions measured for these events (red histograms) with the distributions for pions (blue histograms) at the three beam energies $P = 6, 7, 8$ GeV/c, from left to right. The red histograms are scaled by the relative beam intensities (see Sect. 5.1.1). The prominent kaon peak is separated from the pion one and, at

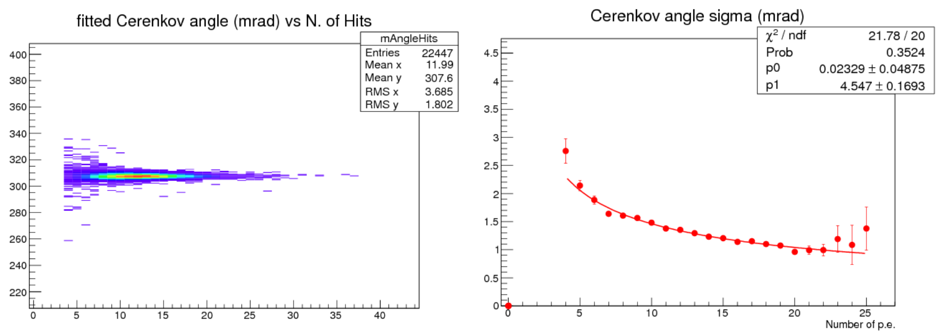

Figure 5.9: Data with $n = 1.05$ and $t = 2$ cm aerogel. Left plot: Cherenkov angle versus the number N_{pe} of photoelectrons. Right plot: gaussian width of the Cherenkov angle distribution as a function of N_{pe}.

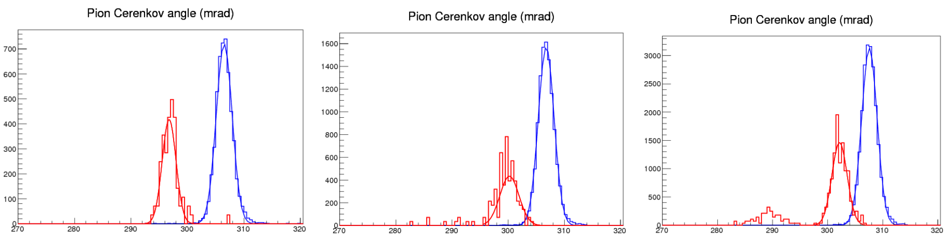

Figure 5.10: Pion Cherenkov angle distributions (in mrad, blue histograms) compared with those from events with gas Cherenkov signal below threshold (red histograms), for $P = 6, 7, 8$ GeV/c beam (from left to right).

the highest energy, some tail of the $\bar{p}$ peak, which disappears as the energy decreases because it goes out of the MAPMTs radial coverage, is also visible. In Tab. 5.1, the mean and width of the gaussian fits of the pion and kaon angles are reported. The number of σ_θ separation between kaon ($R(K)$) and pion ($R(\pi)$) Cherenkov angles as:

$$n_\sigma = \frac{\theta_C(\pi) - \theta_C(K)}{[\sigma_\theta(\pi) + \sigma_\theta(K)]/2}. \tag{5.6}$$

In order to avoid the large fluctuations in the value of $\sigma_\theta(K)$ due to the small kaon statistics, here $\sigma_\theta(K) = \sigma_\theta(\pi)$ is assumed. The obtained values are listed in the last column of Tab. 5.1. Up to the highest momentum, thesepration is always $n_\sigma > 3$.

P (GeV/c)	$\theta_C(\pi)$ (mrad)	$\sigma_\theta(\pi)$ (mrad)	$\theta_C(K)$ (mrad)	$\sigma_\theta(K)$ (mrad)	n_σ
6	333.47±0.03	1.81±0.02	322.13±0.04	1.56±0.04	6.3
7	333.79±0.02	1.79±0.02	325.79±0.05	2.50±0.05	4.4
8	334.80±0.01	1.80±0.01	328.41±0.02	1.72±0.02	3.5

Table 5.1: Gaussian mean and width of pion and kaon Cherenkov angles and number of σ separation, the latter computed assuming $\sigma_\theta(K) = \sigma_\theta(\pi)$.

5.1.5 Reflected light measurements

Though similar in the concept, this configuration is not the same as for the CLAS12 RICH. In fact, the gap lenght is much smaller (about 1.3 m vs 3 m) and geometry constraints prevent to put the MAPMTs on the focal plane of the mirrors. In addition, the relative alignment of the mirror system with the prototype box was checked only at a few mm level and a relative alignment of the various elements was studied off-line using Monte Carlo simulations. As a consequence, a worse ring reconstruction resolution than in the CLAS12 RICH was expected. Nevertheless, the prototype results can be used to validate the reflected light concept and to tune the CLAS12 RICH Monte Carlo simulations.

The nominal configuration foresees a beam momentum of 6 GeV/c and an aerogel radiator with refractive index $n = 1.05$ and thickness $t = 6$ cm. Data were recorded with and without $n = 1.05$ and $t = 2$ cm aerogel absorbers in front of the planar mirrors.

Because of the difficulty in estimating the total photon path length after the mirror reflections, the results were analyzed in terms of ring radius instaed of Cherenkov angle.

5.11 shows the number of hits per event with and without the absorbers. The detected photons are 13.1 without absorber and 5.3 with absorber, with a yield loss of about 60%.

The ring radius reconstrution for the two measurements is compared in 5.12. The left plot compares the radius distribution measured with and without absorbers, indicating a worsening of the resolution from $\sigma_R = 2.67 \pm 0.01$ mm without to $\sigma_R = 3.79 \pm 0.02$ mm with the absorbers. This is largely due to the decrease in the number N_{pe} of photoelectrons. The right plot shows the esolution as a function of the number N_{pe} of photoelectrons. While without absorbers there are events up to $N_{pe} = 20$, with the absorbers the maximum value with significant statistics is $N_{pe} = 11$. Nevertheless, the fitted single photon resolution does not change significantly, since a value of $\sigma^R_{1pe} = 9.55 \pm 0.04$ mm and $\sigma^R_{1pe} = 9.25 \pm 0.04$ mm is obtained without and

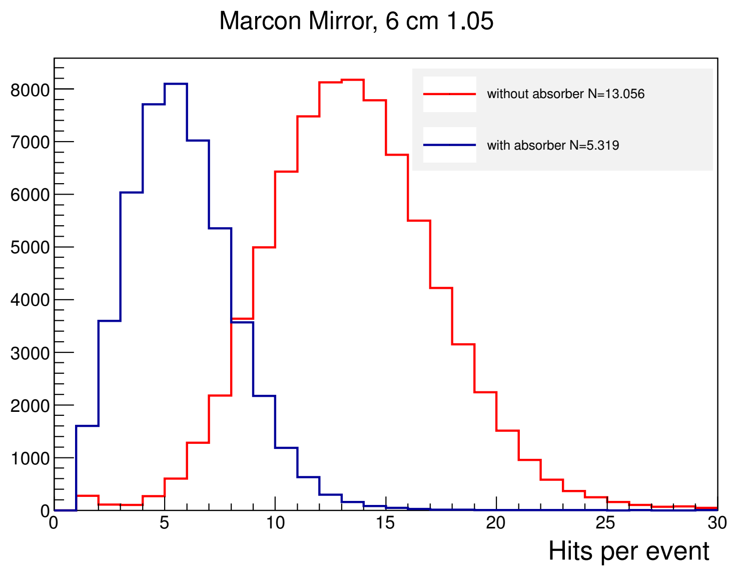

Figure 5.11: Number of hits per event for data without the aerogel absorber (red histogram) and with the 2cm aerogel absorbers placed in front of the planar mirrors (blue histogram).

with the absorbers, respectively. This important result indicate that there is no significant degradation of the Cherenkov angle resolution in the reflected light case, in addition to the expected photon yield loss.

5.1.6 Summary of the test results

The test-beam measurements have proven the working principles of the CLAS12 RICH and the prototype data have also indicated the improvements that can be reached in the final detector.

In the prototype, 14 H8500 with normal glass and 14 with UV-enhanced glass were used. The latter ones provide on average one additional photo-electron, but they also have a worse resolution. The single photon resolution measured with normal glass MAPMTs is in fact about 30% better than for UV-enhanced MAPMTs and about 15% better than the one measured with all the 28 MAPMTs. A corresponding improvement in the pion/kaon separation using only normal glass MAPMTs is expected.

Another improvement is the better ring coverage (close to the limit given by the H8500 packing fraction of 89%) anticipated in the final RICH. In the prototype, the coverage was worse by an factor of $15 - 25\%$. With a cut $N_{pe} > 7$, a gain in resolution of about 7% was obtained with a loss of

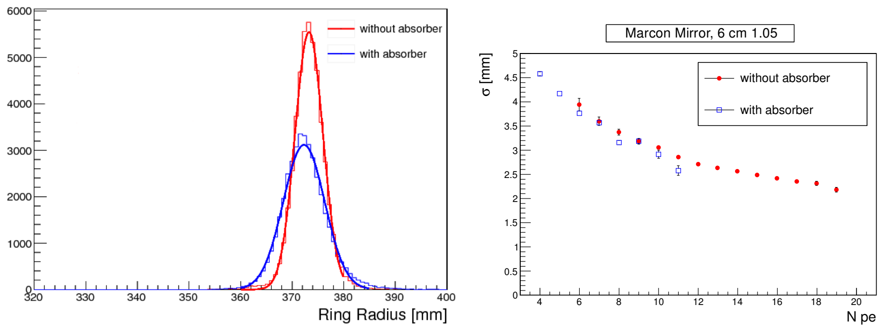

Figure 5.12: Left plot: ring radius distributions without (red histogram) and with (blue histogram) the aerogel absorber. Right plot: gaussian width of the ring radius as a function of the number of *p.e.* for runs without (black circles) and with (red circles) the aerogel absorbers.

events of only 10%. Therefore, in the CLAS12 RICH, the events with a smaller number of Cherenkov hits can be rejected, improving the resolution but without decreasing too much the efficiency. For the reflected light case, the longer photon path length will help in the separation of the Cherenkov pion and kaon rings provided that the 1 ns time resolution will be matced.

In particular, the beam-test campain provided the validation of MAROC as front-end signal processing circuit for MAPMT working at single photon level.

5.2 Radiation damage

The electronics instrumentation can occasionally manifest malfunctioning due to the passage of particles through its analog and digital circuits. A wide range of effects is documented in literature and all of them can be ultimately attributed to alterations in the electrical conductivity between nodes. Depending on the permanent or temporary character of these alterations, the functioning of a device exposed to radiation can be totally compromised or still be acceptable, but with reduced reliability. For high energy physics is therefore necessary to test the equipment to guarantee an adequate tolerance compared to the working environment and eventually implements mitigation strategies at all levels, hardware, firmware and software.

Using CLAS12 simulation tools, the operating condition of the RICH were estimated as a function of the polar angle and energy. From this data the number of particles per unit area integrated in a given time interval (fluence) investing the electronics has been calculated for gammas and neutrons. For example, considering energies in the range from 0.1 to 1MeV, the expected annual neutron fluence on the electronics panel reaches 10^{10} cm^{-2} at full luminosity and 100% duty cycle. Such a level is moderate compared with other facilities like Belle-II and LHCb-2 where the radiation is two order of magnitude higher [31, 32], but is still much higher than ordinary laboratory test conditions. Therefore a test campaign has been organized to reproduce the stress condition on the RICH electronics.

Since the MAROC front-end ASIC was designed in 0.35μm BiCMOS technology (AMS) for the ATLAS luminometer, no permanent damage is foreseen for it at this levels. On the other hand its configuration register can experience alterations that, if not detected, can led to data quality deterioration [2]. For this reason an estimation of the MAROC soft error probability would help in data quality optimization.

Different is the situation for the commercial grade Artix-7 FPGA device that does not have neither a specific radiation tolerant design nor a documented reliability in irradiated environment. Based on the results of similar product from the same manufacturer, Virtex and Kintex families [31, 33], it is reasonable to expect some level of logic error susceptibility in both configuration and user memory. For this component, it would be good to have an estimation of operational availability, to schedule periodical maintenance and eventually prepare counter measurements against data corruption. Also an on-field verification of the non-volatile memory stability would provide important indications for the cabling of the RICH resources, being the optical fiber the baseline solution and having the JTAG port (that would require the routing of an addition cable) as a possible recovery option.

If many studies in high energy physics and other fields exist for FPGA components, no specific documentation has been found about the small form factor optical transceiver adopted in the RICH electronics implementation. As this component plays an essential role in the readout communication, being the data link between the controller and the front-end tile, a test of its tolerance is of primary importance.

In principle a complete radiation validation of a device requires systematic test with all types of ionizing particles, but in practice this is very time and money consuming. We limited the study to neutrons and gammas because they they exhibit by far the largest fluence and therefore provide enough indication for the operation in CLAS12. In both cases, the radiation intensity was chosen to integrate a minimum of ten year equivalent exposition at

[2] private communication with the MAROC designer Christoff de la Taille, during the PSHP 14 Conference.

CLAS12 in a shorter period of time, then the devices were stressed longer to investigate their performance limit.

The section is organized as follows: first the data acquisition setup is presented, then results at the two beam testing facility are described, finally the implication for the RICH electronics during the experiment life cycle are discussed.

5.2.1 Setup and Methods

Tests consist in alternating an irradiation with a registers check or a periodical monitoring while the bombardment is running. The primary goals are twofold: measure the stability of the digital information written on the irradiated board (soft error immunity), whether containing configuration or event data, and assess the tolerance of the entire unit.

The test tile is provided with power supply and optical fiber cabling in order to keep it running during the irradiations and have the chance to detect memory alteration or functioning interruption. Placed in an adjacent room not exposed to radiation, the data acquisition computer stores a reference copy of all the registers (master copies) and operates consistency checks when it receives instructions from the control room workstation. A separate acquisition system, provided by the irradiation facility, monitors the particle flux and manages the safety interlock system.

As an example, 5.13 shows the neutron source and the tile positioning operation before starting the test.

A special firmware version has been used to enhance the soft error sensitivity by adding two large test memories to the standard RICH firmware. The RICH logic and buffering occupy only about 25% of the FPGA resources, so this addition allows to collect statistics from a larger number of cells and determine the error immunity performance with a higher precision at a given exposure time. A summary of all the types of memory used is presented in table 5.2. Each of them can be independently accessed thanks to a dedicated function library. SPI refers to the not-valatile memeory EEPROM, the acronym stands for Serial Peripheral Interface (SPI), the communication protocol between FPGA and EEPROM devices. BRAM and REG are two kinds of memory resources inside the FPGA, the first consists in large blocks used mostly for data buffering, the seconds is small and distributed to be used for logic or small registers.

The sequence of operations can be described as follows. At power cycle all the memories are initialized with a master image. During or after the irradiation the content of the memories in table 5.2 is readout and compared with the corresponding master image. Data are saved on a plain text file

Figure 5.13: Installation at Frascati Neutron Generator facility (FNG)

Memory	Size [kbit]	Usage
SPI	512000	Firmware image
BRAM	2000	Test for event data
REG	32	Test for I/O register
MAROC	2	Front end parameters

Table 5.2: Memory buffers for rad testing. The SPI refers to the EEPROM device, BRAM and REG are implemented into the FPGA to enhance the error sensitivity compared to the standard use of resources of the RICH logic.

on the acquisition PC and the number of errors is printed on screen for a real time control by the user. Files are identified with a timestamp to avoid overwriting and allow later reconstruction and correlations.

In addition to this basic, custom made, failure check test, a more sophisticated instrument is provided by the manufacturer (Xilinx [34]) to test directly the FPGA configuration memory. The module is called Soft Error Mitigation (SEM) and consists in a finite state machine (called *scrubber*) that scans the parity bits of the memory blocks looking for inconsistencies and attempting to repair the damaged portions. The SEM provides a deeper look at the functional alteration and it is complementary to our observations. Its error counting statistics can be accessed using dedicated registers that are again not part of the RICH standard firmware. There are special cases where the bitstream repairing operation is not possible, for example when multiple alterations leave unaltered the parity bits or when an initial error propagates creating multiple issues that the scrubber is not able to manage. In these cases the SEM finite state machine goes to idle state and a reset is necessary to restart the operations. As this eventuality was not known at the moment of the tests, in a couple of occasions some error statistics was lost, roughly one over 50 hours in case of neutrons (2%).

5.2.2 Neutron Test

The Frascati Neutron Generator facility (FNG) provides a point like isotropic source of 14 MeV/c mono-energetic neutrons exploiting the $d + {}^3\mathrm{H} \rightarrow \alpha + \mathrm{n}$ reaction, i.e. from the nuclear fusion of tritium and deuterium into *alpha* and neutron. The number of neutrons produced per unit of time can be monitored by an α particle solid state detector in the cavern and adjusted from the control room. The comparison with CLAS12 conditions is done in two steps. First the CLAS12 and FNG neutron fluxes are convoluted with the damage function of Si to obtain the equivalent number of 1 MeV neutrons ($\mathrm{n_{eq}}$) as described in the standard E722 by ASTM [35]. This gives the equivalent number of 1 MeV neutrons per unit time that create the same damage in Si components and allows comparison between different experimental situations. Then the distance separating the sample and the source is used to calculate the actual fluence investing the tile. A separation of 10 cm was chosen considering that the maximum intensity provided at FNG is 10^{10} neutrons. The CLAS12 equivalent time is calculated considering a flux of 250 neutrons $\mathrm{cm^{-1}s^{-1}}$.

Figure 5.17 shows a monitor plot in which the flux of α particles is plotted as a function of the time (in hours) for the three days of testing (in blue). The detected errors from the BRAM memory are superimposed (in red). The verticals lines represent power cycle events, i.e. counter reset. The beam intensity was slowly ramped up during the first day of operation for a corresponding neutron flux never exceeding $2 \times 10^9\ \mathrm{n_{eq}/s}$ or an equivalent CLAS12 time of 1 year at full luminosity. During the second day the electronics were exposed to higher fluxes causing more frequent functional errors and consequent reconfiguration through power cycles. At the end of the second day a high intensity flux was used to stress the sample. This last irradiation corresponds to 12 years of equivalent time in CLAS12. On day 3 moderate fluxes were used again to collect systematic data and a final extremely high neutron flux was used, increasing the beam intensity and positioning the sample at a distance of 4 centimeters from the source, thus gaining a factor 36 in comparison with the previous flux condition. In total 65 CLAS12 equivalents

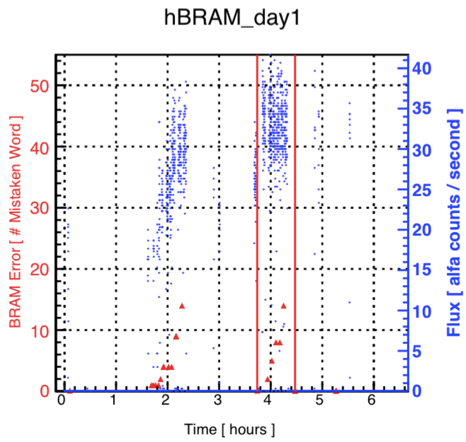

Figure 5.14: Day 1 irradiation history.

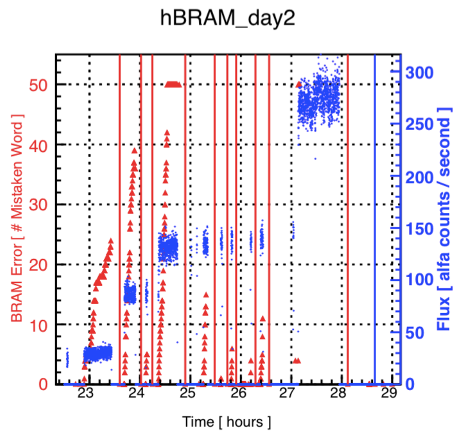

Figure 5.15: Day 2 irradiation history.

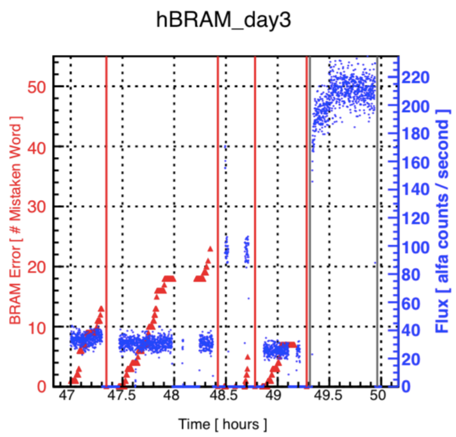

Figure 5.16: Day 3 irradiation history.

Figure 5.17: Neutron Irradiation Test. Beam intensity (in red) and BRAM error occurrences (in blue). Red vertical lines indicate reset operations (power cycles). The end-of-the-day high flux irradiation of day 2 and 3 were not error monitored.

years have been reproduced and data were online monitored for 23 of them. During the unmonitored irradiation of the last day, i.e. after 23 equivalent years in CLAS12, the optical transceiver was permanently damaged and had to be replaced before executing the diagnostic on EEPROM.

No error has been observed in the EEPROM memory during the whole test and after. No error has been observed in the MAROC configuration register. The total number of errors observed by the SEM controller was 185. Among these, 175 (94.6%) were classified as correctable and only 10 (5.4%) as uncorrectable. A similar number of errors (about 200) have been detected summing all the errors on BRAM and REG memories.

In total 18 communication protocol failures were observed during the whole test due to configuration memory alteration in the portion of the FPGA that manage the TCP/IP protocol.

The BRAM memory will be used for RICH data buffering and its errors have been carefully studied. Three regimes of neutron fluxes were used to study the dependence of the error probability on the beam intensity. The obtained trend is reported in 5.18. From this data no evident correlation with the flux appears and the calculated average error probability is less than 10^{-8} errors/n_{eq} for the three regimes considered. In terms of CLAS12, this means an error every 6.6 weeks per electronic tile. The absence of correlation with the flux is probably due to the poor statistics collected or simply because the dependence would become evident only by spanning different orders of magnitude. The regime between 4 and 10 millions neutrons $cm^{-2}s^{-1}$ were investigated on resident configuration data. For real events this number has to be scaled for the latency of the trigger.

5.2.3 Gamma Test

A gamma irradiation test has been performed at Istituto Superiore di Sanità (Italian National Institute of Health) in Rome with a ^{137}Cs source. Figure 5.19 shows a picture of the irradiation machine. A bench module power supply and a PC with optical Ethernet link completed the setup.

The gamma source provides a uniform irradiation over the sample with a very high dose rate compared to CLAS12. The minimum possible flux allows to reproduce one year equivalent time in just 60 seconds (4.4×10^{10} photons). For this reason short irradiations were performed at the beginning, until the estimated 10 years equivalent dose of CLAS12, corresponding to 137 Rad, was reached. Because no error or malfunctioning had been observed during this period, the sample was irradiated for many hours up to a dose of 50 kRad. The registers and flash memory did not reported any soft error during this period and only one configuration memory error were detected by the SEM

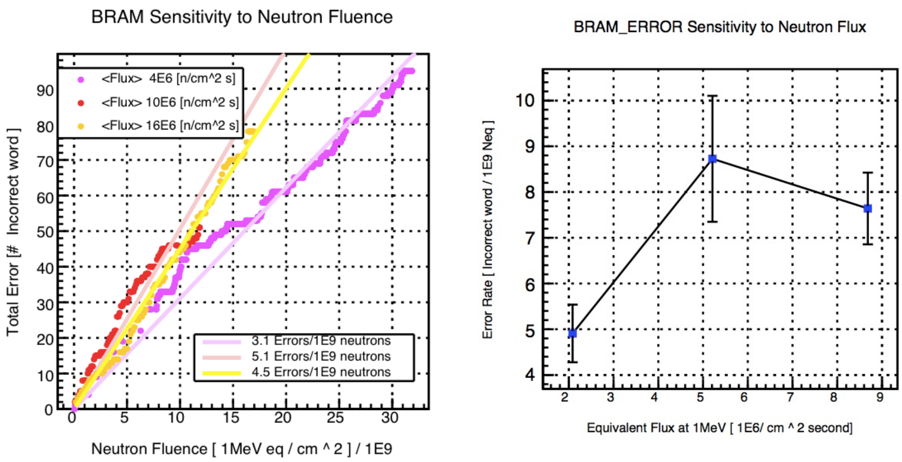

Figure 5.18: Small error probability, independent from the beam intensity

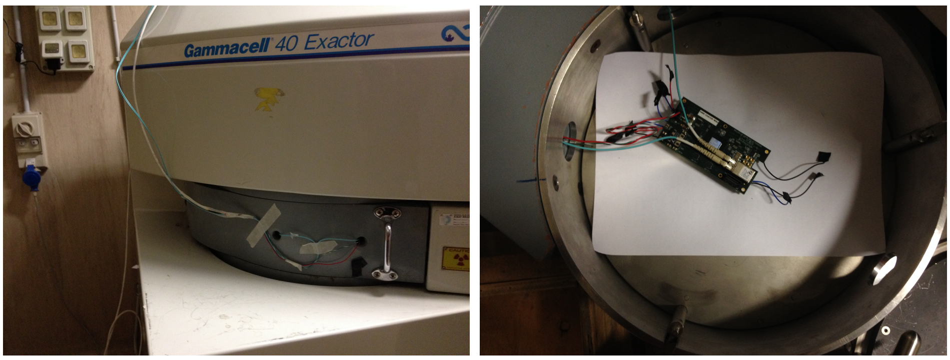

Figure 5.19: ^{137}Cs Irradiation facility. Cables entering the irradiated volume for providing data link

controller around 40 kRad.

Voltages and temperature were monitored, as well as the other registers, every 5 minutes as shown in 5.20. They started to drift at 46 kRad, (logbook entry 410), then the connection with the board was lost and the last 3 hours of irradiation followed without online checks. The interruption of the SEM controller did not allow to tell if the communication interruption was due to an uncorrectable error or had another origin. Looking at the plots the ADC measurement drift can be explained by a progressive degradation of the 1.8 Voltage regulator that provides the bias for the all the regulators on board. This part was the only one broken during the DC voltage test operated after the deactivation period. In absence of further temperature data it is not possible to conclude if this was due tothe gamma irradiation or to an excess above the temperature limit caused by the absence of a cooling system.

5.2.4 Conclusions

The performed irradiation tests are not a complete qualification of the radiation tolerance of the front-end electronics. Only mono-energetic beams have been used and only two samples have been irradiated: one tile with 14 MeV/c with neutrons, one tile with with 662 keV gamma photons.

However soft errors have been observed in correlation with the integrated fluence, at least for the neutron case, thus an error immunity estimation has been possible for the RICH electronics. In addition to that, none of the programmable devices reported any hardware damage at the expected fluence level of CLAS12 neither for neutrons nor for gammas.

Based on the observed soft error rate, an estimation of the event data corruption is possible. A non zero error probability has been estimated in the neutron case (10^{-8} errors/n_{eq}). To estimate the impact on the RICH data quality, this number has to be multiplied by the total number of tiles (150) and divided by the latency of the trigger ($8\,\mu$s). The latter is the time interval in which the digitized data persist in the memory elements located in the acceptance of the spectrometer, and is thus prone to corruption. Considering that, the number of errors at the expected CLAS12 fluence would be (over 25000 channels), small enough that no redundant logic, i.e. parity bits, appears necessary neither in the firmware nor at software level.

The EEPROM device seems to be built with a very radiation tolerant technology and demonstrated to be adequate to store the firmware image without the need to implement a JTAG recovery option.

The last considerations are about configuration registers. The MAROC chip showed stable performance over the entire period of irradiation. Its

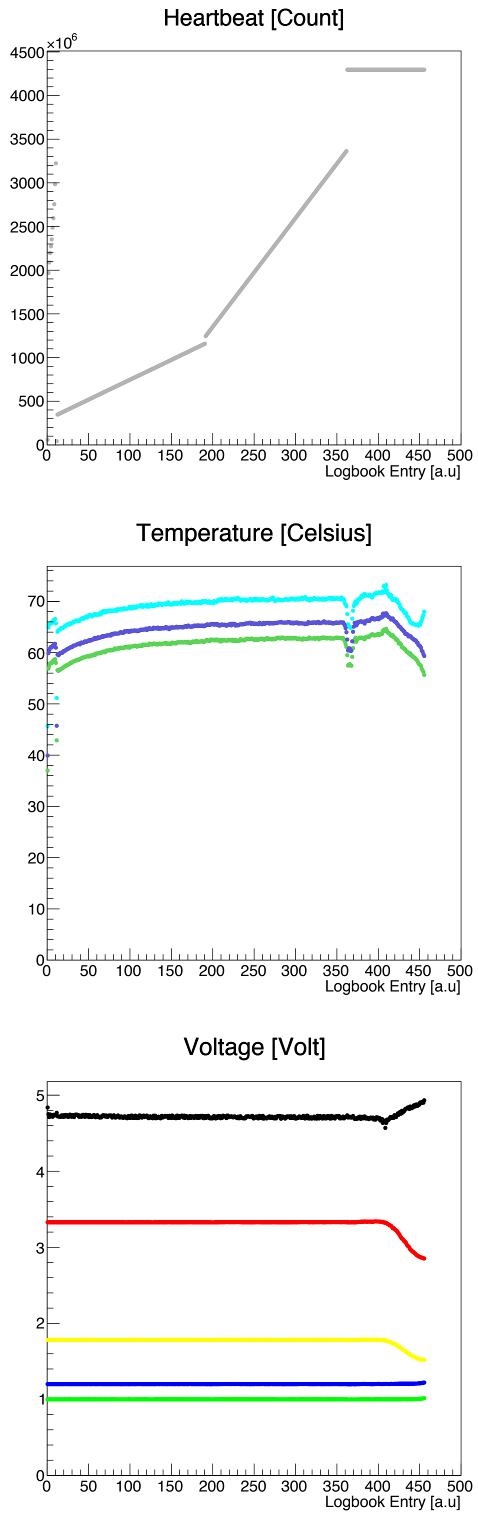

Figure 5.20: Data monitor during gamma irradiation. Soft error mitigation was in idle state since entry 360 when ADC, voltage and temperature values started a drift indicating a progressive reduction of the bias.

reconfiguration is already scheduled at the beginning of each run and periodical checks will ensure the data quality without compromising the detector availability for physics data taking (taking few millisecond every hour) In case of corruption, the FPGA firmware can be restored with a power cycle operation or via optical fiber. As both operations can be done in parallel (i.e. independently) on each tile and take only few millisecond, the system availability can be considered perfectly adequate for CLAS12 operations. As a further element of safety, a second image of the firmware can be stored (compressed) in the EEPROM in case the first get deteriorated.

Finally the SEM self repairing capabilities are very interesting, but cannot be fully trusted because not all the errors can be located and repaired, and because a time interval occurs between bit flip occurrence, its detection, location and correction, so no protection is offered against the propagation of this error.

5.3 Test beam with digital readout

During the spring of 2016, the designed Cherenkov light readout system was tested in real working conditions[36].

5.3.1 Experimental setup

The test was part of the preliminary studies for the realization of a RICH detector for a new facility, an Electron Ion Collider (EIC), dedicated to the progress of the knowledge on Nuclear Physics in the next decades. JLAB is one of the site candidate for the construction of an EIC thanks to the existing expertise in accelerator and detection technologies. With the addition of a new ion source, accelerator and cooler to the JLab electron beam facility, an EIC could be realized at an elevated luminosity, up to 2×10^{34} cm^{-2} s^{-1}, and at a high center-of-mass energy, extended up to 140 GeV/c, with the use of extremely advanced magnets of 12 T field [37]. As part of the *R&D* program, a prototype of an innovative modular RICH detector (*mRICH*) has been designed, constructed and tested using the CLAS12 RICH electronics for the MAPMT readout. The *mRICH* concept is based on a array of compact RICH modules, each with a Fresnel lens to focus the Cherenkov ring on the detector plane positioned at a short distance (corresponding to the 10-20 cm lens focal length) from the aerogel radiator.

The test has been conducted at Fermilab using a 120 GeV/c proton beam to exploit its narrow profile and avoid the implementation of a tracking system. The photon detection surface, composed by 4 H8500 MAPMTs, is shown in 5.21 together with the two readout tiles (for a total of 256 channels). For this test no readout controller was used and the two FPGA boards were readout independently using a dual-head optical Ethernet card on a standard PC. The reconstruction of the events has been done offline using the time stamp for data alignment of the two boards. The patch panel of the mRICH prototype has been realized accordingly to the specifications of the CLAS12 RICH readout electronics with LC optical fiber, SHV and low voltage connectors as shown in 5.22.

5.3.2 Result and Conclusions

The test lasted for few days and provided the chance to validate the RICH binary readout with real Cherenkov photons. 5.23 shows a typical accumulated event display monitor representing the occupancy (detected hits) along the MAPMT surface. The proton beam was incident in the bottom-left quadrant, where the corresponding hit accumulation is due to the ionization in the photocathode glass window when the charged particles traverse the photon detection surface. The Cherenkov ring is clearly visible at the center thanks to the Fresnel lens imaging.

Because of the 6 mm pixalization provided by the available H8500 MAPMT, larger than the *mRICH* design value of 3 mm, no hadron identification was attempted. Nevertheless it was possible to compare the ring position and size and the number of detected photons on the ring with the simulations, finding a close agreement with [8]. Together with a first validation of the *mRICH* concept, the test proven the single-photon detection capability of the CLAS12 RICH readout electronics in conjunction with the H8500 MAPMTs. This was an important milestone since the online discrimination of single-photon signals is not a trivial task.

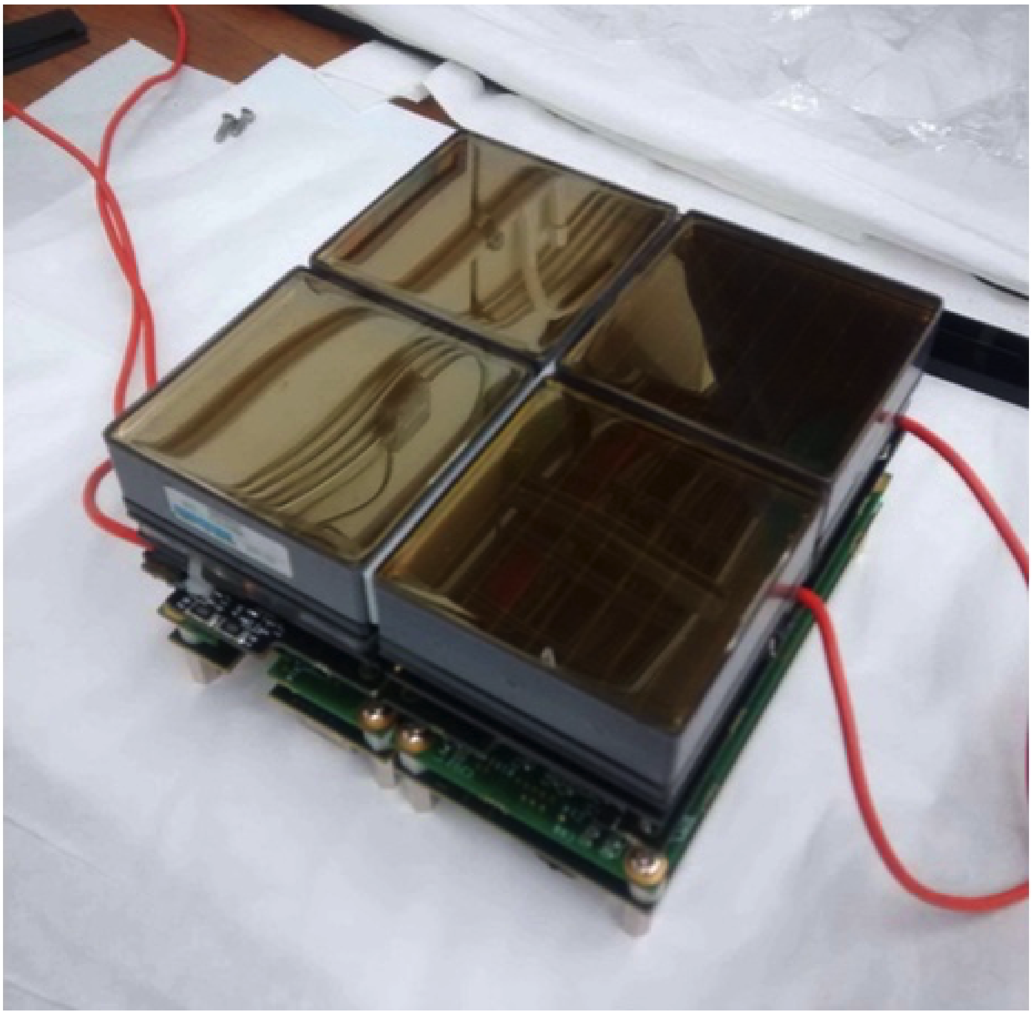

Figure 5.21: The *mRICH* prototype photon detection surface composed by 4 H8500 MAPMTs mounted on 2 side by side electronic tiles (256 pixels).

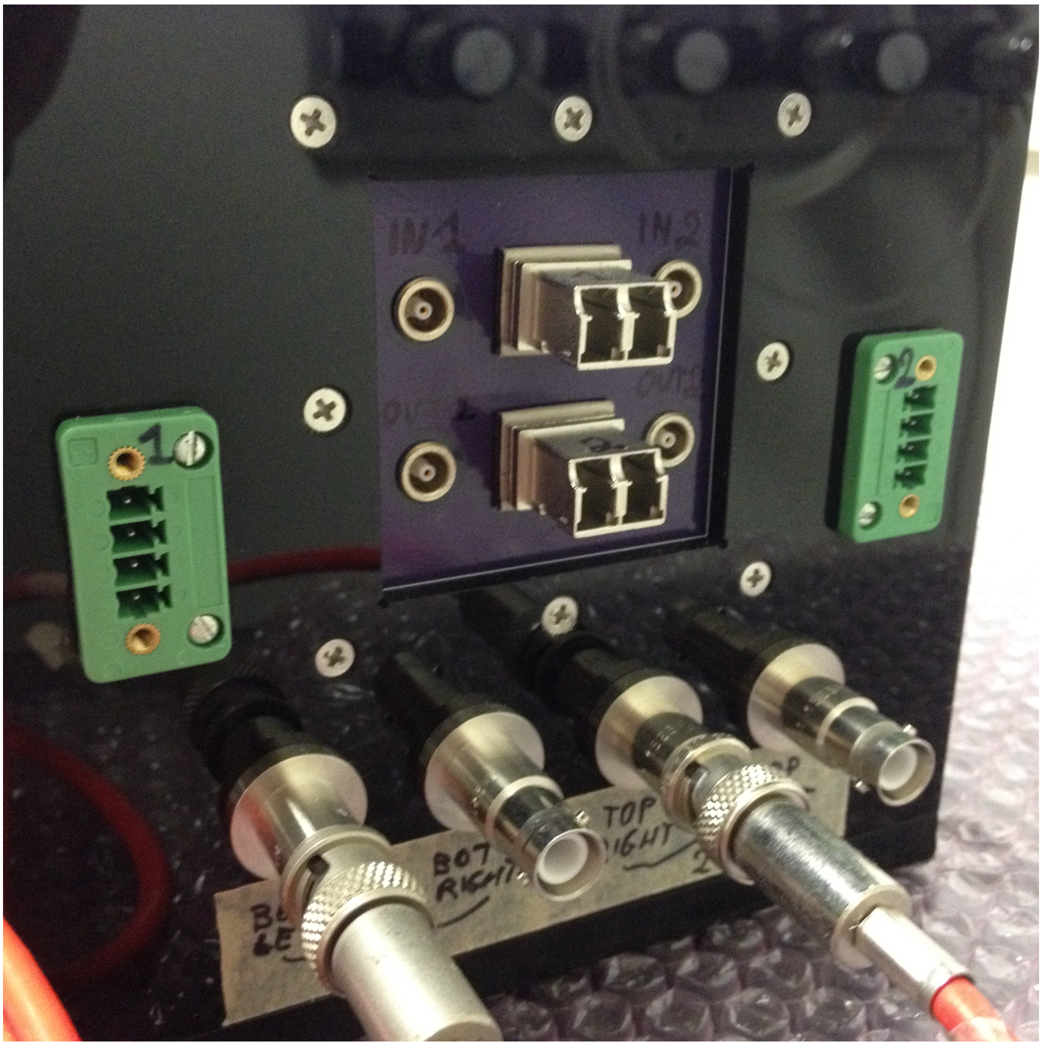

Figure 5.22: Detail view of the patch panel of the *mRICH* prototype. Two FPGA boards were connected independently to the data acquisition PC using optical fiber links and four LEMO cables were used for additional I/O resources, i.e. distributing the trigger (violet panel). Two of the four available SHV connectors were used to feed the 4 H8500 MAPMTs inside the box via the 2 ADAPTER boards. Green connectors were used for LV distribution.

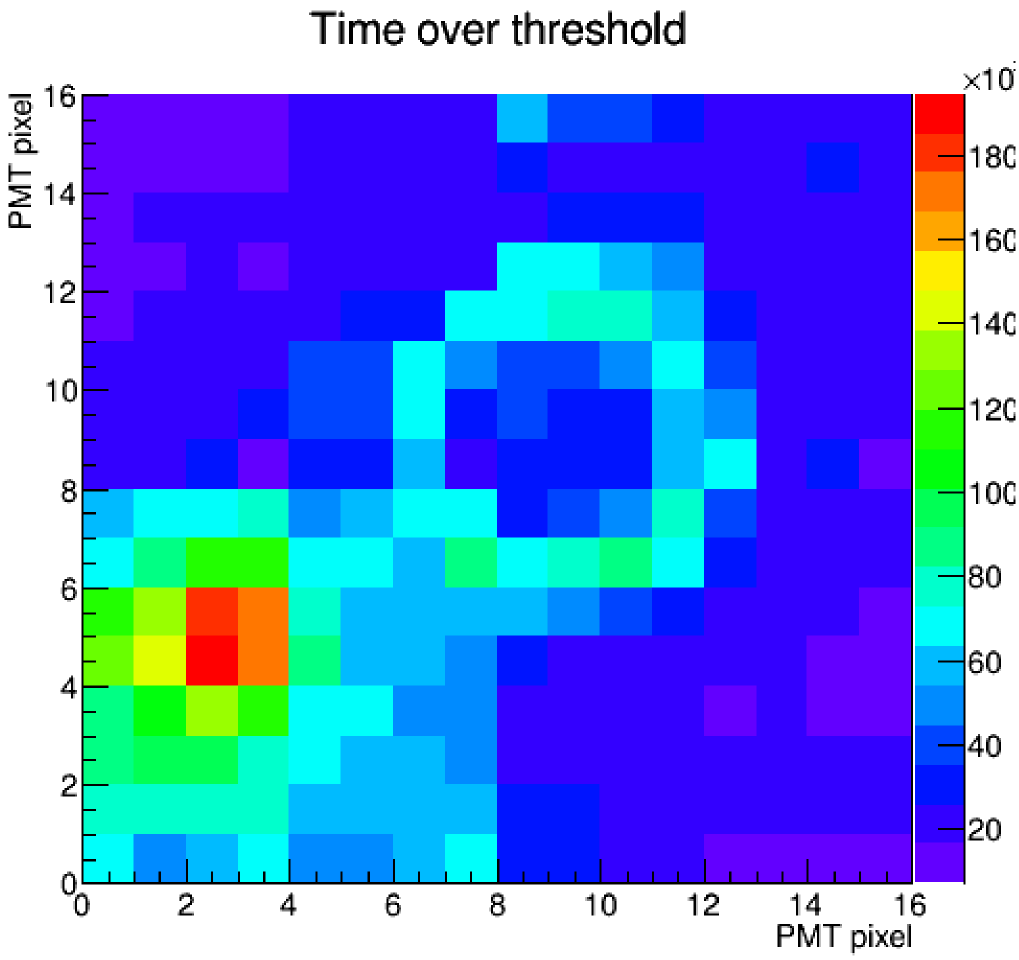

Figure 5.23: Test Beam accumulated event display. The data taking was operated in the same conditions foreseen at CLAS12, namely with an asynchronous external trigger source and only the TDC digital output recorded. The Cherenkov ring, clearly visible at the center of the image, was obtained from a 120 GeV/c protons beam traversing a 1.03 refractive index aerogel tile in the bottom-left quadrant. A Fresnel lens focused the Cherenkov ring at the center of the detection surface composed by 4 Hamamatsu H8500. The MAPMT were mounted on two RICH electronic tiles for a total of 256 readout pixels.

Chapter 6

Conclusion

The design and the development of the readout electronics for the new RICH module of CLAS12 spectrometer has been presented together with the fully qualifying tests conducted by the candidate for the prototypes validation. A large set of tests results, with different setups, demonstrated that the proposed solution satisfies the project requirements with remarkable flexibility.

As an outcome of the positive results obtained the mass production of the front end boards took place during the finalization of this document. Soon 160 new tiles will be ready to be characterized with the tools and protocols created and tuned up by the author and here described. They will be assembled, together with the other detector's components, during the spring of 2017 in a clean room at JLab.

In the next months the functionalities developed during the prototype testing will be extended to the entire electronic panel. The procedures will be systematized and further automatized to be able to control and monitor the large number of channels in a timely manner. The migration of the software tools into the CLAS12 environment will be completed for the final commissioning of the detector. Cosmic rays will be used for an extensive commissioning phase towards the RICH detector installation planned in September 2017.

In this conclusive chapter a summary of the main results is presented together with a possible set of improvements. Finally, a list of adaptations to other experimental conditions, possible with minimal modifications, is proposed to advertise potential applications of the thesis work and to highlight the multipurpose features of the design.

6.1 Results

A readout electronics for the new RICH detector module of the CLAS12 experiment at JLab has been designed to fit into the spectrometer baseline with minimum impact. The use of the MAROC chip for the MAPMTs readout, combined with in situ programmable logic, is an effective solution for having high specialization and flexibility at the same time. With such an electronics, the RICH can be operated with a high level of automation in combination with the other detectors or autonomously from the rest of the apparatus. In particular, dedicated calibration run modes would allow to calibrate and monitor the photosensor response and compensate any potential aging. In addition, the modular approach and the compactness of the detection unit make this readout potentially interesting for other applications. Relevant features are the complete in-situ data digitization that, combined with the low multiplicity of the Cherenkov photons, will allow substantially dead-time free acquisition at the expected event rate of CLAS12 operations and the available multiplexed charge measurement useful for calibration porpouses.

Numerous tests have been done to verify that the system fulfills the expected performance. An high resolution pulse height spectrum, a sensitivity down to extremely small fraction of the typical photoelectron signal and a time resolution adequate to separate direct and reflected photons have been proven by using both the on board adjustable amplitude test pulse and real photosensors. Many different procedures have been proposed to chose the optimum workpoint and ensure high uniformity in the performance of the whole photodetection surface. In addition, the tolerance of the front-end unit to the CLAS12 radiation environment has been proven in specific test with neutron and gamma irradiation. The tests validated the stand alone components and demonstrated an almost null probability of volatile memory corruption. The inaccessibility of the equipment and the thermal constraints during data-taking have been analised and solved minimizing the power consumption of all the components.

TDC The TDC readout system acquires both leading and trailing edge polarities and proved to be perfectly adequate for the binary readout. The 1 ns resolution, required to separate direct from reflected photon hits, can be obtained in the whole dynamic range of H8500 single-photon signals by a proper offline walk correction of the discriminating time. The discrimination efficiency is excellent down to few tens of fC or, correspndingly, to less than 10% of the average single-photon signal provided by the RICH photosensors.

ADC High resolution pulse amplitude spectra allow an effective monitoring of the MAPMT performance and provide at the same time the necessary information for pixel gain equalization. Monitoring and calibration runs can use either calibrated pulses from the on board injector in internal triggering mode or MAPMT dark-count events in self-triggering mode.

PCB layout Accounting for the constraints given by the electronic panel assembling and the MAROC package dimensions, the PCB layout has been optimized to minimize the feedback and mutual induction among digital outputs and analog inputs.

Power dissipation The heat generated by tiles array (less than 4 Watts per unit) can be easily removed with a simple air conditioning system of 100 liters per minutes.

Tolerance to radiation Given the moderate irradiation environment of CLAS12 at the electronic panel position, specific tests qualified the hardware components for the use during all the life time of the experiment, that the data corruption probability is small and that the necessary reconfiguration are fully compatible with machine operations with a system availability close to 100%

Software Tools A complete library of methods to configure, readout, calibrate, slow-control monitor and analyze the analog and digital MAROC outputs have been developed. The software has been organized in a modular way and integrated with an automatic logbooking and easy control parameter selection. The tools are ready for the CLAS12 integration. The majority of the modules will be reused during detector commissioning and stand alone testing, while for the migration in the CLAS12 software environment the object oriented approach will payback in the foreseen Java language migration.

6.2 Outlook

In the next months a more systematic strategy for calibrating the 25000 readout channels has to be developed. It should account for the fine tuning of the shaping parameters and allow an effective channel equalization. The full electronic panel should be equiped and commissioned before the first RICH module installation planned for September 2017. Methods will be implemented to exploit in autotrigger mode the background of the experiment, e.g. the photocathode thermal emission and cosmic rays, as a natural source of information.

6.2.1 Potential improvements

A second RICH sector is planned to create a symmetric setup for spin asymmetry study with a transversely polarized target in two years from now.

Detailed studies performed at single photoelectron level allowed to acquire a lot of experience in treating small signals and developing solutions for an upgraded readout electronic circuit:

- The addition of few more layers or the use of blind vias could help in suppressing the input circuit coupling for a crosstalk reduction.

- The adoption of the lately available MAROC BGA package, with smaller dimensions, anticipated benefits for the board layout in terms of easy routing and placing of the components and potential upgrades to manage a larger number of channels and cope with higher pixel density.

- A finer step in the hold delay register (now 8 ns) could help in narrowing the calibration parameter distributions by having a more precise estimation of the pulse peak amplitude.

- Timing performances can be improved using different firmware having higher power consumption as counterpart.

6.2.2 Future applications

SiPM readout The second RICH module could be implemented with solid state detector if they become available at a minor cost per unit of surface than MAPMTs. Feasibility study have shown that SiPM can sustain the CLAS12 radiation environment if properly cooled. As the dynamic range provided by the MAROC chip is compatible with the output characteristics of SiPMs, the same electronics can in principle be used.

GlueX DIRC A Detector of Internally Reflected Cherenkov light (DIRC) is under construction for enhance the hadron identification capability of the GLueX experiment in Hall D at JLab. The readout is based on the RICH electronics and MAROC chip.

Electron Ion Collider The instrumentation developed can be successfully used in different experimental condition where single photon measurements capabilities are required together with the construction of large pixellated detection surfaces. The RICH electronics is being used for the detector R&D of innovative hadron identification devices of a future EIC.

Biology and Medical Imaging Contacts exists with JLab groups that perform PET on plants, to study the vegetable nutriment cycles, and ISS groups working on high resolution tomography for clinical and pre-clinical studies. The capability to work in the few photon regime over a large-area at affordable costs has several applications and is the subject of the CLASMED priority project of MIUR Italian Ministry.

Detector *R&D* The RICH electronics will be used to perform feasibility tests of tracking particles passing a scintillating volume, within an INFN Gruppo 5 funded project.

Appendices

Appendix A

Detector services

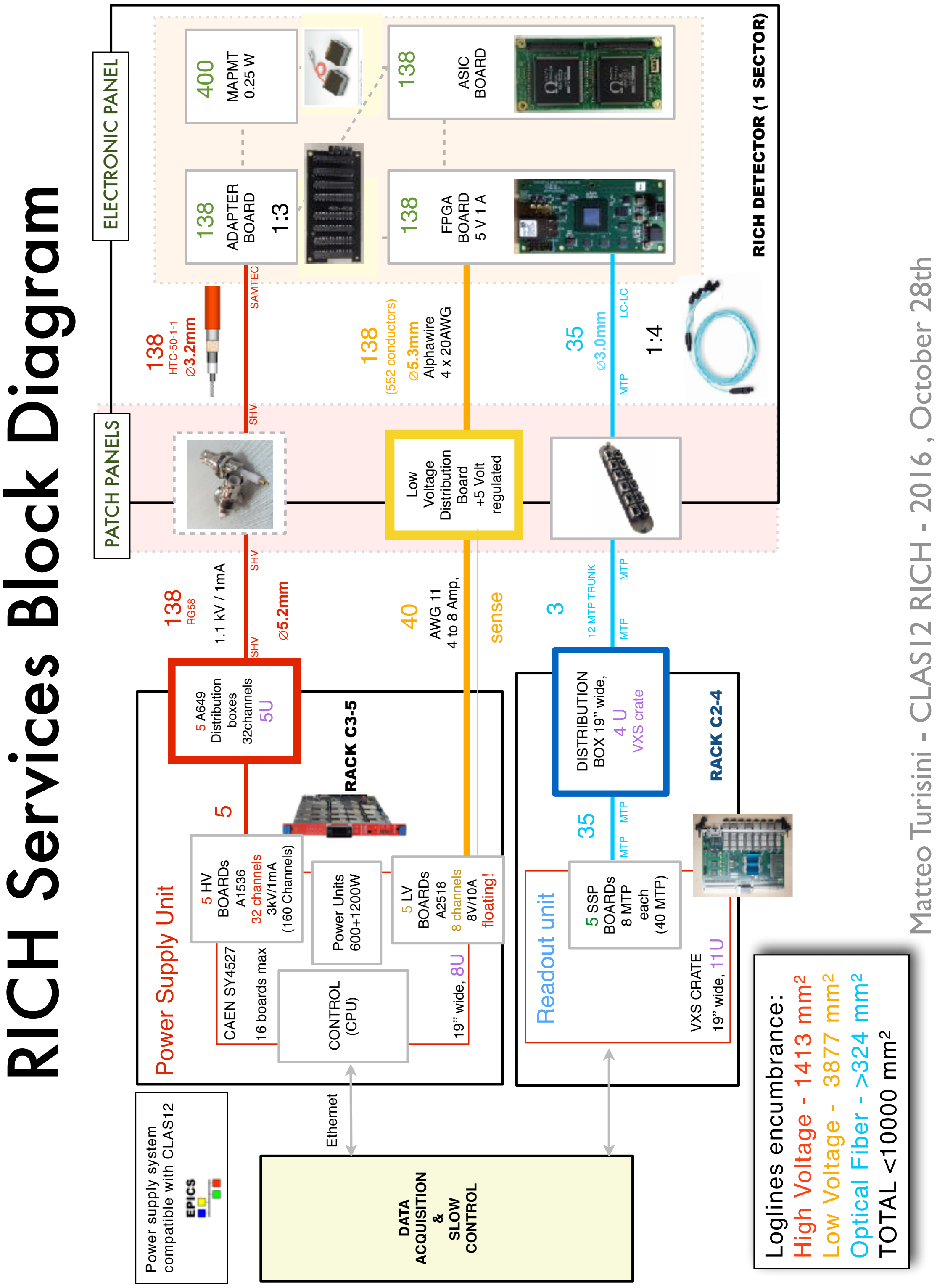

Figure A.1: RICH detector services block scheme

Appendix B

Configuration File

```
run :
{
        name = "tbd";
        address= "192.168.1.10"
        note = "Test␣Bench␣INFN-Ferrara␣(Italy),␣2015␣August␣14th";
        daq_mode = 1; // 0 Scaler, 1 Event, 2 Slow Control 3 Configure only
        source_type = 0; // 0 CTEST enables, 1 anodes
        trigger_source = 0; // 0 internal pulser, 1 autotrigger
        event_preset = 10000;
        time_preset = 20;
        id = 0; // 0 means automatic increment, N means use N as runID
        out = [ 18, 0 ];
        pulser :
        {
                frequency = 1000;
                dutycycle = 0.5;
                repetition = 100;
        };
        ctest_amplitude = 0;
        qmin=0;
        qmax=100;

        slowcontrol :
        {
                enb_scaler = 1;
                enb_voltage = 0;
                enb_temperature = 0;
                repetition = 1;
                time_interval = 1000;
                verbosity = 1;
                savedata = 0;
        };
        tdc :
```

```
        {
                trigger_delay =0;
                evtb_lookback = 110;  // clock ticks units [8 ns]
                evtb_windowwidth = 100;  // clock ticks units [8 ns]
        };
        adc :
        {
                enable_adc = 1; // useless ? to check
                hold_delay = 13; // actually the best hold is taken from external file
                waveform_mode = 0;
                sample_statistics = 10;
                disableCK40 = 0;
        };
        mapmt :
        {
                hv = -1;
                id = ["GA0303","","GA0096"];
        };
        laser :
        {
                w = 5;
                x = 183;
                y = 7;
        };
        maskedOR : // SELF TRIGGER
        {
                opt = 0; //0  single channel; single asic
                asic = 1;
                channel = 3;
        };
        maroc :
        {
                id = [880,587,584];
                pedTDCRMS = [198,200,197];
                pedTDCMean = [10,2,5]; // GAIN DEPENDENT
                Thr = [192,200,197];

                gain_default = 64;
                gain_mode = 0;
                gain_map_file = "../cfg/gain/gain_map";
                thr_default = 250;
                thr_map = 0;
                thr_map_file = "../cfg/thr/thr_map.txt";
                best_hold_file = "./besthold.txt"
                ctest_mode = 1; // 0 = disabled, 1 = single channel (ch_sel), 2 = all chan
                ch_sel = 3;
                ch_probe = 3;
                mask32 = 255L;
                cmd_fsu = 0;
```

```
        cmd_ss = 1;
        cmd_fsb = 1;
        swb_buf_250f = 0; / /RC buffer attenuation, standard 0000
        swb_buf_500f = 0;
        swb_buf_1p = 0;
        swb_buf_2p = 0;
        ONOFF_ss = 1;
        sw_ss_300f = 1; // Slow Shaper Configuration, standard 110
        sw_ss_600f = 1;
        sw_ss_1200f = 0;
        EN_ADC = 1;
        H1H2_choice = 0;
        sw_fsu_20f = 1;
        sw_fsu_40f = 1;
        sw_fsu_25k = 0;
        sw_fsu_50k = 0;
        sw_fsu_100k = 0;
        sw_fsb1_50k = 0; //  Fast Shaper Bipolar, standard 0001
        sw_fsb1_100k = 0;
        sw_fsb1_100f = 0;
        sw_fsb1_50f = 1;
        cmd_fsb_fsu = 0;
        valid_dc_fs = 1;
        sw_fsb2_50k = 0;
        sw_fsb2_100k = 0;
        sw_fsb2_100f = 0;
        sw_fsb2_50f = 1;
        valid_dc_fsb2 = 0;
        ENb_tristate = 1;
        polar_discri = 1; // 0 = active high, 1 = active low
        inv_discriADC = 0;
        d1_d2 = 0;
        cmd_CK_mux = 0;
        ONOFF_otabg = 0;
        ONOFF_dac = 0;
        small_dac = 0;
        enb_outADC = 0;
        inv_startCmptGray = 1;
        ramp_8bit = 0;
        ramp_10bit = 0;
    };
    ana :
    {
        enable = 1; # use 0 for running daq only
        verbosity = 0; // 0 = nothing, 1 only header, 2 all
        tmin = 1; // minimum leading edge time for an hit to be filled in the hit histogra
        tmax = 8191;
    };
};
```

Appendix C

MAROC board schematics

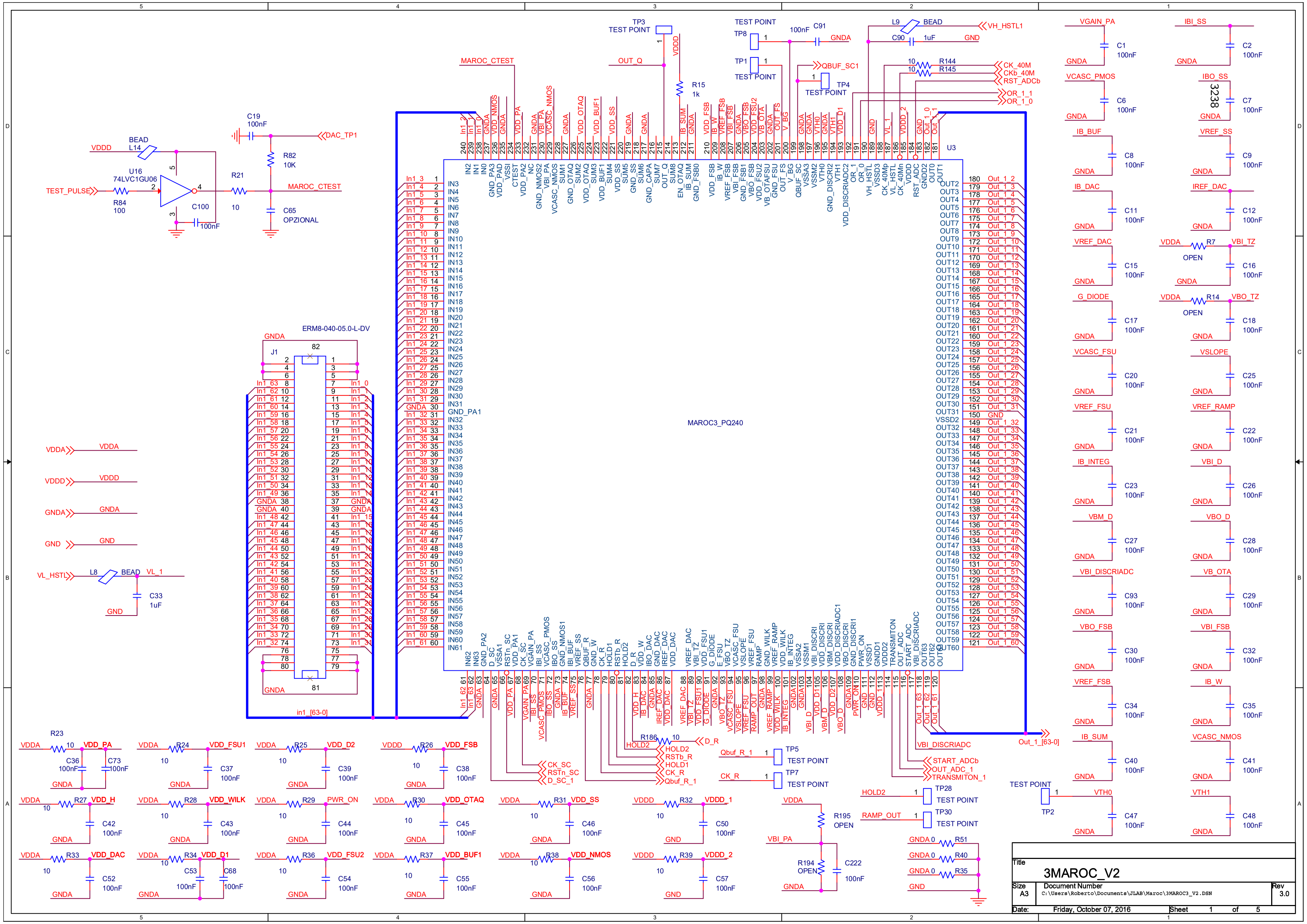
3MAROC_V2
Size A3
Document Number C:\Users\Roberto\Documents\JLAB\Maroc\3MAROC3_V2.DSN
Rev 3.0
Date: Friday, October 07, 2016
Sheet 1 of 5
MAROC3_PQ240
ERM8-040-05.0-L-DV

3239

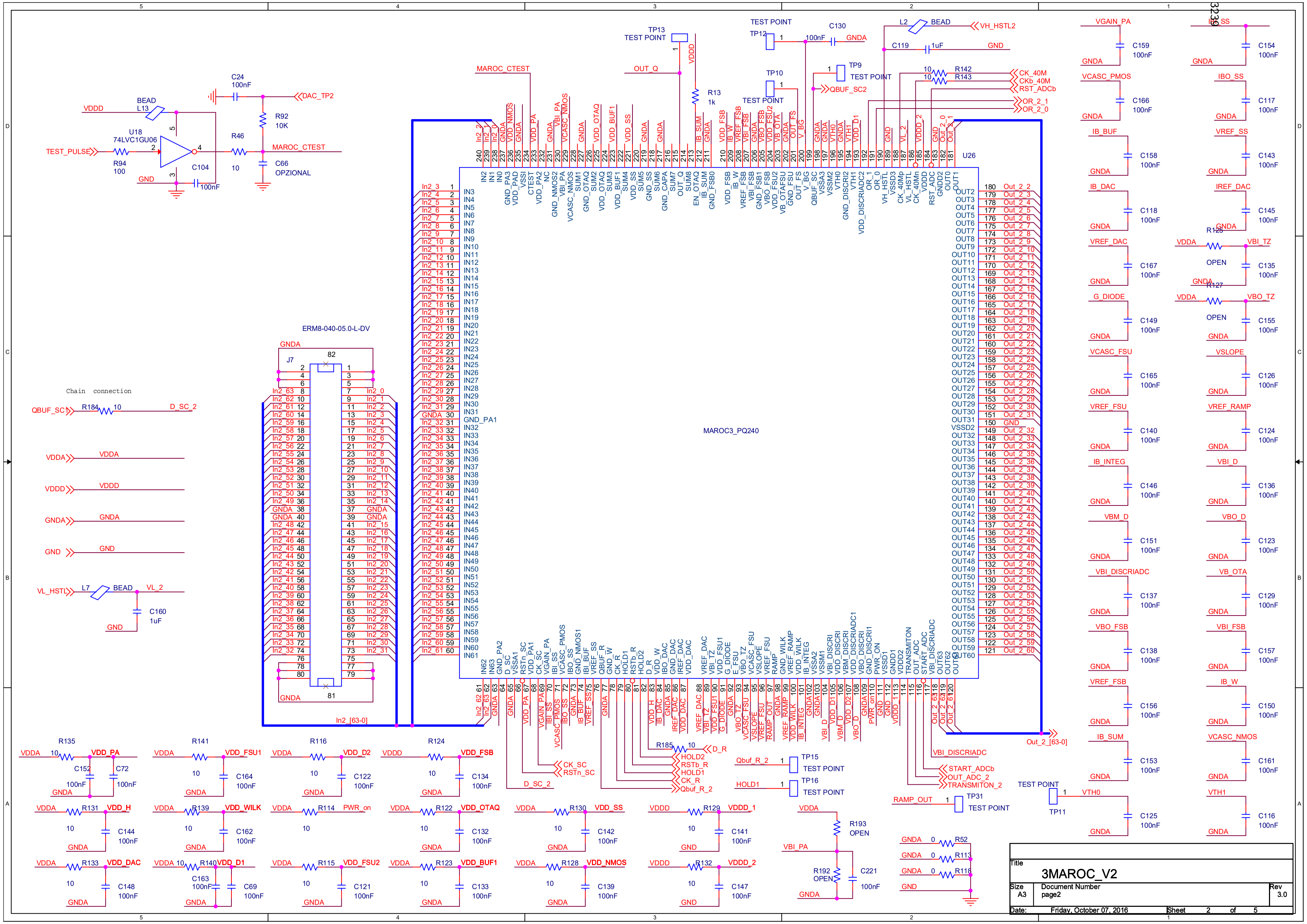
MAROC3_PQ240
ERM8-040-05.0-L-DV
Title
3MAROC_V2
Size
A3
Document Number
page2
Rev
3.0
Date: Friday, October 07, 2016
Sheet 2 of 5

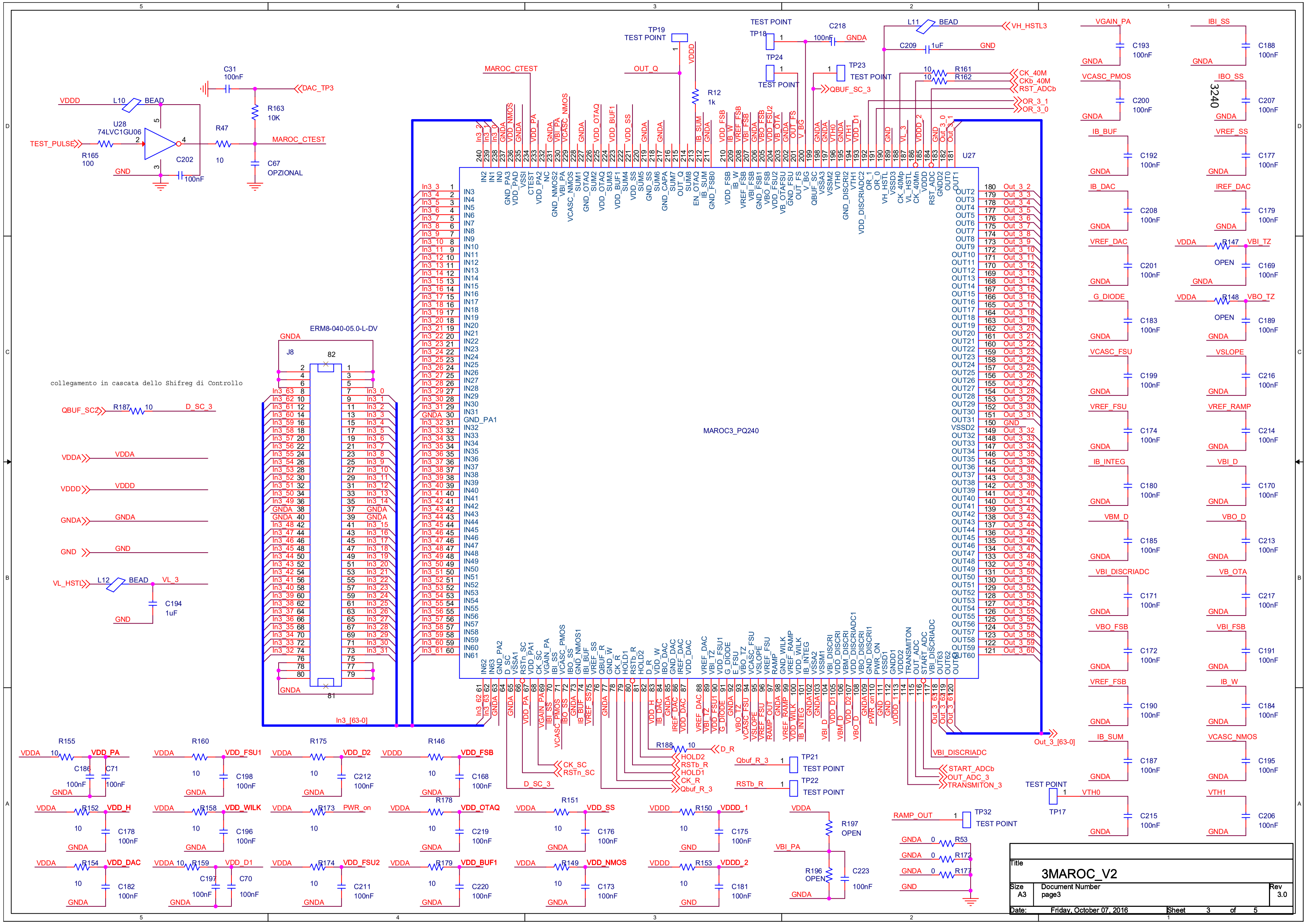
3MAROC_V2
Title
Size
A3
Document Number
page3
Rev
3.0
Date:
Friday, October 07, 2016
Sheet
3
of
5
MAROC3_PQ240
ERM8-040-05.0-L-DV
collegamento in cascata dello Shifreg di Controllo

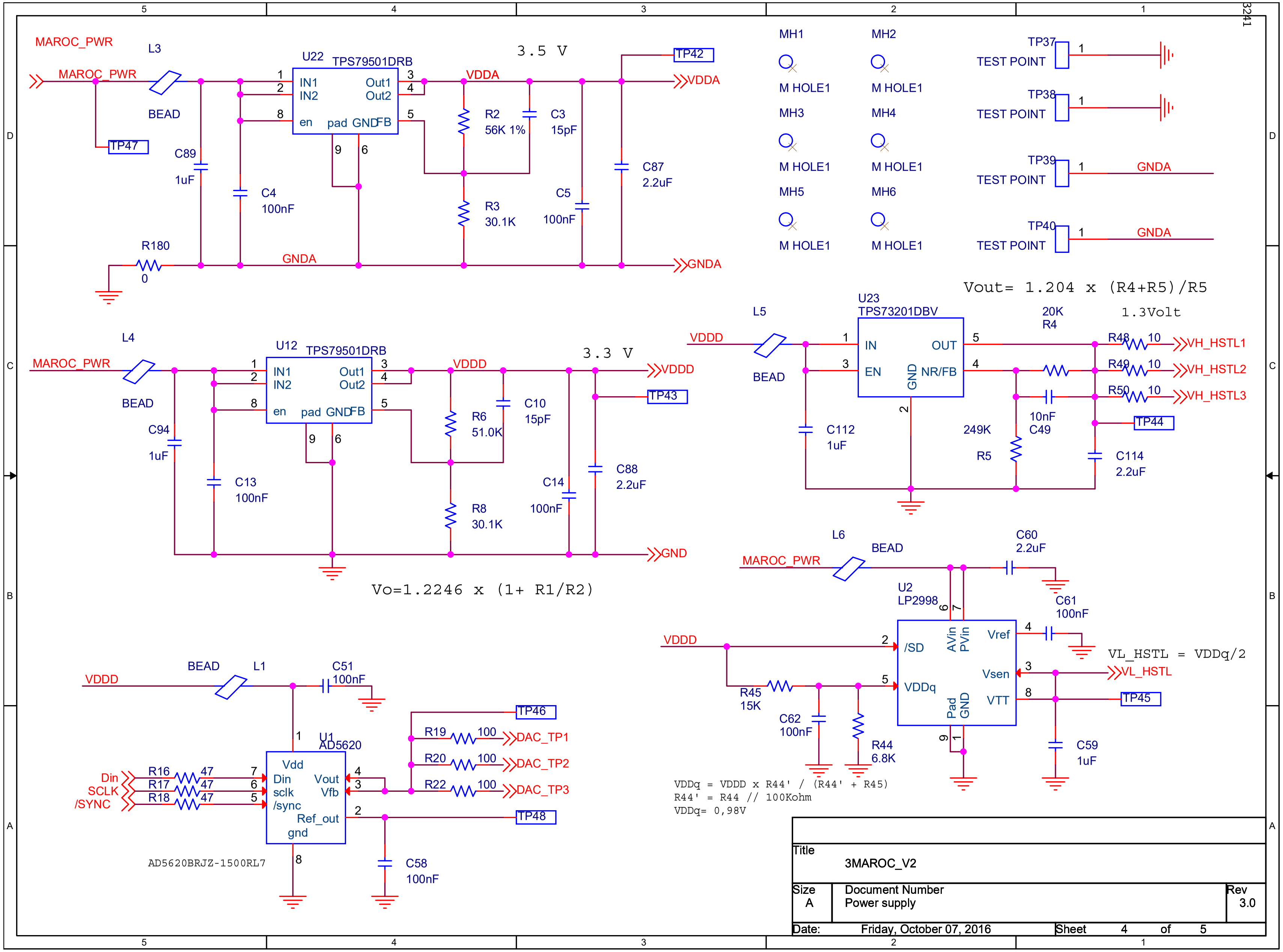
3241
MAROC_PWR
L3
BEAD
TP47
C89
1uF
C4
100nF
R180
0
U22 TPS79501DRB
IN1
IN2
en
pad GND FB
Out1
Out2
VDDA
R2
56K 1%
C3
15pF
R3
30.1K
C5
100nF
C87
2.2uF
3.5 V
TP42
VDDA
GNDA
MH1
MH2
M HOLE1
MH3
MH4
MH5
MH6
TP37
TP38
TP39
TP40
TEST POINT
Vout= 1.204 x (R4+R5)/R5
1.3Volt
L4
U12 TPS79501DRB
VDDD
R6
51.0K
C10
15pF
R8
30.1K
C14
100nF
C88
2.2uF
C94
1uF
C13
100nF
3.3 V
TP43
GND
Vo=1.2246 x (1+ R1/R2)
L5
U23
TPS73201DBV
IN
EN
OUT
NR/FB
GND
20K
R4
R48 10
R49 10
R50 10
VH_HSTL1
VH_HSTL2
VH_HSTL3
TP44
C112
1uF
249K
R5
10nF
C49
C114
2.2uF
L6
C60
2.2uF
U2
LP2998
C61
100nF
/SD
AVin
PVin
Vref
VDDq
Vsen
VTT
Pad
GND
VL_HSTL = VDDq/2
VL_HSTL
TP45
R45
15K
C62
100nF
R44
6.8K
C59
1uF
VDDq = VDDD x R44' / (R44' + R45)
R44' = R44 // 100Kohm
VDDq= 0,98V
L1
C51
100nF
U1
AD5620
Vdd
Din
sclk
/sync
Vout
Vfb
Ref_out
gnd
R16 47
R17 47
R18 47
Din
SCLK
/SYNC
R19 100
R20 100
R22 100
DAC_TP1
DAC_TP2
DAC_TP3
TP46
TP48
C58
100nF
AD5620BRJZ-1500RL7
Title
3MAROC_V2
Size
A
Document Number
Power supply
Rev
3.0
Date: Friday, October 07, 2016
Sheet 4 of 5

3242

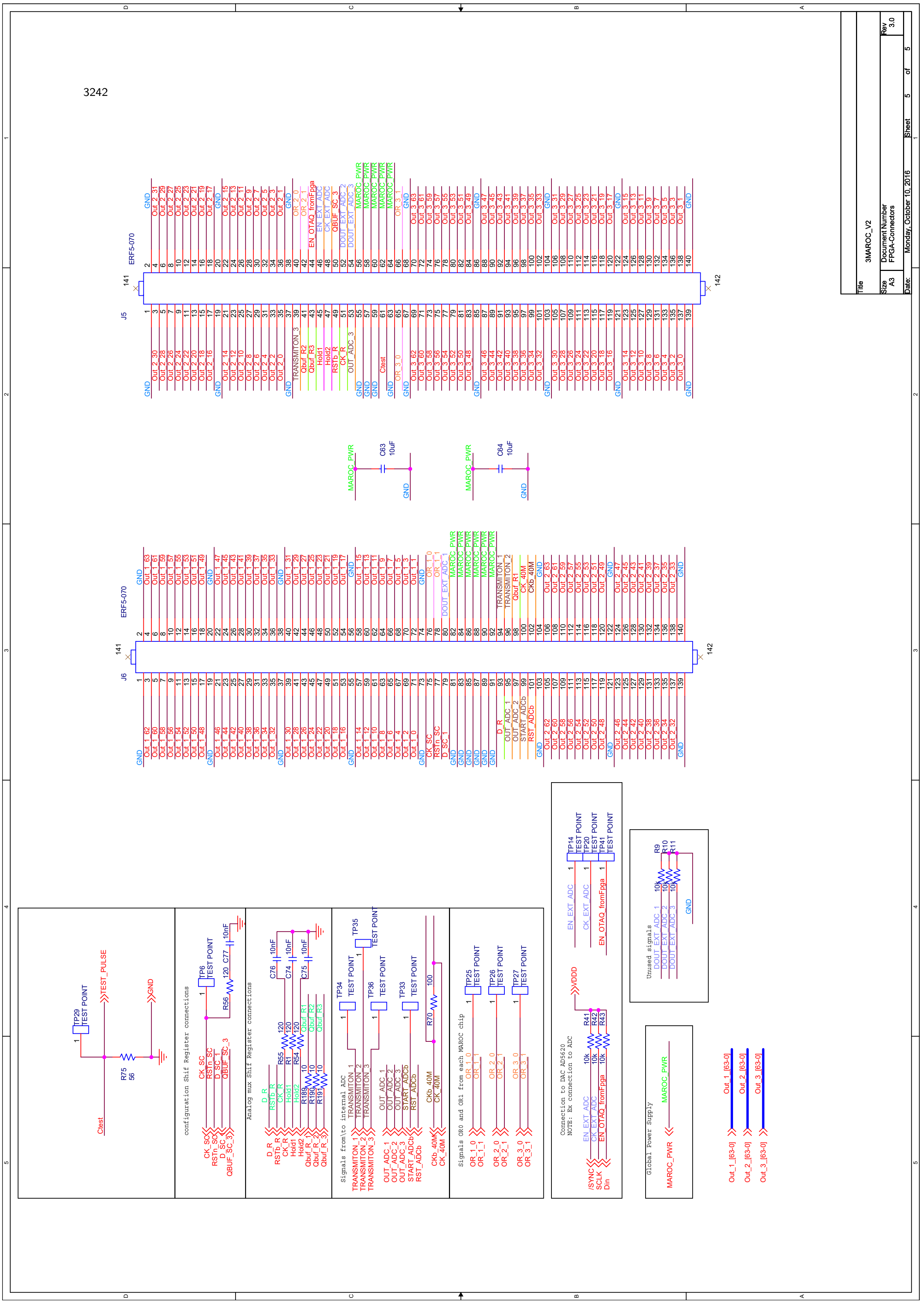
Title
3MAROC_V2
Size
A3
Document Number
FPGA-Connectors
Rev
3.0
Date: Monday, October 10, 2016
Sheet 5 of 5
J5
ERF5-070
J6
ERF5-070

3243

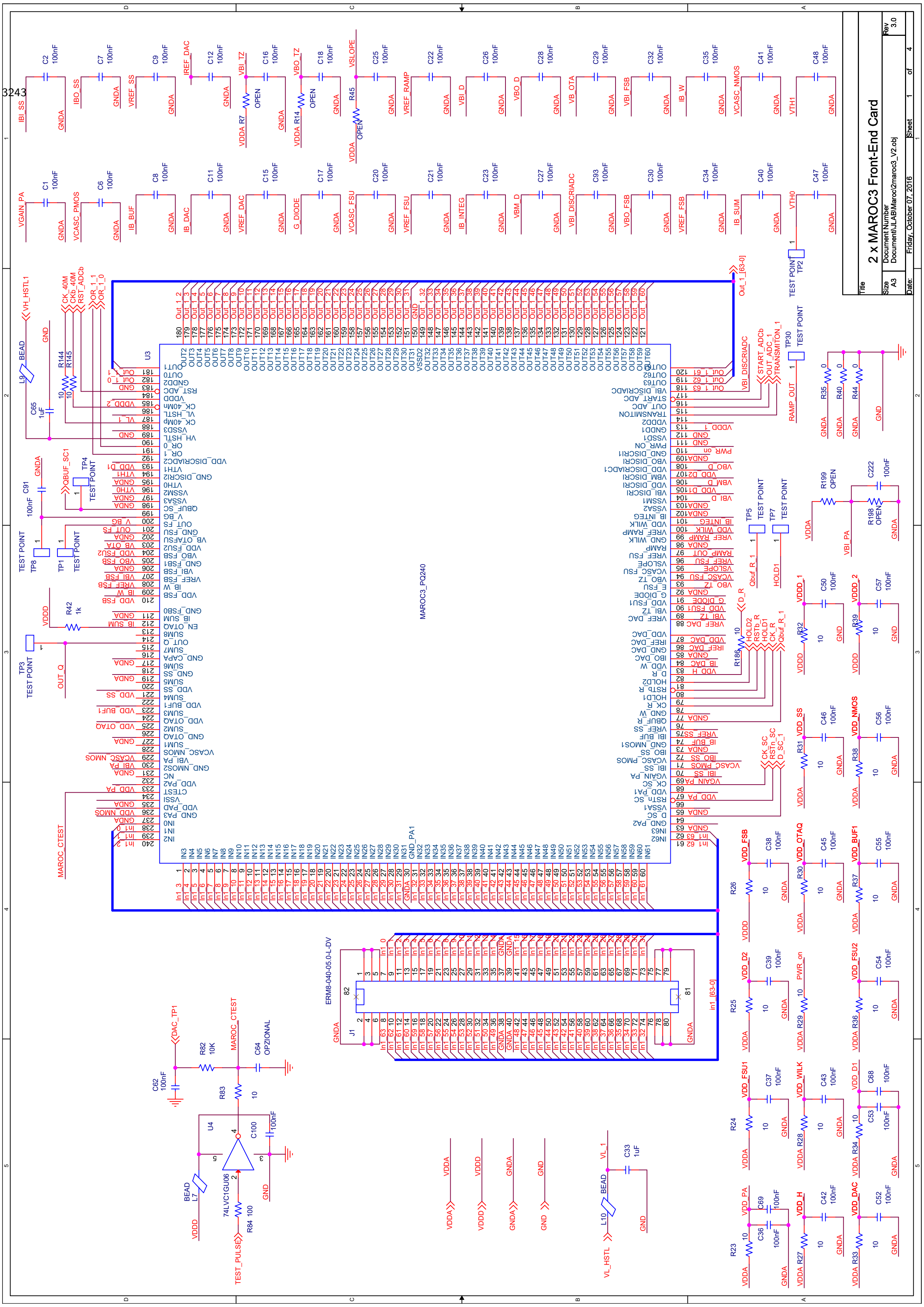

Title
2 x MAROC3 Front-End Card
Size
A3
Document Number
Document\LAB\Maroc\2maroc3_V2.obj
Rev
3.0
Date: Friday, October 07, 2016
Sheet 1 of 4

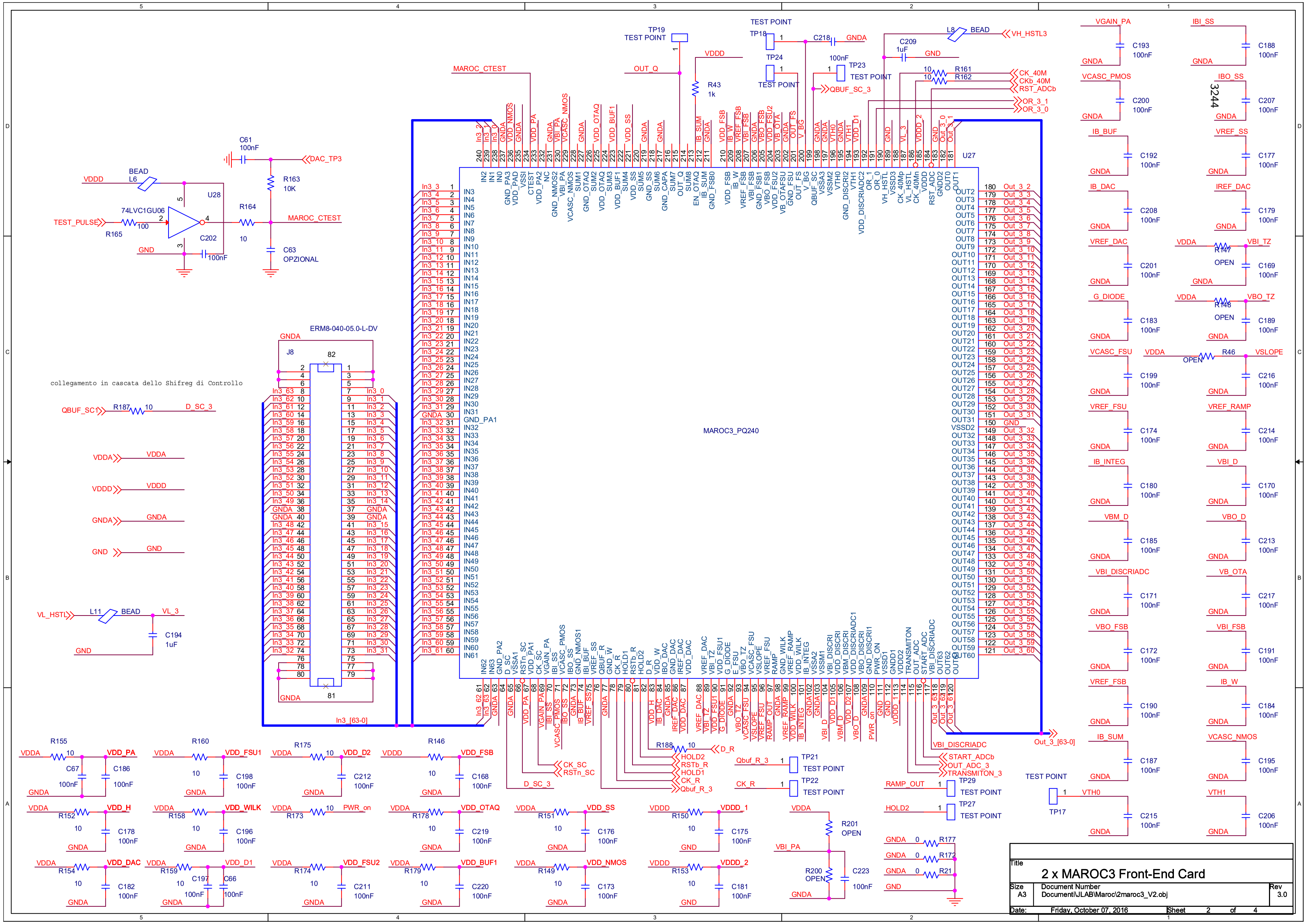

2 x MAROC3 Front-End Card
Title
Size A3
Document Number
Document\JLAB\Maroc\2maroc3_V2.obj
Rev 3.0
Date: Friday, October 07, 2016
Sheet 2 of 4
MAROC3_PQ240
U27
ERM8-040-05.0-L-DV
J8
74LVC1GU06
U28
collegamento in cascata dello Shifreg di Controllo
TEST POINT
3244

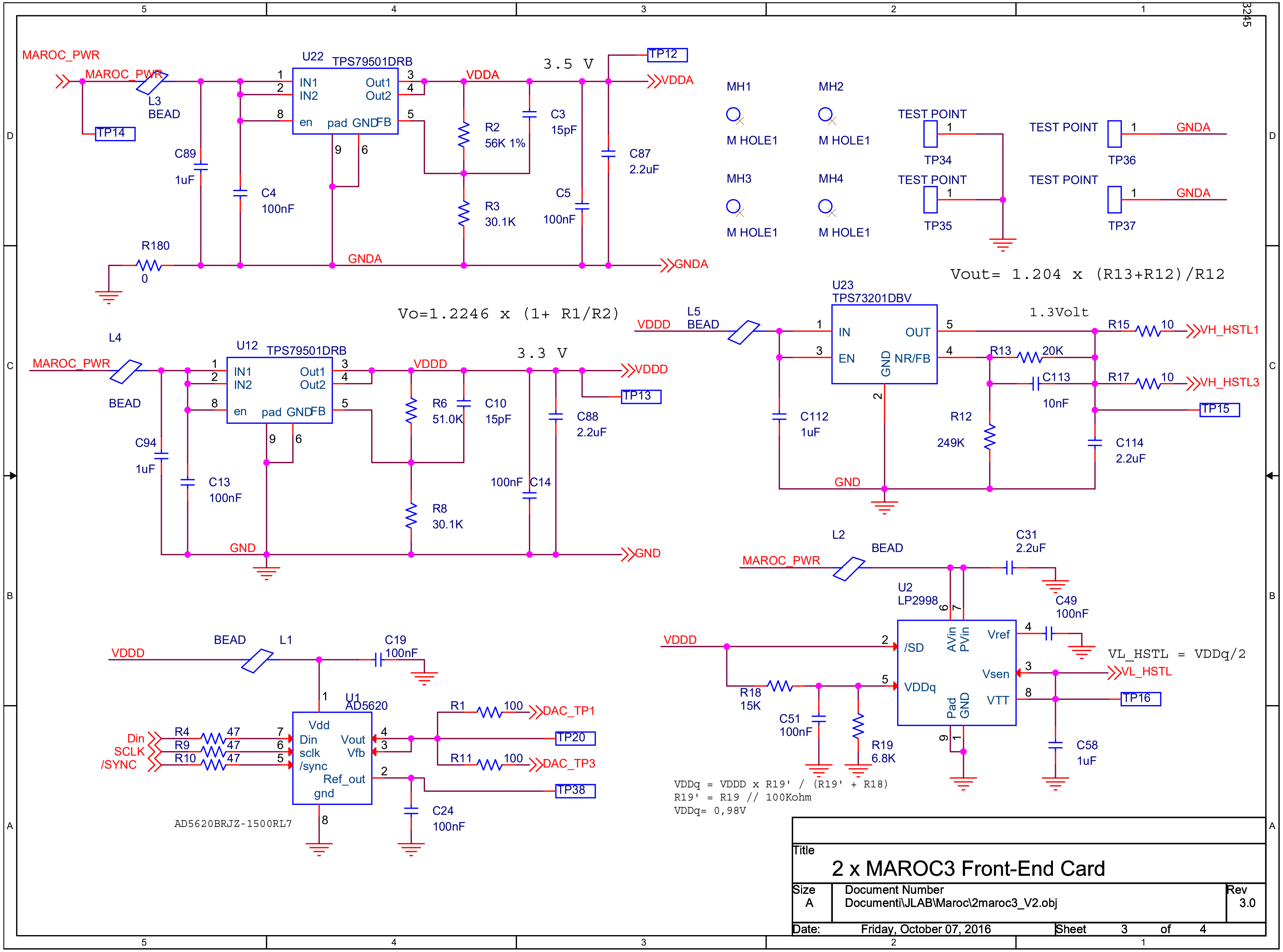

3245
MAROC_PWR
L3 BEAD
TP14
C89 1uF
C4 100nF
R180 0
U22 TPS79501DRB
IN1 IN2 en pad GND FB Out1 Out2
VDDA
3.5 V
R2 56K 1%
R3 30.1K
C3 15pF
C5 100nF
C87 2.2uF
TP12
GNDA
Vo=1.2246 x (1+ R1/R2)
L4 BEAD
C94 1uF
C13 100nF
U12 TPS79501DRB
VDDD
3.3 V
R6 51.0K
C10 15pF
R8 30.1K
100nF C14
C88 2.2uF
TP13
GND
MH1 M HOLE1
MH2 M HOLE1
MH3 M HOLE1
MH4 M HOLE1
TEST POINT TP34
TEST POINT TP35
TEST POINT TP36
TEST POINT TP37
Vout= 1.204 x (R13+R12)/R12
U23 TPS73201DBV
IN EN GND OUT NR/FB
L5 BEAD
C112 1uF
1.3Volt
R15 10 VH_HSTL1
R13 20K
C113 10nF
R17 10 VH_HSTL3
TP15
R12 249K
C114 2.2uF
L2 BEAD
C31 2.2uF
U2 LP2998
C49 100nF
/SD AVin PVin Vref Vsen VTT VDDq Pad GND
VL_HSTL = VDDq/2
VL_HSTL
TP16
R18 15K
C51 100nF
R19 6.8K
C58 1uF
VDDq = VDDD x R19' / (R19' + R18)
R19' = R19 // 100Kohm
VDDq= 0,98V
L1 BEAD
C19 100nF
U1 AD5620
Vdd Din sclk /sync Vout Vfb Ref_out gnd
Din SCLK /SYNC
R4 47
R9 47
R10 47
R1 100 DAC_TP1
TP20
R11 100 DAC_TP3
TP38
C24 100nF
AD5620BRJZ-1500RL7
Title
2 x MAROC3 Front-End Card
Size A
Document Number
Documenti\JLAB\Maroc\2maroc3_V2.obj
Rev 3.0
Date: Friday, October 07, 2016
Sheet 3 of 4

3246

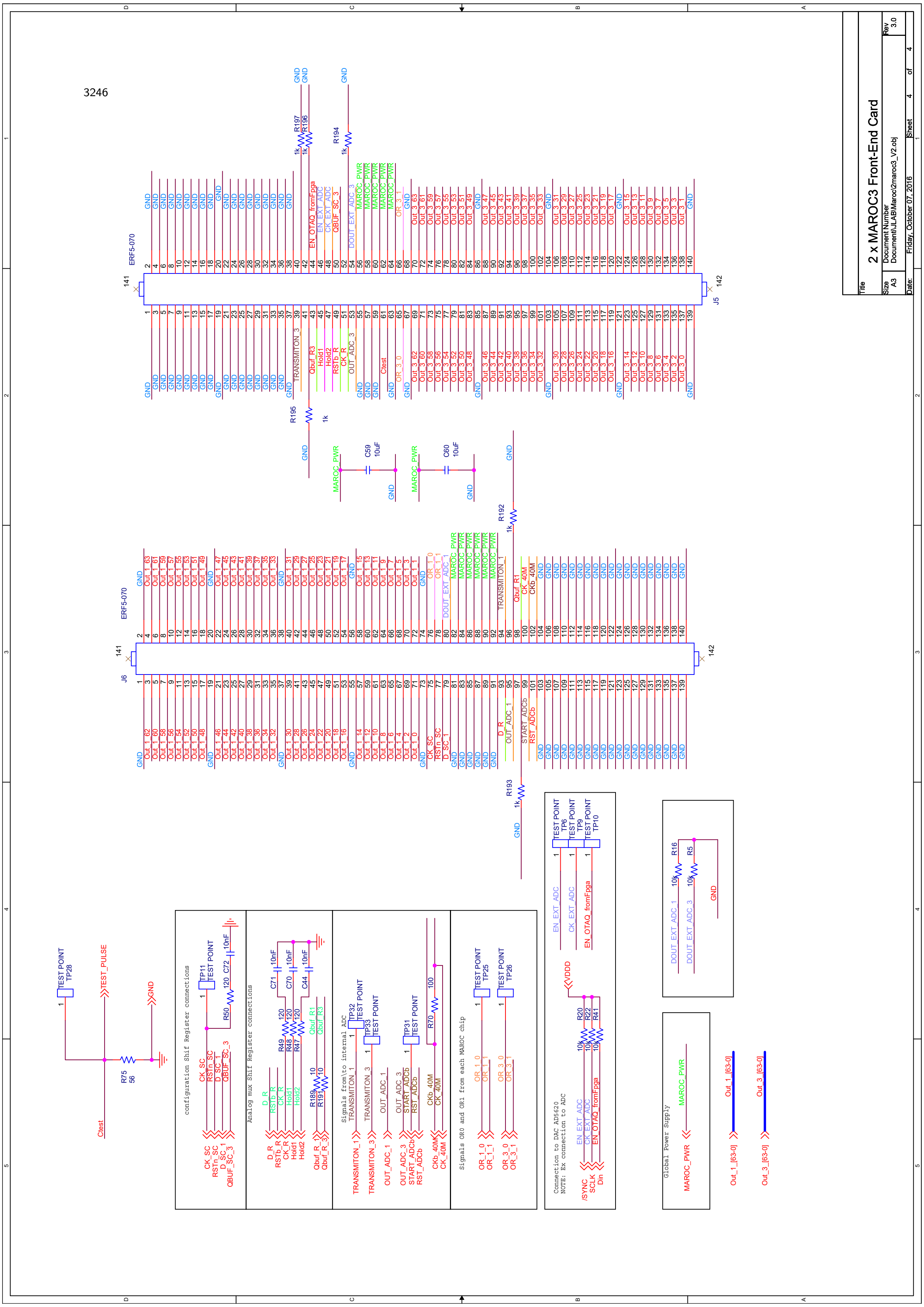

2 x MAROC3 Front-End Card
Title
Size
A3
Document Number
Rev
3.0
Date: Friday, October 07, 2016
Sheet 4 of 4

3247

Bibliography

[1] S. Pisano *et al.*, "Single and double spin asymmetries for deeply virtual compton scattering measured with CLAS and a longitudinally polarized proton target," *Phys. Rev.*, vol. D91, no. 5, p. 052014, 2015.

[2] B. Mecking *et al.*, "The {CEBAF} large acceptance spectrometer ({CLAS})," *Nuclear Instruments and Methods in Physics Research Section A: Accelerators, Spectrometers, Detectors and Associated Equipment*, vol. 503, no. 3, pp. 513 – 553, 2003.

[3] M. M. et al, "The clas12-rich technical design report," Tech. Rep. 1, JLAB, September 2013.

[4] A. E. Alaoui, N. Baltzell, and K. Hafidi, "A rich detector for clas12 spectrometer," *Physics Procedia*, vol. 37, pp. 773 – 780, 2012.

[5] J. Séguinot, J. Tocqueville, and T. Ypsilantis, "Imaging cerenkov detector: Photo-ionization of tri-ethyl-amine," *Nuclear Instruments and Methods*, vol. 173, no. 2, pp. 283 – 298, 1980.

[6] M. Contalbrigo, M.Turisini, *et al.*, "The large-area hybrid-optics {CLAS12} {RICH} detector: Tests of innovative components," *Nuclear Instruments and Methods in Physics Research Section A: Accelerators, Spectrometers, Detectors and Associated Equipment*, vol. 766, pp. 22 – 27, 2014. {RICH2013} Proceedings of the Eighth International Workshop on Ring Imaging Cherenkov Detectors Shonan, Kanagawa, Japan, December 2-6, 2013.

[7] F. Garibaldi, E. Cisbani, S. Colilli, F. Cusanno, S. Frullani, R. Fratoni, F. Giuliani, M. Gricia, M. Iodice, M. Lucentini, L. Pierangeli, F. Santavenere, G. Urciuoli, P. Veneroni, G. Cataldo, R. Leo, L. Lagamba, E. Nappi, V. Paticchio, J. LeRose, B. Kross, B. Reitz, J. Segal, C. Zorn, and H. Breuer, "A proximity focusing {RICH} detector for kaon physics at jefferson lab hall a," *Nuclear Instruments and Methods in Physics*

Research Section A: Accelerators, Spectrometers, Detectors and Associated Equipment, vol. 502, no. 1, pp. 117 – 122, 2003. Experimental Techniques of Cherenkov Light Imaging. Proceedings of the Fourth International Workshop on Ring Imaging Cherenkov Detectors.

[8] A. Pereira, M. Turisini, *et al.*, "Test of the clas12 rich large-scale prototype in the direct proximity focusing configuration," *The European Physical Journal A*, vol. 52, no. 2, p. 23, 2016.

[9] Y. Sallaz-Damaz, L. Derome, M. Mangin-Brinet, M. Loth, K. Protasov, A. Putze, M. Vargas-Trevino, O. Véziant, M. Buénerd, A. Menchaca-Rocha, E. Belmont, M. Vargas-Magaña, H. Léon-Vargas, A. Ortiz-Velàsquez, A. Malinine, F. Baraõ, R. Pereira, T. Bellunato, C. Matteuzzi, and D. Perego, "Characterization study of silica aerogel for cherenkov imaging," *Nuclear Instruments and Methods in Physics Research Section A: Accelerators, Spectrometers, Detectors and Associated Equipment*, vol. 614, no. 2, pp. 184 – 195, 2010.

[10] T. Iijima, "Development of {RICH} counters towards the kekb/belle upgrade," *Nuclear Instruments and Methods in Physics Research Section A: Accelerators, Spectrometers, Detectors and Associated Equipment*, vol. 598, no. 1, pp. 138 – 142, 2009. Instrumentation for Collding Beam PhysicsProceedings of the 10th International Conference on Instrumentation for Colliding Beam Physics.

[11] A. Barnyakov, M. Barnyakov, K. Beloborodov, V. Bobrovnikov, A. Buzykaev, V. Golubev, B. Gulevich, A. Danilyuk, S. Kononov, E. Kravchenko, K. Martin, A. Onuchin, V. Porosev, and S. Serednyakov, "Status of aerogel production in novosibirsk," *Nuclear Instruments and Methods in Physics Research Section A: Accelerators, Spectrometers, Detectors and Associated Equipment*, vol. 639, no. 1, pp. 225 – 226, 2011. Proceedings of the Seventh International Workshop on Ring Imaging Cherenkov Detectors.

[12] M. Hoek, V. Lucherini, M. Mirazita, R. A. Montgomery, A. Orlandi, S. Anefalos Pereira, S. Pisano, P. Rossi, A. Viticchiè, and A. Witchger, "Investigation of Hamamatsu H8500 phototubes as single photon detectors," *ArXiv e-prints*, Sept. 2014.

[13] R. Dolenec, H. Chagani, S. Korpar, P. Križan, R. Pestotnik, and A. Stanovnik, "Tests of a silicon photomultiplier module for detection of cherenkov photons," *Nuclear Instruments and Methods in Physics Research Section A: Accelerators, Spectrometers, Detectors and Associated

Equipment, vol. 628, no. 1, pp. 398 – 402, 2011. {VCI} 2010Proceedings of the 12th International Vienna Conference on Instrumentation.

[14] S. S. Majos, P. Achenbach, C. A. Gayoso, J. Bernauer, R. Böhm, M. Distler, M. G. R. de la Paz, H. Merkel, U. Müller, L. Nungesser, J. Pochodzalla, B. Schlimme, T. Walcher, M. Weinriefer, and C. Yoon, "Noise and radiation damage in silicon photomultipliers exposed to electromagnetic and hadronic radiation," *Nuclear Instruments and Methods in Physics Research Section A: Accelerators, Spectrometers, Detectors and Associated Equipment*, vol. 602, no. 2, pp. 506 – 510, 2009.

[15] B. W. Adams, K. Attenkofer, M. Bogdan, K. Byrum, A. Elagin, J. W. Elam, H. J. Frisch, J.-F. Genat, H. Grabas, J. Gregar, E. Hahn, M. Heintz, Z. Insepov, V. Ivanov, S. Jelinsky, S. Jokely, S. W. Lee, A. U. Mane, J. McPhate, M. J. Minot, P. Murat, K. Nishimura, R. Northrop, R. Obaid, E. Oberla, E. Ramberg, A. Ronzhin, O. H. Siegmund, G. Sellberg, N. T. Sullivan, A. Tremsin, G. Varner, I. Veryovkin, A. Vostrikov, R. G. Wagner, D. Walters, H.-H. Wang, M. Wetstein, J. Xi, Z. Yusov, and A. Zinovev, "A Brief Technical History of the Large-Area Picosecond Photodetector (LAPPD) Collaboration," *ArXiv e-prints*, Mar. 2016.

[16] E. Oberla, H. Grabas, M. Bogdan, H. Frisch, J. Genat, K. Nishimura, G. Varner, and A. Wong, "A 4-channel waveform sampling asic in 0.13 um cmos for front-end readout of large-area micro-channel plate detectors," *Physics Procedia*, vol. 37, pp. 1690 – 1698, 2012.

[17] R. Pani, M. Cinti, R. Pellegrini, C. Trotta, G. Trotta, L. Montani, S. Ridolfi, F. Garibaldi, R. Scafè, N. Belcari, and A. D. Guerra, "Evaluation of flat panel {PMT} for gamma ray imaging," *Nuclear Instruments and Methods in Physics Research Section A: Accelerators, Spectrometers, Detectors and Associated Equipment*, vol. 504, no. 1–3, pp. 262 – 268, 2003. Proceedings of the 3rd International Conference on New Developments in Photodetection.

[18] D. Herbert, N. Belcari, M. Camarda, and A. D. Guerra, "A comparison of the imaging performance of different {PSPMTs} for {PET} applications," *Nuclear Instruments and Methods in Physics Research Section A: Accelerators, Spectrometers, Detectors and Associated Equipment*, vol. 518, no. 1–2, pp. 399 – 400, 2004. Frontier Detectors for Frontier Physics: Proceedin.

[19] F. Garibaldi, E. Cisbani, S. Colilli, F. Cusanno, R. Fratoni, F. Giuliani, M. Gricia, M. Lucentini, R. Fratoni, S. L. Meo, M. Magliozzi, F. San-

tanvenere, M. Cinti, R. Pani, R. Pellegrini, G. Simonetti, O. Schillaci, S. D. Vecchio, M. Salvatore, S. Majewski, R. Lanza, G. D. Vincentis, and F. Scopinaro, "Molecular imaging: High-resolution detectors for early diagnosis and therapy monitoring of breast cancer," *Nuclear Instruments and Methods in Physics Research Section A: Accelerators, Spectrometers, Detectors and Associated Equipment*, vol. 569, no. 2, pp. 286 – 290, 2006. Proceedings of the 3rd International Conference on Imaging Technologies in Biomedical SciencesInnovation in Nuclear and Radiological Imaging: from Basic Research to Clinical Application.

[20] R. Montgomery, E. Cowie, M. Hoek, T. Keri, and B. Seitz, "Multi-anode photomultiplier tube studies for imaging applications," *Nuclear Instruments and Methods in Physics Research Section A: Accelerators, Spectrometers, Detectors and Associated Equipment*, vol. 695, pp. 326 – 329, 2012. New Developments in Photodetection {NDIP11}.

[21] M. Calvi, P. Carniti, L. Cassina, C. Gotti, M. Maino, C. Matteuzzi, and G. Pessina, "Characterization of the hamamatsu h12700a-03 and r12699-03 multi-anode photomultiplier tubes," *Journal of Instrumentation*, vol. 10, no. 09, p. P09021, 2015.

[22] C. d. L. T. S.Blin, P.Barillon, "Maroc, a generic photomultiplier readout chip," in *Topical Workshop on Electronics for Particle Physics* (J. of Instrumentaion, ed.), SISSA, IOP, December 2010.

[23] P. Carniti, M. D. Matteis, A. Giachero, C. Gotti, M. Maino, and G. Pessina, "Claro-cmos, a very low power asic for fast photon counting with pixellated photodetectors," *Journal of Instrumentation*, vol. 7, no. 11, p. P11026, 2012.

[24] C. F. et al, "Dream: a 64-channel front-end chip with analogue trigger latency bu er for the micromégas tracker of the CLAS12 experiment." September 2014.

[25] P. Degtiarenko, "Precision analysis of the photomultiplier response to ultra low signals," *ArXiv e-prints*, Aug. 2016.

[26] M. Contalbrigo, "Tests of innovative photon detectors and integrated electronics for the large-area {CLAS12} ring-imaging cherenkov detector," *Nuclear Instruments and Methods in Physics Research Section A: Accelerators, Spectrometers, Detectors and Associated Equipment*, vol. 787, pp. 224 – 228, 2015. New Developments in Photodetection {NDIP14}.

[27] M. Mirazita, M.Turisini, *et al.*, "The large-area hybrid-optics RICH detector for the CLAS12 spectrometer," in *RICH2016* (N. Instruments and S. A. Methods in Physics Research, eds.), Elsevier/North-Holland, 2016.

[28] laria Balossino, M.Turisini, *et al.*, "Cherenkov light imaging tests with state-of-the-art solid state photon counter for the CLAS12 RICH detector," in *RICH2016* (N. Instruments and S. A. Methods in Physics Research, eds.), Elsevier/North-Holland, 2016.

[29] M. Contalbrigo, I. Balossino, L. Barion, G. Battaglia, A. Barnyakov, A. Danilyuk, A. Katcin, E. Kravchenko, M. Mirazita, A. Movsisyan, L. Pappalardo, and S. Squerzanti, "Aerogel mass production for the CLAS12 RICH: Novel characterization methods and Optical Performance," in *RICH2016* (N. Instruments and S. A. Methods in Physics Research, eds.), Elsevier/North-Holland, 2016.

[30] A. G. Argentieri, E. Cisbani, S. Colilli, F. Cusanno, R. D. Leo, R. Fratoni, F. Garibaldi, F. Giuliani, M. Gricia, M. Lucentini, M. L. Magliozzi, M. Marra, P. Musico, F. Santavenere, S. Torrioli, and G. Vacca, "A novel modular and flexible readout electronics for photon imaging applications," in *2008 IEEE Nuclear Science Symposium Conference Record*, pp. 2132–2136, Oct 2008.

[31] T. Higuchi, M. Nakao, and E. Nakano, "Radiation tolerance of readout electronics for belle ii," *Journal of Instrumentation*, vol. 7, no. 02, p. C02022, 2012.

[32] M. Fiorini, M. Andreotti, W. Baldini, R. Calabrese, P. Carniti, L. Cassina, A. C. Ramusino, A. Giachero, C. Gotti, E. Luppi, M. Maino, R. Malaguti, G. Pessina, and L. Tomassetti, "Radiation hardness tests and characterization of the claro-cmos, a low power and fast single-photon counting {ASIC} in 0.35 micron {CMOS} technology," *Nuclear Instruments and Methods in Physics Research Section A: Accelerators, Spectrometers, Detectors and Associated Equipment*, vol. 766, pp. 228 – 230, 2014. {RICH2013} Proceedings of the Eighth International Workshop on Ring Imaging Cherenkov Detectors Shonan, Kanagawa, Japan, December 2-6, 2013.

[33] P. Adell, G. Allen, G. Swift, and S. McClure, "Assessing and mitigating radiation effects in xilinx sram fpgas," in *2008 European Conference on Radiation and Its Effects on Components and Systems*, pp. 418–424, Sept 2008.

[34] Xilinx, *Soft Error Mitigation Controller v4.1, LogiCORE IP Product Guide*. Xilinx, September 2015.

[35] American Society for Testing and Materials International, West Conshohocken, Pennsylvania, USA, *Standard Practice for Characterizing Neutron Fluence Spectra in Terms of an Equivalent Monoenergetic Neutron Fluence for Radiation- Hardness Testing of Electronics*, August 2009.

[36] C. Wong, M.Turisini, *et al.*, "Modular focusing ring imaging cherenkov detector for electron-ion collider experiments." Preprint submitted to Nuclear Instruments and Methods in Physics Research A, January 2017.

[37] A. Accardi, J. L. Albacete, M. Anselmino, N. Armesto, E. C. Aschenauer, A. Bacchetta, D. Boer, W. K. Brooks, T. Burton, N.-B. Chang, W.-T. Deng, A. Deshpande, M. Diehl, A. Dumitru, R. Dupré, R. Ent, S. Fazio, H. Gao, V. Guzey, H. Hakobyan, Y. Hao, D. Hasch, R. Holt, T. Horn, M. Huang, A. Hutton, C. Hyde, J. Jalilian-Marian, S. Klein, B. Kopeliovich, Y. Kovchegov, K. Kumar, K. Kumerički, M. A. C. Lamont, T. Lappi, J.-H. Lee, Y. Lee, E. M. Levin, F.-L. Lin, V. Litvinenko, T. W. Ludlam, C. Marquet, Z.-E. Meziani, R. McKeown, A. Metz, R. Milner, V. S. Morozov, A. H. Mueller, B. Müller, D. Müller, P. Nadel-Turonski, H. Paukkunen, A. Prokudin, V. Ptitsyn, X. Qian, J.-W. Qiu, M. Ramsey-Musolf, T. Roser, F. Sabatié, R. Sassot, G. Schnell, P. Schweitzer, E. Sichtermann, M. Stratmann, M. Strikman, M. Sullivan, S. Taneja, T. Toll, D. Trbojevic, T. Ullrich, R. Venugopalan, S. Vigdor, W. Vogelsang, C. Weiss, B.-W. Xiao, F. Yuan, Y.-H. Zhang, and L. Zheng, "Electron Ion Collider: The Next QCD Frontier - Understanding the glue that binds us all," *ArXiv e-prints*, Dec. 2012.